UNIVERSITY OF CALIFORNIA
RIVERSIDE

The Union Island Group of the Great Slave Lake, NWT, Canada: A Perspective on the Aftermath of the Lomagundi Carbon Isotope Excursion

A Dissertation submitted in partial satisfaction
of the requirements for the degree of

Master of Science

in

Geological Sciences

by

Logan Kiel Magad-Weiss

September 2019

Thesis Committee:
Dr. Andrey Bekker, Chairperson
Dr. Timothy Lyons
Dr. Gordon Love

The Dissertation of Logan Kiel Magad-Weiss is approved:

Committee Chairperson

University of California, Riverside

Table of Contents:

List of Tables:

List of Figures:

Chapter 1: Introduction

Temporally constraining the appearance of free oxygen in the atmosphere, and the Earth's response to such a change remains a critical question in Earth's Sciences. Many proxies have been invoked to explain when the concentration of oxygen in the atmosphere rose to levels substantially different from the low levels of the Archean, namely the disappearance of mass independent fractionation of sulfur (Farquhar et al., 2000), and trace metal records (Jones and Manning, 1994; Lyons et al., 2014; Partin et al., 2013). It is inferred that oxygenation of the Earth's System occurred over two time intervals during the Precambrian, first during the Paleoproterozoic (2.4-2.3 Ga ago; Gumsley et al., 2017; Lyons et al., 2014), and a much later event during the Neoproterozoic (0.8-0.65 Ga ago); (Och and Shields-Zhou, 2012; Planavsky et al., 2014b; Stüeken et al., 2016) after approximately a billion years of intermediate oxygen levels that were substantially higher than in the Archean, but significantly lower than Phanerozoic concentrations (Kipp et al., 2018; Lyons et al., 2014). Earth's shift from globally reducing to oxidizing conditions was initiated with the onset of the Great Oxidation Event (GOE) between ~2.4 and 2.3 Ga and persisted until ~2.1-2.0 Ga (Bekker, 2014; Bekker and Holland, 2012; Holland, 2002), ultimately coming to an end with the conclusion of the Lomagundi Event (LE), during which the carbon isotopic values in carbonates became highly positive, averaging +8‰, with values of +16‰ being common, and even as high as +28‰ VPDB (Bekker et al., 2003; Bekker et al., 2008; Bekker and Holland, 2012; Karhu and Holland, 1996). Termination of the LE is marked by deposition of organic-rich lithologies (Martin et al., 2013; Melezhik et al., 1999), a

crash of the seawater sulfate reservoir (Bekker and Holland, 2012), deposition of Mn-rich sediments (Bekker et al., 2003; Ossa Ossa et al., 2018), the first appearance of phosphorite deposits (Bekker et al., 2003; Bekker and Holland, 2012; Maheshwari et al., 2010; Papineau, 2010), rarely deposition of iron formation (Bekker et al., 2003; Ossa-Ossa et al., 2018), and return of carbon isotopic values in carbonates to around 0‰ (Bekker and Holland, 2012; Maheshwari et al., 2010; Melezhik et al., 1999). Initially described by Schidlowski et al., 1975 in the Lomagundi Group of Zimbabwe, carbonates deposited between 2.22 and 2.06 Ga globally have shown highly positive carbon isotopic signatures and have been identified on all continents with the exception of Antarctica (Bekker, 2014).

Under the reducing conditions of the Archean, large reservoirs of reduced materials, most notably sulfides (including pyrite) accumulated in the upper crust on the continents. Oxidative weathering of pyrite in the upper crust acidified groundwaters through production of sulfuric acid (Bekker and Holland, 2012), enhancing dissolution of phosphate minerals (Bekker and Holland, 2012; Ossa Ossa et al., 2018). Delivery of higher concentrations of phosphorus to the ocean through oxidative weathering stimulated primary productivity, increased burial of organic matter, and oxygen concentrations in the atmosphere. Carbon isotope ratios in carbonates were driven to highly positive values by extensive removal of isotopically light carbon derived burial of organic matter (Bekker and Holland, 2012; Konhauser et al., 2011; Kump et al., 2011). Temporal constraints on the termination of the LE remain a topic of debate, as there is no known succession in which the strata record the entire duration of the LE beginning with

the rise of carbonate carbon isotope values to highly positive values, and then returning back to values of ~0‰. A generally accepted end for the LE in the literature is at ~2.06 Ga (Bekker, 2014; Bekker and Holland, 2012; Karhu and Holland, 1996). Following the termination of the LE, it has been proposed that the seawater carbonate carbon returned to 0‰, resulting in an ocean deoxygenation event (Bekker and Holland, 2012; Bekker et al., 2016; Kump et al., 2011). Three mechanisms have been proposed to explain the return of carbonate carbon isotopic values to 0‰, and their contribution to the ocean deoxygenation event: 1) Decrease in a flux resulting from a decline in the availability of sulfides near the surface in the upper crust (Bekker and Holland, 2012). nutrient Titration of sulfides in the upper surface layer of the continents through oxidation of pyrite would lead to a decrease in the delivery of phosphorous from reduced dissolution of phosphate minerals with increasing pH, lowering of biological productivity, and allowing the system to return to "normal" conditions. 2) Oxidative weathering of organic-rich lithologies deposited during the LE contributed carbon with highly negative values leading to enhanced O_2 consumption (Bekker and Holland, 2012; Kump et al., 2011). 3) Volcanic and hydrothermal input of sulfides (Ossa-Ossa et al., 2018). Shoaling of anoxic deep waters enriched in Mn (II), Fe (II), H_2S, and CH_4 into the photic zone during transgressive periods likely stimulated the rate of microbial sulfate reduction (MSR), limited sulfate diffusion into sediments, and allowed methanogenic activity closer to the sediment-water interface (Ossa-Ossa et al., 2018).

Despite the generally accepted view that the LE terminated at ~2.06 Ga (Bekker, 2014; Bekker and Holland, 2012; Karhu and Holland, 1996), there is growing evidence

that there was instability in the biogeochemical carbon cycle in the aftermath of the LE, potentially fluctuating between periods of high and low productivity as recorded by carbon isotopic variations in carbonates. It has been conventionally suggested that following the end of the LE, carbon isotopic values in carbonates remained at around 0‰ and the so called "Boring Billion" began, during which there has been perceived long term stability in the carbon cycle up until the second great oxidation event during the Neoproterozoic (800-550 Ma) (Och and Shields-Zhou, 2012). Carbon isotopic analyses of carbonates from the Wooly Dolomite in the Horseshoe rift basin of Western Australia by Bekker et al., (2016) revealed highly positive isotopic values on the order of +8.4 ‰ VPDB, likely representing a primary global signal. U/Pb dating of zircons by SHRIMP method from a tuff in the Wooly Dolomite by Muller et al., (2003) yielded an age of 2031 ± 6 Ma, post-dating the end of the LE. Bekker et al., (2016) showed that in the aftermath of the LE there was at least one short-lived highly positive carbon isotope excursion.

The Slave craton of North America is an ~300,000 km^2 (Bleeker et al., 2000) portion of Archean crust bounded by Proterozoic rift margins (Bleeker et al., 2004). Located in the southeastern portion of the Slave craton, the East Arm Basin preserves an exposed Archean granitic basement, overlain by an extensive Paleoproterozoic cover sequence. The Union Island Group is a supracrustal succession of Paleoproterozoic quartz pebble conglomerate, carbonate, mafic volcanics, and mudrocks unconformably overlying an Archean granitic basement (Hoffman, 1968; Hoffman et al., 1977; Kjarsgaard et al., 2013). Rocks of the Union Island Group are of interest for stable

isotope analysis due to their Paleoproterozoic age and black shale bracketed by dolostone units. The Union Island Group has undergone lower greenschist facies metamorphism based on actinolite-chlorite-epidote-titanite mineralogy of mafic units and experienced only mild hydrothermal alteration recorded by carbonate veins (Kipp et al., 2018; Sheen, 2017). Thus, the carbonate and black shale units are suitable for compiling chemostratigraphic records, which will provide insights into the local depositional environment conditions during this intriguing interval of the Paleoproterozoic Era. Recently, Sheen et al., (2018) conducted U/Pb dating by isotope dilution thermal ionization mass spectrometry (ID-TIMS) of zircons from a volcanoclastic unit in the lower basalt unit. The U/Pb crystallization age yielded was 2045.8 ± 1.0 Ma, making the lower dolostone unit a candidate to record the last portion of the LE, or a separate carbon isotope excursion during the time period immediately after. Here, we present bulk carbonate carbon, oxygen, organic carbon, major and trace elements, rare earth elements and strontium isotopes from the upper and lower dolostone units, as well as organic carbon and nitrogen isotopes, redox-sensitive trace metal ratios, rare earth elements, Fe-speciation, and Sm/Nd isotopic data for the black shale unit in order to constrain if the Union Island Group records the latest portion of the LE, or a period immediately in its aftermath, and implications to geochemical cycling during the Paleoproterozoic.

Chapter 2: Geologic Background

The Paleoproterozoic East Arm basin developed along the southeastern margin of the Slave craton is underlain by the Archean granitic crust of the Slave craton and contains extensive, well-preserved Paleoproterozoic strata. The Archean Slave craton is bounded to the east by the Wopmay orogen (**Figure 2.2**), however geologic evolution of the eastern margin of the Slave craton is less understood with models inferred ranging from Himalayan-style collision (e.g., Gibb and Thomas, 1977; Hoffman, 1987; Tirrul and Grotzinger, 1990) to Tian Shan-style intracratonic underthrusting (Chacko et al., 2000; Snyder and Kjarsgaard, 2013). Until recently, it has been inferred that the allochthonous 1.93 Ga Wilson Island Group (Bowring et al., 1984) is the base of the supracrustal succession on the basis of having a higher grade of metamorphism than the other strata in the basin (Hoffman, 1969; Johnson, 1990). The stratigraphic relationship between the Union Island and Wilson Island groups up until recently had been strictly conjectural, with no known locality displaying a stratigraphic contact between the two groups. A U-Pb zircon age of 2045.8 ± 1.0 Ma for a volcanoclastic unit within the basalt unit by Sheen et al., (2018) provide the first absolute constraints on the depositional age of the Union Island Group and determines that the Union Island Group is the base of the Paleoproterozoic supracrustal succession in the East Arm basin since the felsite from the Wilson Island Group was dated at 1928 ± 11 Ma with the U-Pb zircon method (Bowring et al., 1984).

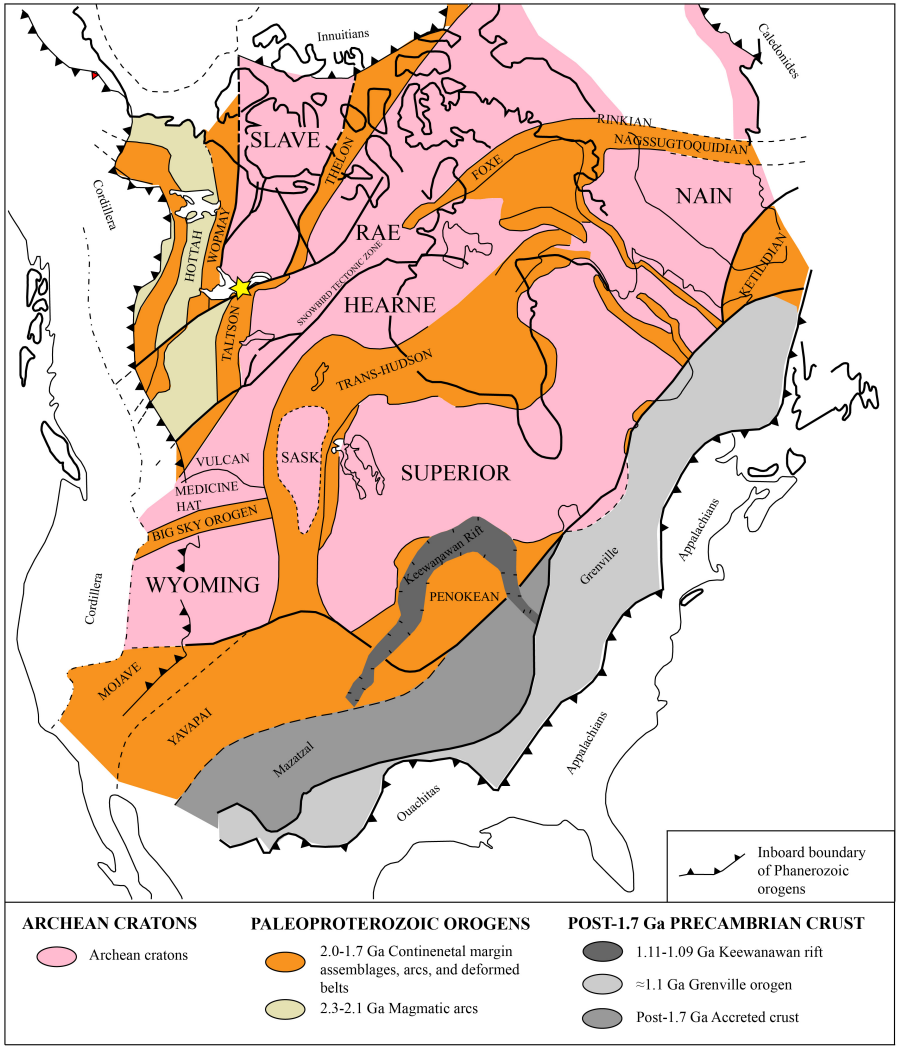

Figure 2.1: Map of the cratons of North America from Hoffman, (1988), and Bleeker and Hall, (2007). The yellow star shows the location of the East Arm basin in the Great Slave Lake.

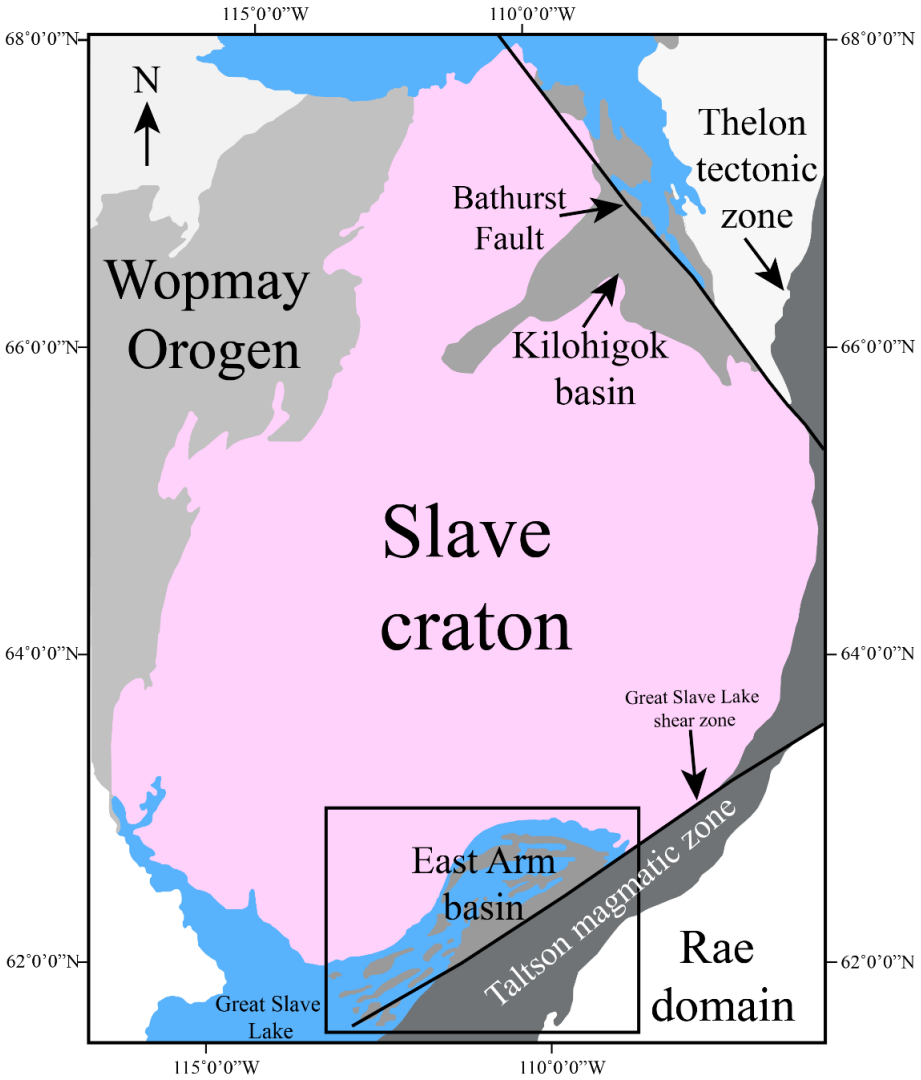

Figure 2.2: A simplified geological map of the Slave craton and surrounding geological terranes modified from the original work Hoffman, (1988a), and Sheen et al., (2018).

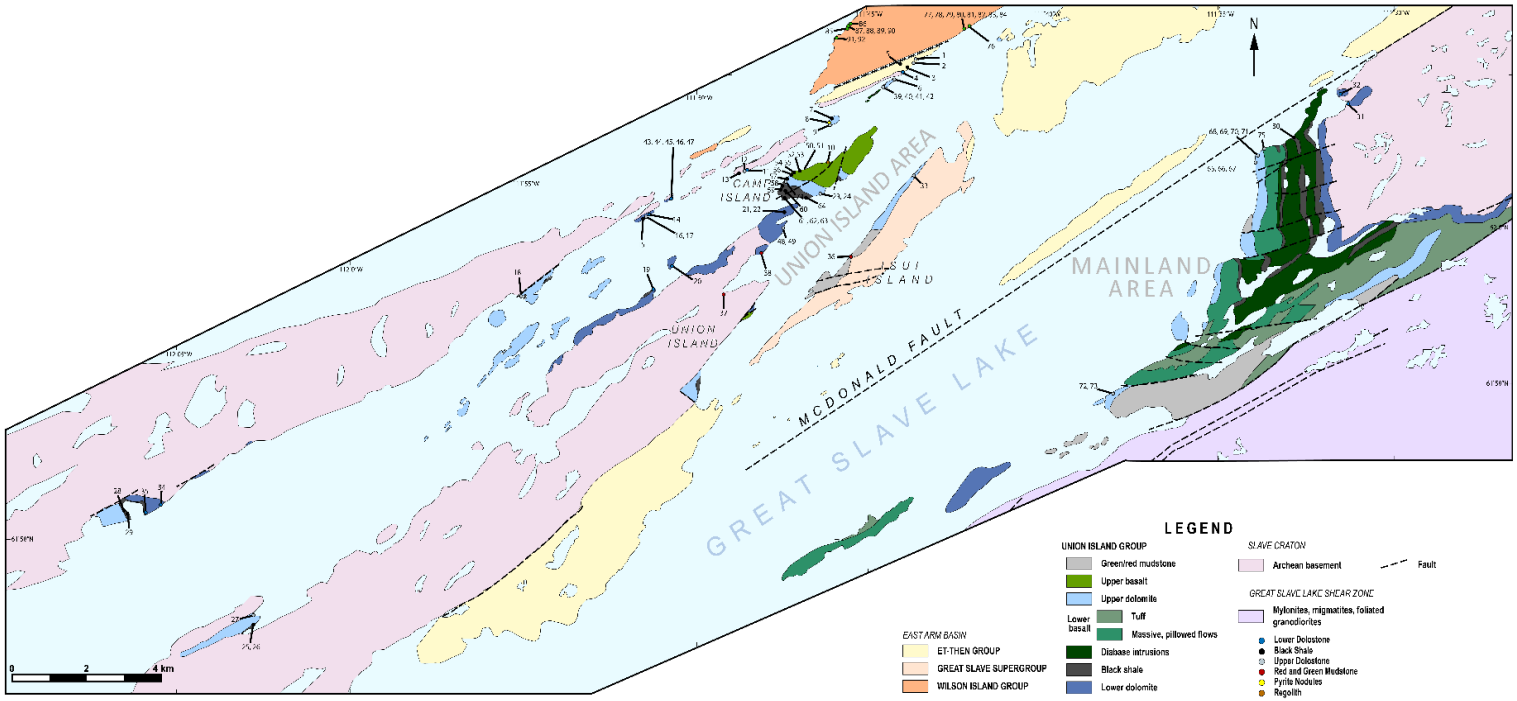

Figure 2.3: Map of the East Arm basin modified from Sheen et al., (2018). Sample localities are marked for the lower dolostone (blue), black shale (black), upper dolostone (gray), and red and green mudstone (red) units. For more information see **Table 1** in the appendices.

The oldest Paleoproterozoic events on the southeastern margin of the Slave craton include emplacement of the 2185-2176 Ma Blatchford Lake Intrusive Suite (Bowring et al., 1984; Mumford et al., 2012; Sinclair et al., 1994) and 2217 ± 4 Ma Simpson Island Dyke to the north of the East Arm basin (Mumford et al., 2012). These magmatic events potentially correlate to the 2231 ± 2 Ma (U-Pb baddeleyite) Malley dyke swarm extending from the central Slave craton to the Kilohigok basin (Buchan et al., 2012) and part of the ca. 2180 Ma Southwest Slave magmatic province including the 2188 +16/-10 Ma Big Spruce Lake alkaline complex (Cavell and Baadsgaard, 1986), the 2181 ± 2 Ma Duck Lake sill, 2180 ± 1 Ma Squalus Lake intrusion (Bleeker and Hall, 2007; Buchan et al., 2010; Mitchell et al., 2014) and reflect extension and rifting on the Slave craton, potentially associated with the mantle upwelling, but the sedimentary record of these events is yet unrecognized on the Slave craton.

Deposition of the Union Island Group at 2045.8 ± 1.0 Ma is proposed to have occurred in a passive rift setting and it represents a five-part failed rift succession (Sheen et al., 2018). Sheen et al., (2018) proposed five stages in the development of the Union Island failed rift based on the earlier works (Hoffman, 1969; Hoffman et al., 1977; Thorstad, 1976), most recent mapping (e.g., Kjarsgaard et al., 2013), and geochemical work: 1) Passive stretching and subsidence with deposition of the lower dolostone unit and the overlying black shale unit. 2) A period of mafic magmatism driven by low-degree, partial melting of a mixed source near the base of a thinned lithosphere during which the lower basalt unit erupted and mafic dikes and sills were emplaced. 3) A hiatus in magmatism resulting in deposition of the upper dolostone unit. 4.) A return to mafic

magmatism sourced from the asthenosphere emplacing the upper basalt unit 5) Deposition of the red and green mudstone. An unconformity marks the contact between the Union Island Group and the overlying ~1.86 Ga Sosan Group of the Great Slave Lake Supergroup (Hoffman, 1988; Hoffman et al., 1977).

The Union Island Group has been inferred to be deposited in a Paleoproterozoic stagnant basin (Hoffman et al., 1977), and marine basinal to platformal setting with intermittent mafic magmatism (Badham and Stanworth, 1977; Sheen et al., 2018). Deposition of most of the succession (lower dolostone, black shale, and basalt units) occurred beneath the wave base, and possibly below the photic zone (Kipp et al., 2018).

In contrast to the conventional view that the Union Island Group was deposited in an open-marine setting, there is growing evidence that the Union Island Group could represent deposition a closed to semi-closed basin with intermittent connection to the ocean. The U-Pb zircon age of 2045.1 ± 1.0 Ma for the volcaniclastic sediments represents an age for eruption of the lower basalt (Sheen et al., 2018). The following 60 to 70 Myr time window after the eruption of the Union Island Group basalts and before voluminous magmatic activity in the adjacent Taltson magmatic zone (<1986 Ma) and deformation along the Great Slave Lake shear zone (<1978 Ma) bears no record of the development and destruction of an ocean basin or subduction along the Slave-Rae lithospheric boundary (Sheen et al., 2018; Snyder and Kjarsgaard, 2013). A lack of

physical evidence for ancient open marine conditions, paired with geochemical data from this study, suggest that the Union Island Group was deposited in a restricted setting.

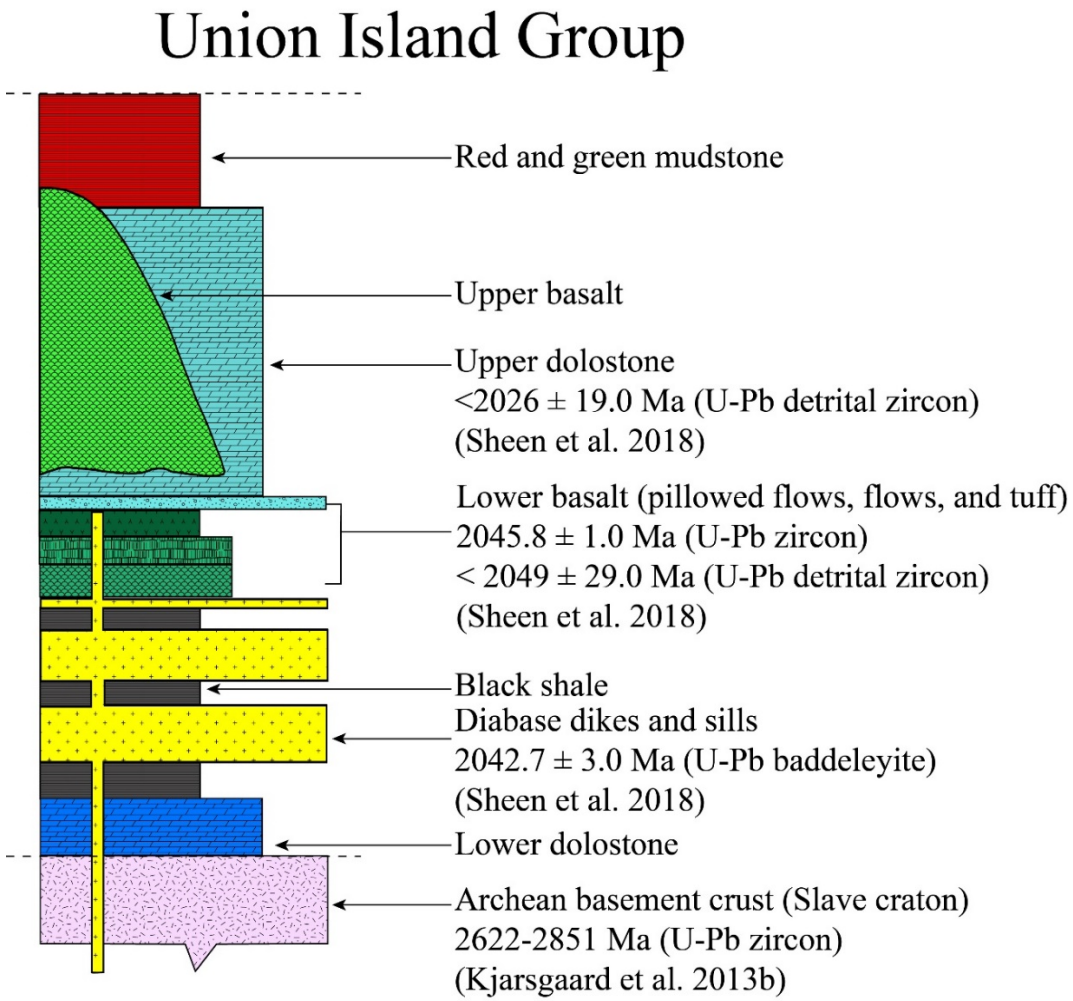

Figure 2.4: Stratigraphy of the Union Island Group with U-Pb geochronologic constraints. Ages for the basalt units and associated dikes and sills as well as ages of detrital zircons are from Sheen et al., (2018). U-Pb dates for the basement are from Kjarsgaard et al., (2013b).

Union Island Group

Lower and Upper Dolostone Units

The lower dolostone unit of the Union Island Group is composed of a generally massive dolostone with complex veining system containing irregular cherty beds and lenses, pelitic layers displaying micaceous parting, and radiaxial dolomite (Hoffman et al., 1977; Sheen, 2017). It has an exposed apparent thickness of the lower dolostone unit is ~200 m (Sheen, 2017). Unconformably overlying the Archean granitic basement (**Figure 2.4**), there is a locally developed layer of quartz-rich regolith derived from the underlying weathered granites of the Slave craton (Hoffman et al., 1977; Sheen, 2017). Deposition is thought to have occurred during the first stage of rifting.

The Union Island Group upper dolostone unit is ~200 m thick (Sheen, 2017), and comformably overlies the Union Island Group black shale unit (**Figure 2.4**) (Sheen, 2017; Thorstad, 1976). Unlike the lower dolostone unit, the upper dolostone unit is well bedded and contains silt- to sand-sized grains with red to green mudstone forming interbeds, and a stromatolitic interval that has been reported on the northeastern tip of Union Island (Sheen, 2017). Deposition of the upper dolostone unit is inferred to have occurred during the third stage of rifting (Sheen et al., 2018).

Figure 2.5: Fine lamination and ripples in the upper dolostone unit. Rock hammer for scale.

Black Shale Unit

The black shale unit of the Union Island Group has an estimated thickness of ~500 m (Sheen, 2017) and unconformably overlies the lower dolostone unit of the Union Island Group (**Figure 2.4**, Thorstad, 1976). It is intruded by diabase sills and is composed of massive to laminated, moderately fissile carbonaceous black shale with dolomitic mudstone interbeds (Hoffman et al., 1977; Sheen, 2017; Thorstad, 1976). Disseminated and nodular pyrite commonly occur throughout the unit (Thorstad, 1976; Sheen, 2017).

Samples of the black shale unit show variable degrees of silicification. It is inferred that the black shale unit was deposited during the first stage of rifting, after deposition of the lower dolostone unit, due to continued subsidence of the Slave craton and a transgression (Sheen et al., 2018).

Red and Green Mudstone

The red and green mudstone unit is finely laminated mud to siltstone, and commonly includes dolostone. It is been reported to conformably overlie massive tuffs of the lower basalt unit, the upper dolostone unit, and the upper basalt unit (**Figure 2.4**) (Sheen, 2017; Thorstad, 1976). It is ~400 m thick, and has black shale, mudstone with concretions, and dolostone beds towards the base of the unit, but grading occurs further up-section (Sheen, 2017). Convolute bedding, and micro-faults have also been reported to commonly occur (Sheen, 2017).

Wilson Island Group

The 1928 ± 11 Ma Wilson Island Group (Bowring et al., 1984) contains Paleoproterozoic volcanic and sedimentary rocks allocthonous in the East Arm basin (Kjarsgaard et al., 2013). Geochronologic constraints obtained by U-Pb zircon dating (Bowring et al., 1984) from a felsic flow or dome (Johnson, 1987a) intruding the Rheinhardt Formation provided an age for deposition of the Wilson Island Group

(Johnson, 1990). The four formations that compose the Wilson Island Group in ascending order are: 1) the Rheinhardt Formation, 2) the Safety Cove Formation, 3) the Five Snares assemblage, and 4) the Basile Bay Formation (Johnson, 1990; Kjarsgaard et al., 2013). In the East Arm basin, fragments of the Wilson Island Group can be found from Outposts Islands northeastward to Basile Lake (Johnson, 1990). The dextral McDonald-Wilson fault offsets the upper Five Snares Formation and Basil Bay Formation northeastward from the lower Rheinhardt Formation and Safety Cove Formation (Hoffman, 1977; Johnson, 1990). Correlation between the two areas was inferred based on the sequence at the top of the stratigraphic section at Wilson Island resembling the lower part of the stratigraphic section at Basile Bay that is inferred to represent a continuous section (Johnson, 1990). The most thorough study of the Wilson Island Group was conducted by Johnson, (1990), and provided in depth description of the individual formations that is summarized herein. The Rheinhardt Formation is composed of intercalated mafic and felsic metavolcanic rocks and clastic metasedimentary rocks, with the base truncated by a major fault. The Safety Cove Formation (see description below), which is the focus of this study, consist of a mixed quartz sandstone and carbonate succession. The Five Snares assemblage is made up of siliciclastic and dolomitic metasedimentary rocks, and the Basile Formation consists of a thick succession of predominantly siliciclastic metasedimentary rocks.

Safety Cove Formation

Detailed stratigraphic description of the Safety Cove Formation was conducted by Johnson, 1990, and their description of the Safety Cove Formation is summarized here. The Safety Cove Formation of the Wilson Island Group overlies the Reinhardt Formation, and is a mixed quartz sandstone and carbonate succession, deposited on a coastal braidplain that maintained connection to shallow-marine platform or epeiric sea through a fan-delta distributaries or tidal channels (Johnson, 1990). It is composed of five members, in ascending order: 1) lower arkose member, 2) dolomitic sandstone member, 3) middle arkose member, 4) sandy dolostone member, and 5) upper mixed member. The lower arkose member is ~700 m thick and composed of fine- to medium-grained feldspathic sandstone, with planar lamination, trough cross-bedding, and ripple laminations. Pelitic laminae, wavy and lenticular bedding, rhythmically laminated sandstone and mudstone, and ball and pillow structures are also found. Deposition of the lower arkose member is thought to have occurred in a distal braidplain setting. The dolomitic sandstone member is ~550-650 m thick and contains intercalated dolostone and sandstone. Trough and planar cross-bedding are frequently seen as well as pebbly lags between feldspathic and dolomitic sandstones. Deposition is inferred to have occurred in a marginal to platform setting. The middle arkose member is composed of feldspathic sandstone with planar lamination and trough cross-bedding. It is thought to have been deposited in a combination of settings including tidal channels, distal part of an alluvial braidplain, and sand flats or subtidal bars (Johnson, 1990). The overlying sandy dolostone member is a carbonate-dominated, mixed carbonate-siliciclastic succession.

The uppermost unit, upper mixed member, is the feldspathic sandstone-dominated, mixed carbonate-siliciclastic succession. The dolomitic sandstone, sandy dolostone, and upper mixed members are all mixed siliciclastic and carbonate sediments reflecting deposition in a setting where sediments were delivered from terrigenous sources as well as produced in marginal to platform-marine settings. Stratigraphically above the Safety Cove Formation is the lowermost member of the Five Snares Assemblage.

Chapter 3: Methods

One hundred twenty-one carbonates, twenty-six black shales, three red and green mudstones, and one gray shale from the East Arm basin (the Union Island and Wilson Island groups) were collected in the summer of 2015 and September of 2016. The Union Island Group samples were collected from the lower dolostone, black shale, upper dolostone, and red and green mudstone units, while the Wilson Island Group samples were taken from the Safety Cove Formation (Johnson, 1990).

For $\delta^{13}C_{carb}$ and $\delta^{18}O_{carb}$ analysis, ~250 µg carbonate powders were weighed out into vials and flushed with Airgas ultra-high purity He in a heating block. Carbonate samples were acidified with 100% phosphoric acid (McCrea, 1950) and held at 50°C in the heating block for 24 hours to allow complete dissolution of carbonate minerals. Isotopic composition for carbonate carbon and oxygen were measured using a Thermo Finnigan Delta V Advantage isotope-ratio mass spectrometer in a continuous-flow mode on phosphoric acid liberated CO_2 gas and expressed using conventional δ notation as per mil differences from the international Vienna-Pee Dee Belemnite (VPDB) standard. Data is reported with an analytical error of 1σ, and was better than 0.1 ‰ for carbon and 0.2 ‰ for oxygen isotope data. Data was calibrated against international and internal laboratory standards. International standards used were NBS 18 ($\delta^{13}C$ = -5.01 ‰, $\delta^{18}O$ = -23.0 ‰) and NBS 19 ($\delta^{13}C$ = 1.95 ‰, $\delta^{18}O$ = -2.20 ‰). Internal standards used were UC Davis Calcite ($\delta^{13}C$ = 2.09 ‰, $\delta^{18}O$ = -1.91 ‰), UCR Calcite ($\delta^{13}C$ = -1.78 ‰, $\delta^{18}O$ = -17.95 ‰), M-dolomite ($\delta^{13}C$ = -8.76 ‰, $\delta^{18}O$ = -18.78 ‰), NBS 88b ($\delta^{13}C$ = 2.17 ‰, $\delta^{18}O$ = -

7.59 ‰), and Tytiri dolomite ($\delta^{13}C$ = 0.78 ‰, $\delta^{18}O$ = -7.07 ‰). A calibration line was calculated by least squares linear regression using the known UC Davis calcite and NBS 18 measured isotope values of the standards. To check the quality of analysis, one calibrated international calcite standard (NBS 19) and one calibrated internal dolomite standard (Tytiri) were analyzed together with unknown samples (Turner and Bekker, 2015). Values obtained for NBS 19 were $\delta^{13}C = 1.7 \pm 0.18$ ‰ and $\delta^{18}O = -2.10 \pm 0.21$ ‰ (n = 19) and for Tytiri were $\delta^{13}C = 0.73 \pm 0.01$ ‰ and $\delta^{18}O = -5.74 \pm 0.16$ ‰ (n = 24).

Mineralogical identification of calcite and dolomite minerals was done following the three-step staining method of Dickson, 1965, using 1.5% hydrochloric acid, alizarine red S, and potassium ferricyanide. Data correction of oxygen isotopes for dolomite versus calcite was based on the results of staining.

Major (Ca, Mg, Fe, and Mn) and trace (Sr) element concentrations in 50 carbonates of the upper and lower dolostone units were measured by ICP-MS at the geochemical laboratory in the Department of Geosciences and Geography, University of Helsinki. Analysis was performed by placing 10 mg of sample powder into 15 mL plastic test tubes and acidifying with 0.5 N acetic acid. Magnetic stirring bars were added, and samples were spun on a shaking table for 18 hours at 100 motions per minute. Samples were then centrifuged for 7 minutes at 2500 rpm. 0.1 mL of sample solution was added into a 10 mL ICP-MS test tube and diluted to 10 mL with 50 µL of dilute (1:100) HNO_3. International carbonatite reference standards SARM-40 and COQ-1 were used during the run. Reproducibility was within 10% of the certified values for Ca and Sr. Yields for Fe,

Mn, and Mg were lower, likely reflecting elements bound in silicate rather than carbonate phases.

Twenty-four black shale, red and green mudstone, and gray shale samples were analyzed at the Bureau Veritas Cooperation Commodities Division, where they underwent a full digest using a lithium metaborate/tetraborate fusion, obtaining major and trace element concentrations using inductively coupled plasma emission spectroscopy (ICP-ES) and inductively coupled plasma mass spectrometry (ICP-MS). Gold (Au) and volatile element concentrations were obtained through an aqua regia digestion.

For organic carbon isotope analysis, ~10 g splits of carbonate powders were acidified for at least 3 hours using 12 N HCl in 50 mL centrifuge tubes. For black shale and red and green mudstone samples, 50-100 mg sample powders were acidified using 6N HCl in 50 mL centrifuge tubes. Magnetic stir bar was spun at 150 rpm during acidification to prevent formation of carbonate crust, and vials were periodically vortexed to ensure complete decarbonation. They were then centrifuged at 2500 rpm for two-minute intervals, acid was decanted and powders were washed with deionized water. The process was repeated four times per sample to ensure removal of residual acid. Decarbonated and dried insoluble residue of ~5-10 mg from carbonate powders, black shale and red and green mudstone samples were weighed into 9 x 10 mm tin weigh boats for organic carbon isotope analysis. Organic carbon isotope ratios for shales were measured using the Costech EA 4010, Thermo-Finnigan Delta V Advantage mass spectrometer, and Conflo IV open-split interface system. Unknowns were corrected

against Acetanilide ($\delta^{13}C$ = -28.27 ‰), Hawaii glycine ($\delta^{13}C$ = -36.02 ‰), and USGS SDO-1 ($\delta^{13}C$ = -30.0 ‰). Analytical error was better than 0.1 ‰ for organic carbon (1σ).

Nitrogen isotope analysis of black shale and red and green mudstone samples was conducted by weighing ~40 mg powder of decarbonated black shale into 9 x 10 mm tin weigh boats, and ~100 mg of decarbonated red and green mudstone into 8.5 x 13 mm tin weigh boats. Sample powders were decarbonated using 6 N HCl and underwent the same vortexing and deionized water treatment as for organic carbon. Isotope values were measured using a Costech EA 4010, Thermo-Finnigan Delta V Advantage mass spectrometer, and Conflo IV open-split interface and were better than 0.3 ‰ (1σ). Data are reported in delta notation relative to air and were calibrated against international standards: USGS SDO-1 ($\delta^{15}N$ = -0.8 ‰), SGR-1 ($\delta^{15}N$ = 17.4 ‰), USGS40 ($\delta^{15}N$= -4.52 ‰), and USGS41a ($\delta^{15}N$= 47.55 ‰). Internal standards used were Acetanalide ($\delta^{15}N$ = -0.41 ‰), Hawaii Glycine ($\delta^{15}N$= 11.40 ‰), and Mt. McRae Shale ($\delta^{15}N$ = 6.28 ‰) reference standards. Samples were combusted using oxygen input from a macroloop at 1025°C and passed through a reduction column at 650°C. Tin blanks were run in between each sample as to negate memory effects from residual material left over from the prior combustion.

Fe-speciation was conducted on twenty black shale samples, one gray shale, and three red and green mudstone samples using an Atomic Absorption Spectrometer (AAS) at the Cohen Geochemistry Lab at the University of Leeds in order to constrain whether the Union Island Group black shales were deposited under oxic or anoxic (euxinic or ferruginous) conditions. The highly reactive iron (Fe_{HR}) includes four components that

were quantified in order to evaluate the ratio of highly reactive iron to total iron (Fe_T) (Berner, 1970; Lyons et al. 2009; Raiswell et al. 1988). Highly reactive iron is a sum of iron bound in carbonates (Fe_{carb}), oxides (Fe_{ox}), mixed valence or highly crystalline oxides (Fe_{mag}), and pyrite (Fe_{py}); $Fe_{HR} = Fe_{carb} + Fe_{ox} + Fe_{mag} + Fe_{py}$ (Poulton and Canfield, 2005). By plotting the ratios of Fe_{HR}/Fe_T against Fe_{py}/Fe_{HR}, redox conditions, such as oxic, ferruginous, or euxinic, can be constrained. Iron extraction was conducted in a four-step process described in Poulton and Canfield, 2005: 1) Fe-bearing carbonate phases (siderite and ankerite) were extracted by treating sample powders with a buffered sodium acetate solution for 48 hours. 2) Sample powders were then treated with a buffered sodium dithionite solution for 2 hours to extract labile iron oxides. 3) Sample powders were then treated with a buffered ammonium oxalate solution for 6 hours to extract Fe from mixed valence or highly crystalline oxides (magnetite). 4) Extraction of all reduced sulfur bound in sulfides (predominantly pyrite) was carried out using a 2 hour hot chromous chloride/HCl distillation, which quantitatively captured sulfur as AgS using an $AgNO_3$ trap solution. Concentrations of the iron pools (Fe_{carb}, Fe_{ox}, Fe_{mag}, and Fe_{py}) were measured on AAS at the Cohen Geochemistry Lab of the University of Leeds.

Twenty-six carbonate samples were analyzed for Rb and Sr isotopes using a stepwise dissolution method. The sample powder of dolostone (~100 mg) was first treated with 0.01 N hydrochloric acid at room temperature, and then dissolved in 1N HCl solution at 60°C. Sr was subsequently eluted from an ion-exchange column filled with Dowex AG50W×8 resin using 2.5 N HCl.

Sm-Nd isotope analyses were measured using isotope dilution mass-spectrometry on four black shale, three red and green mudstone, and one gray shale samples at the Laboratory of Isotope Chemostratigraphy and Geochronology at the Russian Academy of Sciences, St. Petersburg, Russia. For isotope analysis, a mixed ^{150}Nd-^{149}Sm spike was added to each shale sample powder (~50 mg) and the samples were then dissolved in a mixture of concentrated HCl+HNO_3+HF acids at a temperature of 110°C. The solution was dried and the residue was re-dissolved in a mixture of concentrated HCl+HNO_3 acids and dried again. The residue was re-dissolved a third time in concentrated HCl. REE were eluted from the ion-exchange column filled with Dowex AG50W×8 resin using 4N HCl. The cut with REE chlorides was then loaded on the second ion-exchange column filled with LN-C50-A (Elchrom) resin to separately elute Nd and Sm in 0.5 N HCl.

Isotope compositions of Sr, Sm, and Nd were measured on a multi-collector Triton TI thermal ionization mass-spectrometer in static collection mode using a Re filament at the Laboratory of Isotope Chemostratigraphy and Geochronology at the Russian Academy of Sciences, St. Petersburg, Russia. The average ^{87}Sr/^{86}Sr value for the NIST SRM-987 strontium carbonate isotope standard measured during this study was 0.710282 ± 0.000008 (2σ, n=14). The average ^{143}Nd/^{144}Nd value measured for the jNd-1 isotope standard during this study was 0.512098 ± 0.000008 (2σ, n=6). Procedural blanks during this study were less than 3 ng for Sr, 0.05 ng for Sm, and 0.2 ng for Nd. Values for εNd(T) and TDM were calculated using the following values for CHUR and DM, respectively: ^{143}Nd/^{144}Nd = 0.512638, ^{147}Sm/^{144}Nd = 0.1967 and ^{143}Nd/^{144}Nd = 0.513151, ^{147}Sm/^{144}Nd = 0.2136.

Eleven total dolostone samples, 6 from the lower dolostone unit and 5 from the upper dolostone unit, and 10 black shale samples were analyzed for REE + Y by ICP-MS (Element XR, Thermo Finnigan) at the Metal Geochemistry Center at Yale University using a quartz spray chamber introduction system. An aliquot of 6 N stock solution was diluted using 5 % HNO_3 after total digests to obtain REE + Y concentrations and was measured in medium resolution. The USGS BHVO geostandard was processed throughout the run and is within ± 10 % of the reported value. Pure element standard was used to check for oxide interference, but no corrections were required.

Chapter 4: Results

Carbon and oxygen isotope values of carbonates

Carbon isotope values for the forty-four lower dolostone unit samples are highly positive, ranging between +2.2 and +9.5 ‰ VPDB, with the average value of +7.4 ‰ (**Figure 4.1, Table 2**). Carbon isotope values for sixty-one upper dolostone unit samples are significantly lower, with an average value of +0.5 ‰, and the full range between -8.3 and +2.8 ‰. Oxygen isotope values for the lower dolostone unit range between -15.8 and -6.7 ‰ VPDB and averaged -9.1 ‰. The upper dolostone unit $\delta^{18}O_{carb}$ values were on average lighter at -10.5 ‰ and ranged between -18.5 and -5.6 ‰.

Carbonate carbon isotope analysis was also conducted on 12 Union Island black shale unit containing more than 50 % of carbonate. All analyses yielded slightly negative carbon isotope ratio values ranging between -4.5 and -0.5 ‰, with an average value of -1.9 ‰.

Carbon isotope ratio values for the overlying Wilson Island Group dolostones are near-to-zero and range between -3.3 and +1.7 ‰, with the average value of +0.1 ‰. Samples with negative carbon isotope values from the Wilson Island Group have dolomite cements with quartz grains and could record composition of diagenetic fluids. Oxygen isotope values of the Wilson Island Group carbonates are on average lighter than those for the Union Island Group dolostones. Their $\delta^{18}O_{carb}$ values range between -17.7 and -10.1 ‰, with an average of -13.4 ‰, consistent with a stronger alteration with respect to carbonates of the Union Island Group.

Diagenetic screening

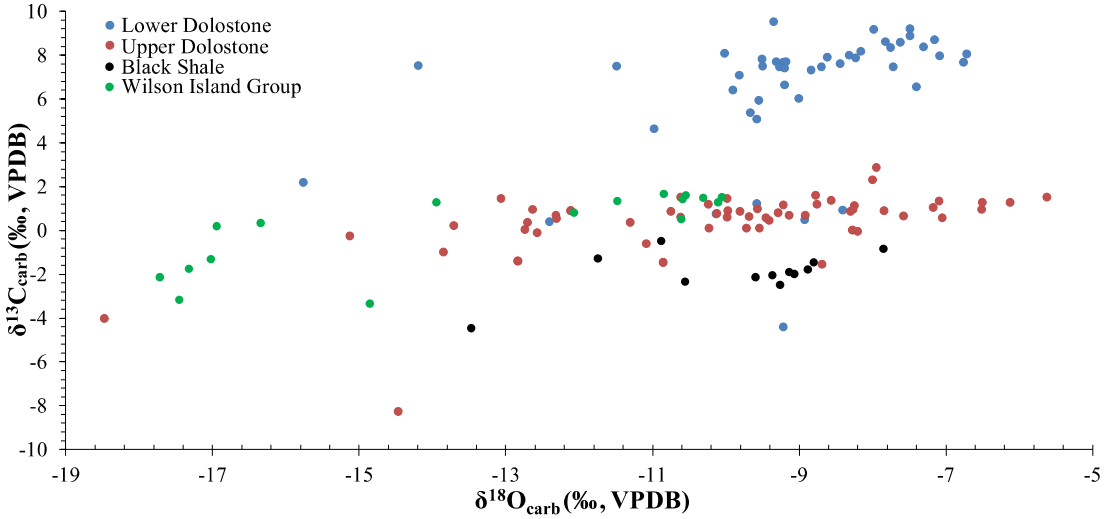

Figure 4.1: Plot of $\delta^{13}C_{carb}$ against $\delta^{18}O_{carb}$. Positive correlation for the lower dolostone unit samples (blue; $R^2 = 0.15$), red and green mudstone (red; $R^2 = 0.31$), black shale (black; $R^2 = 0.29$), and Safety Cove Formation (green; $R^2 = 0.62$) samples suggests that the isotope composition of the Union Island Group and Wilson Island Group carbonates might have been affected by post-depositional processes.

Organic carbon isotope ratios and total organic carbon content

Total organic carbon (TOC) content for both the lower and upper dolostone units is low. The TOC content of the lower dolostone unit ranges between 0.01 and 0.68 wt %, but with an average value of 0.04 wt %. The upper dolostone unit TOC content ranges between 0.01 and 0.08 wt % and has an average value of 0.03 wt %.

TOC content for the black shale unit, red and green mudstone, and gray shale samples is highly variable (**Figure 4.2, Table 3**). Black shales have the highest organic carbon content, reaching as high as 6.3 wt % of organic carbon. The average TOC content for black shale samples was 2.6 wt %, with a minimum organic carbon content of 0.3 wt %. Red and green mudstones have lower organic carbon content, with the TOC

content for all three samples being 0.04 wt %. The gray shale sample also has low organic carbon content, 0.1 wt %, but higher than that for the red and green mudstone samples.

$\delta^{13}C_{org}$ values for the lower dolostone unit range from -42.1 ‰ to -22.7 ‰, with the average value of -31.1 ‰. The negative $\delta^{13}C_{org}$ values for this unit combined with highly positive carbon isotope values for carbonates yields $\Delta^{13}C$ ($\delta^{13}C_{carb}$ - $\delta^{13}C_{org}$) values as high as 50.0 ‰, with an average value of 39.0 ‰. $\delta^{13}C_{org}$ values for the upper dolostone unit range were on average lower than the lower dolostone, ranging between -37.5 ‰ and -22.1 ‰ and with an average value of -29.5 ‰. The $\Delta^{13}C$ value for the upper dolostone was as high as 38.0 ‰ and averaged 29.5 ‰.

The organic carbon isotope composition of black shales from the Union Island Group is ^{13}C-depleted, averaging -39.4 ‰, and reaching as low as -43.1 ‰ (**Figure 4.2**). The most enriched $\delta^{13}C_{org}$ value recorded is -33.2 ‰. Measuring the $\Delta^{13}C$ values for the twelve samples that underwent carbonate analysis yielded an average fractionation between the carbon pools of 37.5 ‰. The red and green mudstones have more ^{13}C-enriched carbon isotope values compared to the black shales, ranging between -27.8 and -26.6 ‰, with the average of -27.1 ‰. A gray shale sample yielded an organic carbon isotope ratio value of -31.8 ‰.

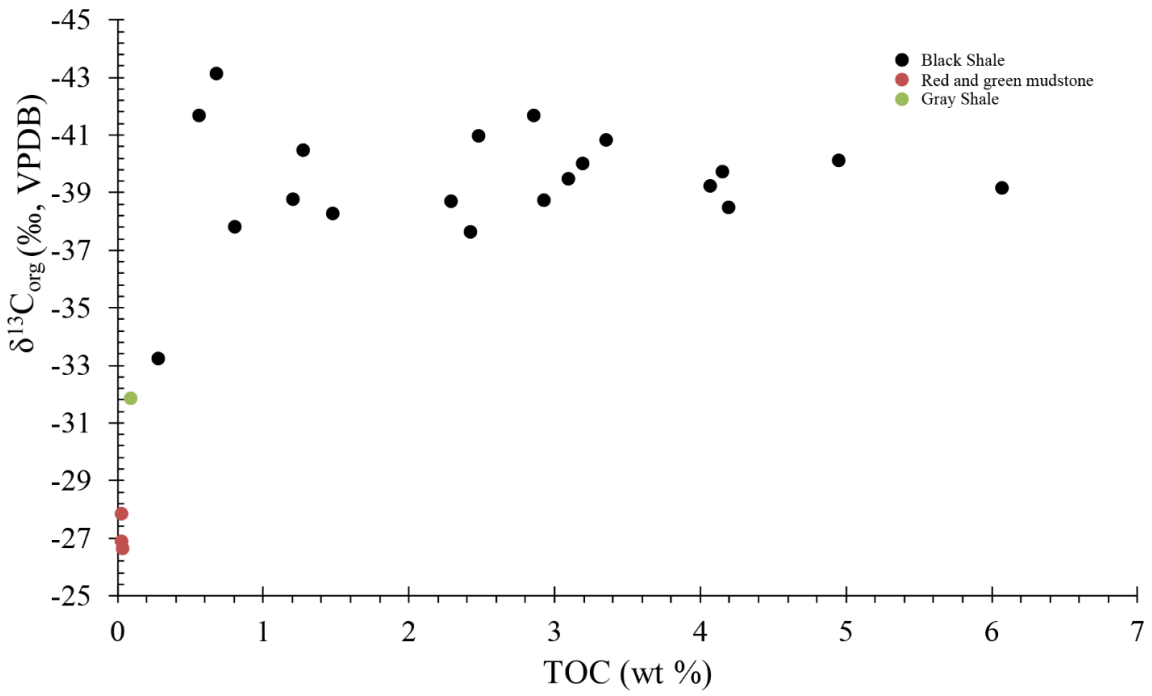

Figure 4.2: Plot of TOC content vs. $\delta^{13}C_{org}$ values. Invariable $\delta^{13}C_{org}$ values with a large range of TOC content indicates that the carbon isotope values of black shales, red and green mudstones, and gray shale have not been significantly altered.

Sr concentrations and isotope values

Strontium concentrations and isotope values were measured for carbonates from both the lower and upper dolostone units (**Figure 4.3, Table 2**). Sr concentrations are generally higher in the lower dolostone unit. The lower dolostone unit Sr concentrations range between 22.2 and 150.5 ppm, with an average concentration of 70.8 ppm. In contrast, the upper dolostone unit Sr concentrations range between 19.1 and 68.3 ppm, with an average concentration of 32.3 ppm. Both the lower and upper dolostone units have $^{87}Sr/^{86}Sr$ values significantly higher than those inferred for the Paleoproterozoic seawater (Veizer and Compston, 1976). The lower dolostone unit $^{87}Sr/^{86}Sr$ ratios range

between 0.708 and 0.756, with an average ratio of 0.722. The upper dolostone unit $^{87}Sr/^{86}Sr$ ratios are higher compared to the lower dolostone unit, with $^{87}Sr/^{86}Sr$ ratios ranging between 0.710 and 0.764, with an average ratio of 0.734.

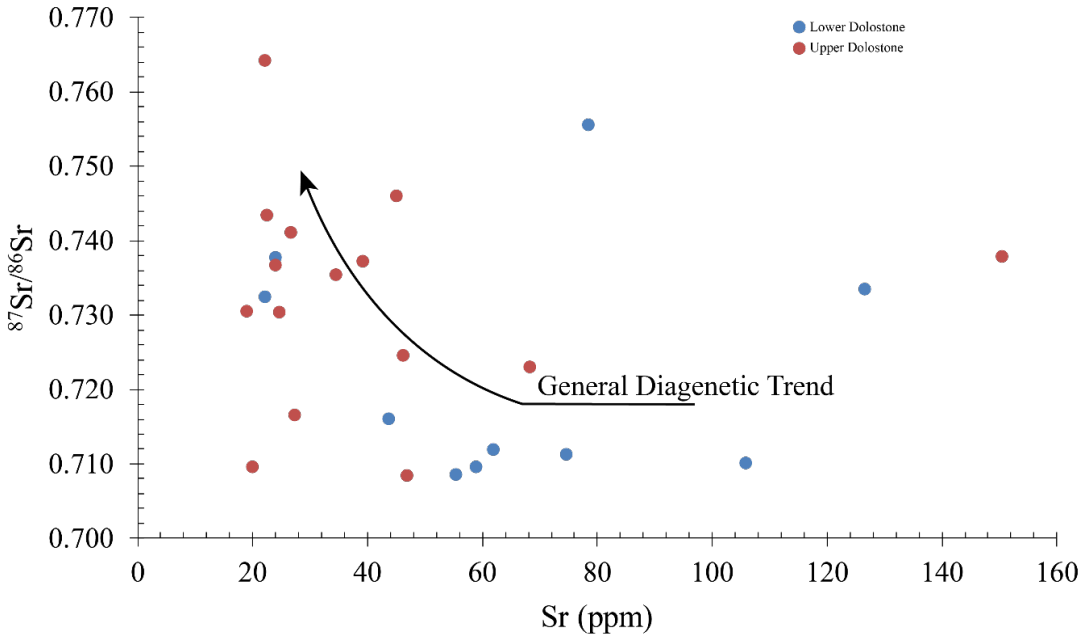

Figure 4.3: Sr concentrations for the upper (red) and lower (blue) dolostone units of the Union Island Group. Trend towards higher $^{87}Sr/^{86}Sr$ ratios with decreasing Sr content (black line) has been linked to diagenetic overprint (e.g., Banner and Hanson, 1990). Lack of such pattern for the lower dolostone ($R^2 = 0.01$) and upper dolostone ($R^2 \approx 0$) units might reflect preservation of a primary depositional Sr isotope signal even though the Sr isotope values are too high for contemporaneous Paleoproterozoic seawater.

Fe and Mn concentrations in the lower and upper dolostones

Both lower and upper dolostone samples were analyzed for Fe and Mn concentrations. Lower dolostone carbonates had Fe concentrations ranging between 3390.61 and 23660.15 ppm with an average of 7675.18 ppm. Upper dolostone samples in general we Fe-enriched compared to lower dolostone samples, with concentrations ranging between 5723.55 and 27429.04 ppm with an average of 15564.29 ppm.

Manganese content for the lower dolostone ranged between 427.74 and 1833.39 ppm with an average of 907.10 ppm. Upper dolostone samples were Mn-enriched compared to lower dolostone samples, with Mn concentrations ranging between 328.19 and 3433.49 ppm with an average of 1198.08 ppm.

Mn/Sr ratios in the lower and upper dolostones

Both the lower and upper dolostone units recorded Mn/Sr ratios above crustal values (Rudnick and Gao, 2013, **Figure 4.4, 4.5**). Mn/Sr ratios for the lower dolostone ranged between 5 and 62 and an average of 20. Upper dolostone samples record on average higher Mn/Sr ratios with a range between 17 and 146 and an average of 35.

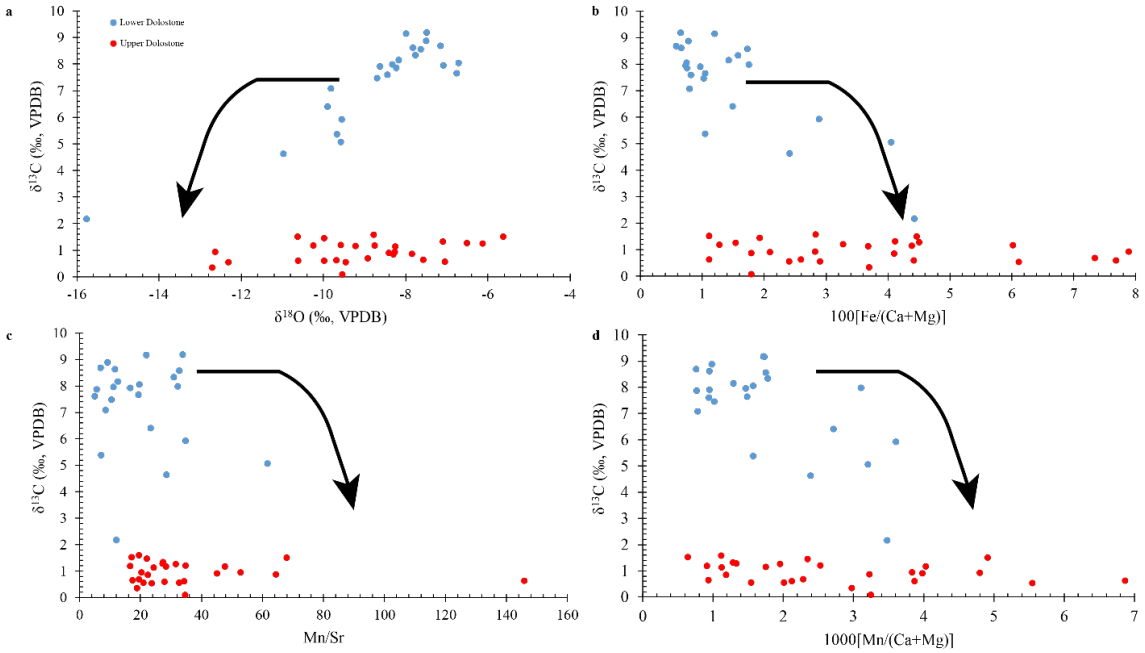

Figure 4.4: Diagenetic cross plots for carbon isotope values of Union Island Group lower (blue) and upper (red) dolostones with general diagenetic trends shown (black arrows, cf. Bekker et al., 2016): (**a**) $\delta^{13}C$ vs. $\delta^{18}O$; (**b**) $\delta^{13}C$ vs 100[Fe/(Ca+Mg)] molar ratios; (**c**) $\delta^{13}C$ vs Mn/Sr weight ratios; and (**d**) $\delta^{13}C$ vs 1000[Mn/(Ca+Mg)] molar ratios. Slight positive covariation between $\delta^{13}C$ values and $\delta^{18}O$ towards lighter values suggests that isotope values for lower and upper dolostone might have been subjected to alteration by post-depositional processes. The absence of $\delta^{13}C$ trending towards lighter values with increasing concentrations of Fe, Mn, and Mn/Sr ratios suggests carbon isotope values have not been highly affected by post-depositional alteration.

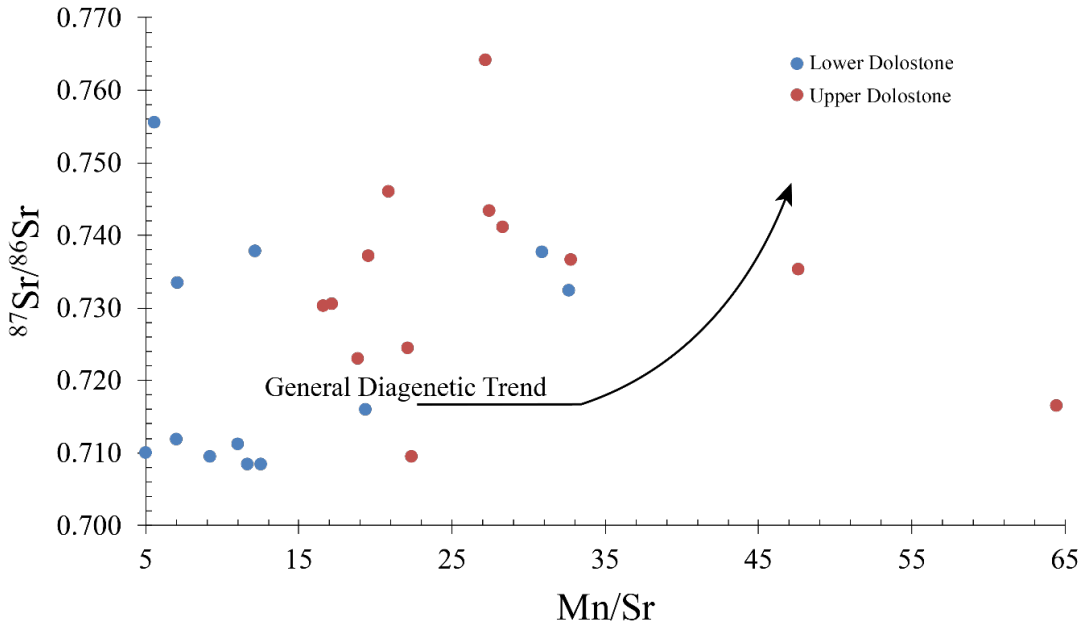

Figure 4.5: $^{87}Sr/^{86}Sr$ vs Mn/Sr ratio for upper (red) and lower (blue) dolostone units of the Union Island Group (cf. Melezhik et al., 2005c). Trends towards higher $^{87}Sr/^{86}Sr$ values with increasing Mn/Sr ratios (black line) has been connected to post-depositional alteration (Veizer et al., 1992a). The absence of such as pattern for the lower dolostone ($R^2 = 0.04$) and upper dolostone ($R^2 = 0.02$) units could reflect a primary Sr depositional signal despite the highly radiogenic Sr isotope values.

Rare-earth elements in the lower and upper dolostones

REE + Y concentrations are normalized to the PAAS values from Taylor and McLennan, (1985), and REE + Y patterns for the lower dolostone and upper dolostone are shown in **Figure 4.6**. Lower dolostone samples contained are characterized by a negative Ce_{SN} anomaly ($Ce/Ce^*_{SN} = 0.89$), and positive Eu_{SN} anomaly ($Eu/Eu^*_{SN} = 1.14$). They also record light rare-earth element (LREE) depletion compared to heavy rare-earth element (HREE) based on the ratio of Pr/Yb_{SN} (cf., Bau and Dulski, 1996; Pr/Yb_{SN} = 0.79), and middle rare-earth element (MREE) enrichment compared to HREE as shown by the ratio of Sm/Yb_{SN} (cf. Bolhar and Van Kranendonk, 2007; $Sm/Yb_{SN} = 1.12$). Upper

dolostone samples record similar patterns to the lower dolostone and record a negative Ce_{SN} anomaly (Ce/Ce^*_{SN} = 0.91), and positive Eu anomaly (Eu/Eu^*_{SN} = 1.13). There is a nearly flat LREE to HREE patterns as reflected by Pr/Yb_{SN} ratios (cf., Bau and Dulski, 1996; Pr/Yb_{SN} = 0.94) and MREE enrichment compared to HREE based on Sm/Yb_{SN} ratios (cf. Bolhar and Van Kranendonk, 2007; Sm/Yb_{SN} = 1.25).

Y/Ho ratios

Y/Ho ratios measured for both the lower and upper dolostone were above chondritic Y/Ho ratios of ~ 26 (Bolhar et al., 2004). The lower dolostone samples contain Y/Ho ratios ranging between 33.5 and 63.6 and averaged 43.9. Upper dolostone samples recorded Y/Ho ratios that were lower, ranging between 28.3 and 48.2 and averaged 37.5.

Cerium anomaly

Cerium anomalies for lower dolostone and upper dolostone samples from the Union Island Group were calculated using the formula of Bau and Dulski, (1996) [$Ce/Ce^*_{SN} = Ce_{SN}/(0.5*La_{SN} + 0.5*Pr_{SN})$] and were normalized to PAAS (**Figure 4.13**). Ce/Ce^*_{SN} values were plotted against Pr/Pr^*_{SN} values [$Pr_{SN}/(0.5*Ce_{SN} + 0.5*Nd_{SN})$] (Bau and Dulski, 1996) to distinguish between true negative Ce_{SN} anomalies and potentially anomalous abundances of La (Bau and Dulski, 1996). Lower dolostone Ce/Ce^*_{SN} values ranged 0.87 and 0.91 and averaged 0.89. Only one lower dolostone sample (UN-16-31-19m) plotted within the field that represents a true negative Ce_{SN} anomaly. All other lower dolostone samples plotted within the field that represents a positive La_{SN} anomaly and no negative Ce_{SN} anomaly (Bau and Dulski, 1996). Upper dolostone Ce/Ce^*_{SN} values

were similar to lower dolostone values, ranging between 0.85 and 0.95 with an average of 0.91. All upper dolostone samples except one (UN-16-27-128.5m) plotted within the field representing a true negative Ce_{SN} anomaly (**Figure 4.13**). UN-16-27-128.5m plotted within the field that represents neither a positive La_{SN} anomaly or true negative Ce_{SN} anomaly.

Europium anomaly

Europium anomalies for the lower dolostone and upper dolostone units of the Union Island Group were calculated following the formula: [$Eu/Eu^*_{SN} = Eu_{SN}/(0.67*Sm_{SN} + 0.33*Tb_{SN})$] (Bau and Dulski, 1996). Both lower and upper dolostone samples record positive Eu/Eu^*_{SN} anomalies. Lower dolostone Eu/Eu^*_{SN} values ranged between 0.83 and 1.42 with an average of 1.14. Upper dolostone samples record Eu/Eu^*_{SN} values ranging between 0.83 and 1.29 and average 1.13 (**Figure 4.6**).

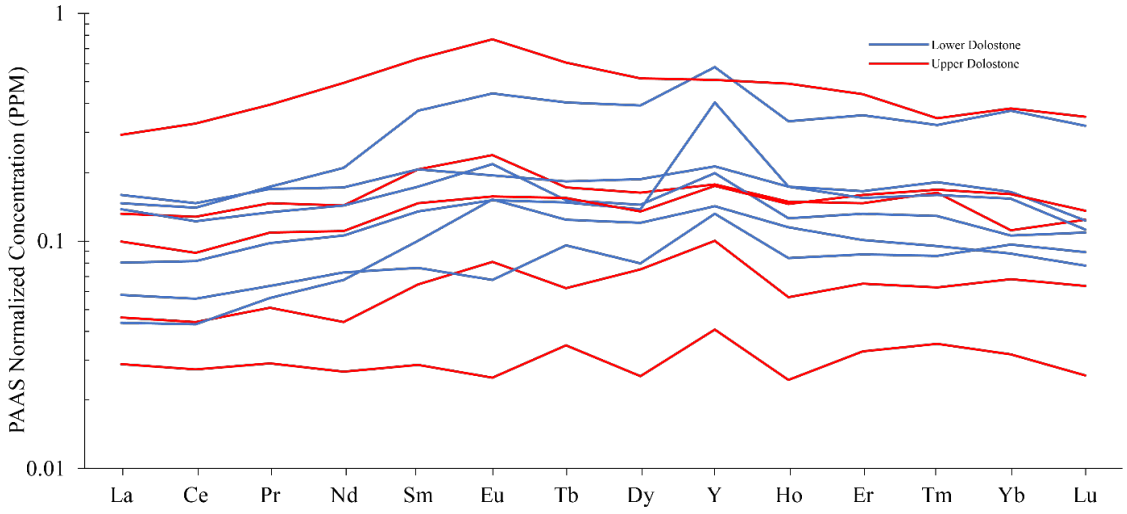

Figure 4.6: REE + Y patterns for Union Island Group lower dolostone and upper dolostone samples.

Black shales, red and green mudstones, and gray shales

Trace metal relationships for determining sedimentary provenance

The average continental crust concentrations of trace metals are taken from Rudnick and Gao, (2013). Concentrations of trace metals have been corrected for carbonate dilution. Carbonate content was calculated as loss on acidification (LOA).

Provenance proxy ratios can be found in **Table 4**. Th/Sc ratios for black shale and gray shale samples were below crustal ratios and averaged 0.62 and 0.56 respectively. In contrast, red and green mudstone samples record enriched Th/Sc ratios with respect to continental crust, averaging 0.94.

La/Sc ratios for black shale samples were depleted compared to crustal concentrations, averaging 2.37. Red and green mudstone samples record a crustal La/Sc ratio of 2.73. The one gray shale sample records an enriched La/Sc ratio of 6.21.

Cross-plots of Th/Sc versus La/Sc (cf. Condie, 1993; **Figure 4.7**) suggest derivation of Union Island Group black shale samples from a predominately mafic source. Red and green mudstone samples indicate sediments sourced from a more felsic provenance. The one gray shale sample indicates derivation from a felsic source composition.

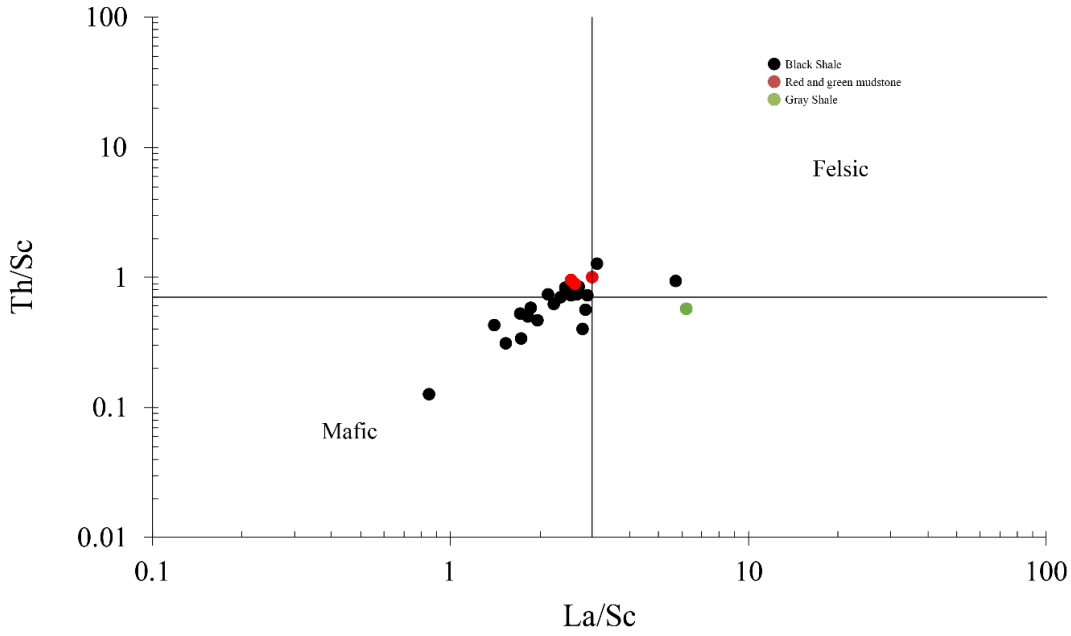

Figure 4.7: Th/Sc versus La/Sc ratios for black shale, red and green mudstone, and gray shale samples (cf. Condie, 1993). Enrichments in incompatible elements (Th and La) versus compatible elements (Sc) reflects contribution of sediments derived from weathering of felsic and mafic sources respectively (Condie, 1993; McLennan et al., 1993).

The Th/Cr ratio in average continental crust is 0.11. Th/Cr ratios in Union Island Group black shale and gray shale samples are depleted with respect to crustal values, both recording average Th/Cr ratios of 0.08. In contrast, red and green mudstone samples are enriched with respect to average continental crust, recording an average Th/Cr ratio of 0.15.

Average continental crust contains a La/Cr ratio of 0.42. La/Cr ratios in the black shale, red and green mudstone, and gray shale samples are enriched above crustal level, with average Th/Cr ratios of 0.75, 0.54, and 1.25 respectively. Cross-plots of Th/Cr versus La/Cr (cf. Bhatia and Crook, 1986, **Figure 4.8**) suggest the Union Island Group

sediments for the black shale, red and green mudstone, and gray shale are sourced from a felsic provenance.

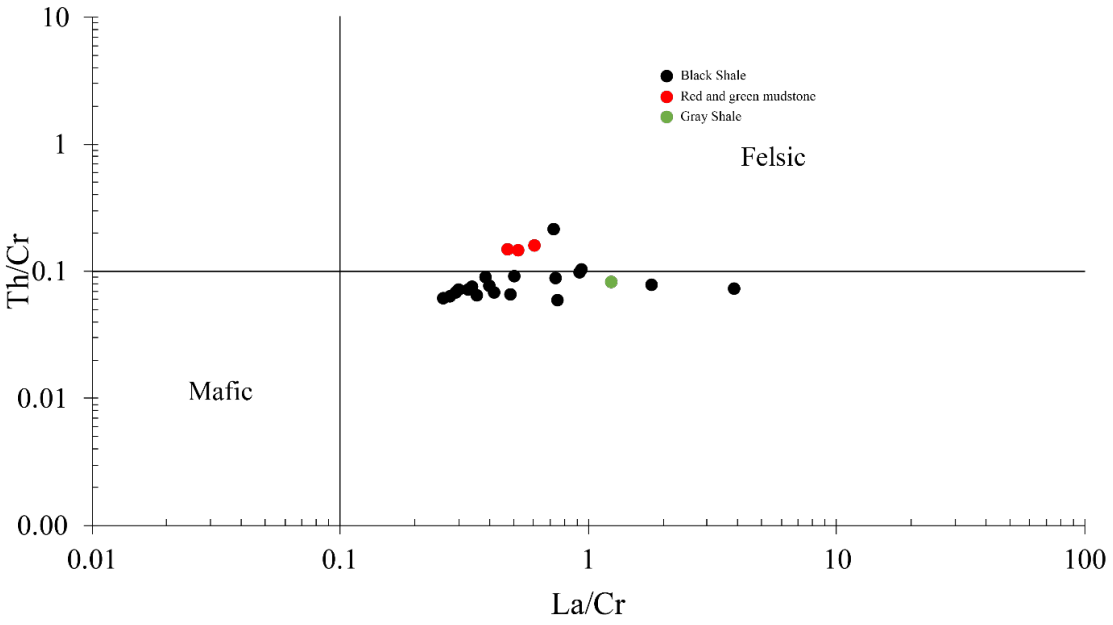

Figure 4.8: Cross-plot of Th/Cr versus La/Cr (cf. Bhatia and Crook, 1986). Enrichments in incompatible elements (Th and La) versus compatible elements (Cr) reflects contribution of sediments derived from weathering of felsic and mafic sources respectively.

Average continental crust contains a Zr/Sc ratio of 13.8. Zr/Sc ratios in black shale, red and green mudstone, and gray shale samples are all depleted with respect to average continental crust. Black shale and red and green mudstone samples both record average Zr/Sc ratios of 9.8. The Zr/Sc of the gray shale was more depleted with respect to average continental crust and was 8.1.

Cross-plots of Th/Sc versus Zr/Sc ratios (cf. McLennan et al. 1993, **Figure 4.9**) indicate that black shale, red and green mudstone, and gray shale samples are reflective

of compositional variation rather than zircon addition and have not been significantly affected by weathering and recycling of sediments. One outlying black shale sample (UN2-15) appears to have been enriched in zircon and contains the highest Zr concentrations at 406.7 ppm. The next highest Zr content in a black shale sample (UN-16-30) was 204.6 ppm.

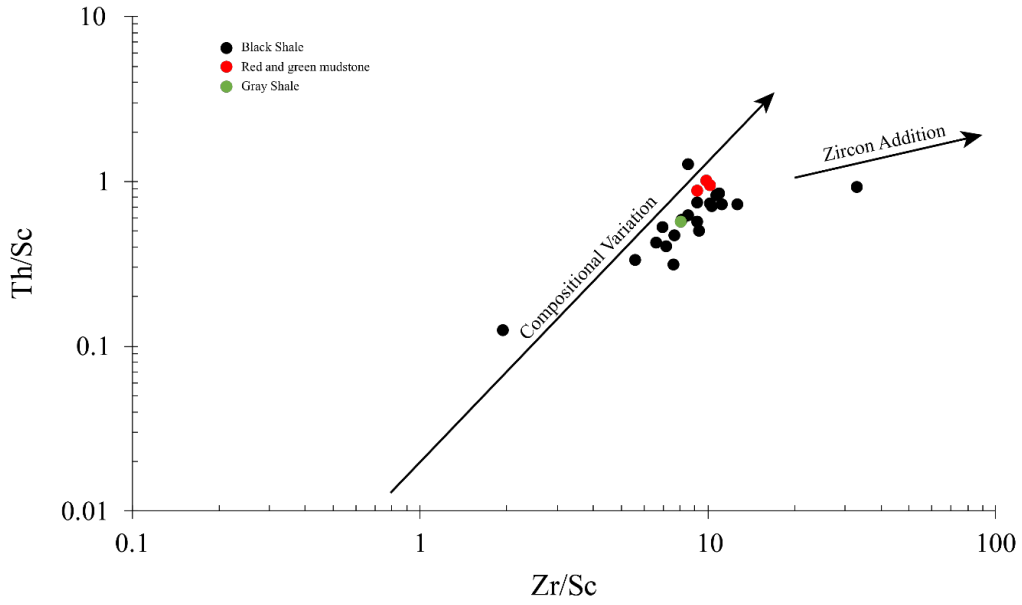

Figure 4.9: Cross-plot of Th/Sc versus Zr/Sc (cf. McLennan et al. 1993). Sedimentary sorting and recycling can lead to enrichments in heavy minerals, notably zircon above crustal concentrations (McLennan et al., 1993).

Trace metal data

The molybdenum (Mo) content of the black shale unit of the Union Island Group is predominately above 1.5 ppm level of the average continental crust, with concentrations ranging from 0.1 to 19.5 ppm, and the average concentration of 7 ppm

(**Table 7**). The red and green mudstone samples are Mo-depleted compared to the average continental crust, ranging from below detection limit to 0.4 ppm. The gray shale is also depleted in Mo compared to the average continental crust and has a Mo concentration of 0.1 ppm.

The uranium (U) content of the Union Island Group black shale unit is higher than the average continental crust concentration of 2.7 ppm (Rudnick and Gao, 2013), with values ranging between 2.0 and 14.1 ppm, and an average value of 6.6 ppm. Red and green mudstone samples are enriched in U compared to the average continental crust and have concentrations slightly lower than those of the black shale unit, between 4.2 and 4.5 ppm, with an average value of 4.3 ppm. Unlike the black shales and red and green mudstones, the only one gray shale sample analyzed is depleted in U compared to the average upper continental crust, with the concentration of 2.5 ppm.

The Union Island Group black shales are generally depleted in Th compared to the 10.5 ppm concentration in the average upper continental crust. Th concentrations range from 2.8 to 26.6 ppm, with an average concentration of 8.7 ppm. Samples from the red and green mudstone are enriched in Th compared to the average upper continental crust, with values ranging between 18.2 and 19.4 ppm, and an average of 18.9 ppm. The one gray shale sample analyzed is enriched in Th compared to the average upper continental crust, having a concentration of 13.2 ppm.

Jones and Manning, (1994) used U/Th ratios <0.75, between 0.75 and 1.25, and >1.25 as representative of deposition under oxic, dysoxic, and suboxic to anoxic waters,

respectively. The average U/Th ratio for the black shale unit is 0.86 (**Figure 4.10, Table 7**) suggesting deposition under low-oxygen conditions (cf. Jones and Manning, 1994). In contrast, two outlying samples of the black shale show U/Th ratios of 0.24 and 0.20, suggesting deposition under a fully oxic water-column (cf. Jones and Manning, 1994). U/Th ratios for the overlying red and green mudstone unit are lower compared to the black shale unit, at an average U/Th ratio of 0.23, consistent with deposition under fully oxic conditions (cf. Jones and Manning, 1994). The gray shale sample has a U/Th ratio similar to those measured for the red and green mudstone, with a U/Th ratio of 0.19, also consistent with deposition under a fully oxic water column.

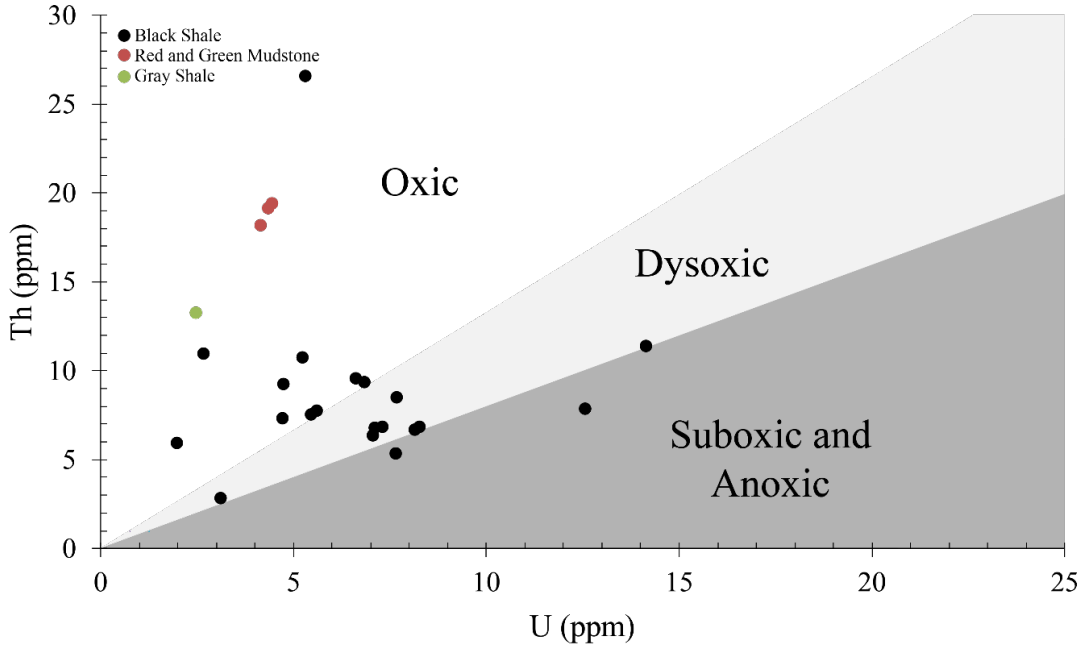

Figure 4.10: U/Th ratios for the Union Island Group black shales, red and green mudstones, and gray shale. U/Th ratios <0.75, between 0.75 and 1.25, and >1.25 reflect deposition under oxic, dysoxic, and suboxic to anoxic waters, respectively (Jones and Manning, 1994). Black shale, red and green mudstone, and gray shale averages are 0.86, 0.23, and 0.19, respectively.

Authigenic enrichment in U (U_{auth}) was calculated as $U_{auth} = U_{total}$-Th/3 (Wignall and Myers, 1988). Black shale samples show authigenic enrichment in U, with U_{auth} ranging between -3.5 and 10.4, with an average of 3.7. Neither the red and green mudstones, or the gray shale record authigenic enrichment with U_{auth} averaging -2.0 and -1.9 respectively.

Iron Speciation

Iron speciation was conducted on black shale, red and green mudstone, and gray shale samples of the Union Island Group to constrain redox conditions during deposition. The ratios of Fe_{HR}/Fe_T and Fe_{py}/Fe_{HR} were calculated following the method of Poulton and Canfield, (2005). The Fe_{HR} pool is quantified as: [$Fe_{HR} = Fe_{carb} + Fe_{ox} + Fe_{mag} + Fe_{py}$]. Black shale samples record the highest Fe_{HR}/Fe_T with values ranging between 0.08 and 1.01and an average of 0.61. Red and green mudstone samples record lower values, with Fe_{HR}/Fe_T ratios ranging between 0.06 and 0.12 and an average of 0.10. The gray shale sample had a Fe_{HR}/Fe_T ratio of 0.54. Black shale samples record the highest ratios of Fe_{py}/Fe_{HR} ranging between 2.21 and 0.02 and averaging 0.42. Red and green mudstones do not contain significant pyrite. The gray shale sample had a Fe_{py}/Fe_{HR} ratio of 0.03. Plots of Fe_{HR}/Fe_T vs Fe_{py}/Fe_{HR} (**Figure 4.11**) suggest deposition of the Union Island Group black shale and gray shale under anoxic ferruginous conditions.

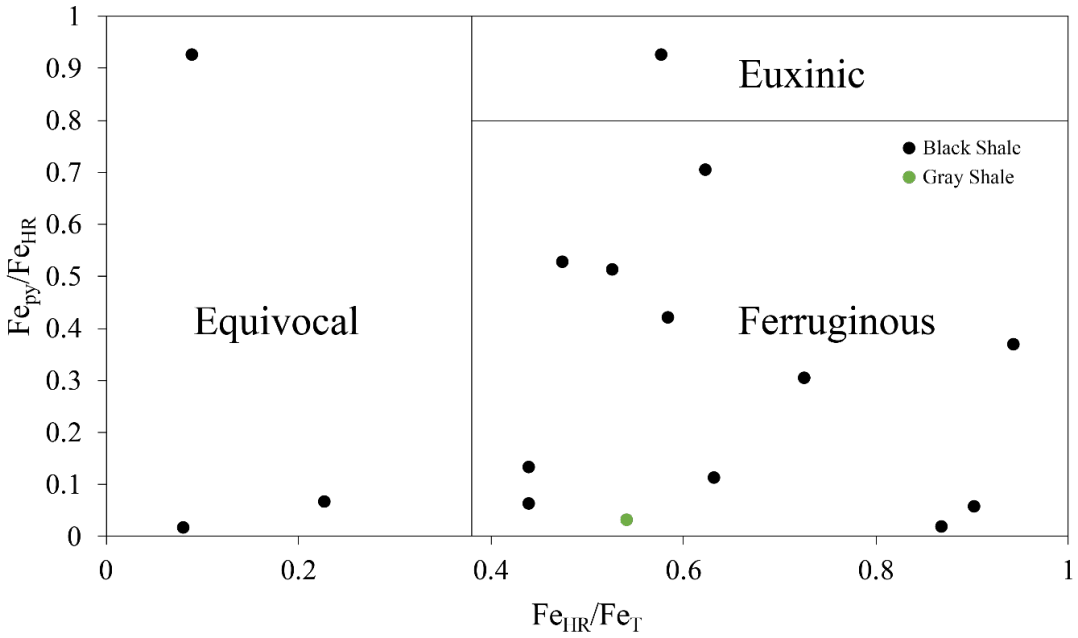

Figure 4.11: Fe_{HR}/Fe_T vs Fe_{py}/Fe_{HR} for Union Island Group black shales and gray shale (cf. Li et al., 2010). Black shales (black) and gray shale (green) suggest deposition under ferruginous conditions. Fe_{HR}/Fe_T >0.38 (black vertical line) in most ancient and modern sediments indicates deposition under anoxic bottom-waters (Li et al., 2010). Fe_{py}/Fe_{HR} ratios >0.8 (black horizontal line) are reflective of deposition under euxinic conditions (Raiswell and Berner, 1987).

Rare-earth elements in the Union Island Group shales

REE + Y concentrations have been normalized to PAAS (Taylor and McLennan, 1985) and REE + Y trends for the Union Island Group black shales, red and green mudstones, and gray shale samples are shown on **Figure 4.12**. The black shale unit of the Union Island Group displays REE + Y patterns with a negative Ce_{SN} anomaly (Ce/Ce^*_{SN} = 0.80) and positive Eu_{SN} anomaly (Eu/Eu^*_{SN} = 1.14). Black shale samples show no LREE to HREE enrichment based on the ratio of Pr/Yb_{SN} (cf., Bau and Dulski, 1996; Pr/Yb_{SN} = 0.97), and are slightly enriched in MREE as reflected by the Sm/Yb_{SN} ratio (cf.

Bolhar and Van Kranendonk, 2007; Sm/Yb_{SN} = 1.05). Red and green mudstone samples display relatively flat REE + Y patterns, but with a slightly negative Ce_{SN} anomaly (Ce/Ce^*_{SN} = 0.96) and LREE enrichment (Pr/Yb_{SN} = 1.22). The gray shale sample has a negative Ce_{SN} anomaly (Ce/Ce^*_{SN} = 0.88) and positive Eu_{SN} anomaly (Eu/Eu^*_{SN} = 1.19). LREE enrichment to HREE is seen as displayed by the ratio of Pr/Yb_{SN} (Pr/Yb_{SN} = 3.33), and MREE enrichment based on Sm/Yb_{SN} (Sm/Yb_{SN} = 1.05).

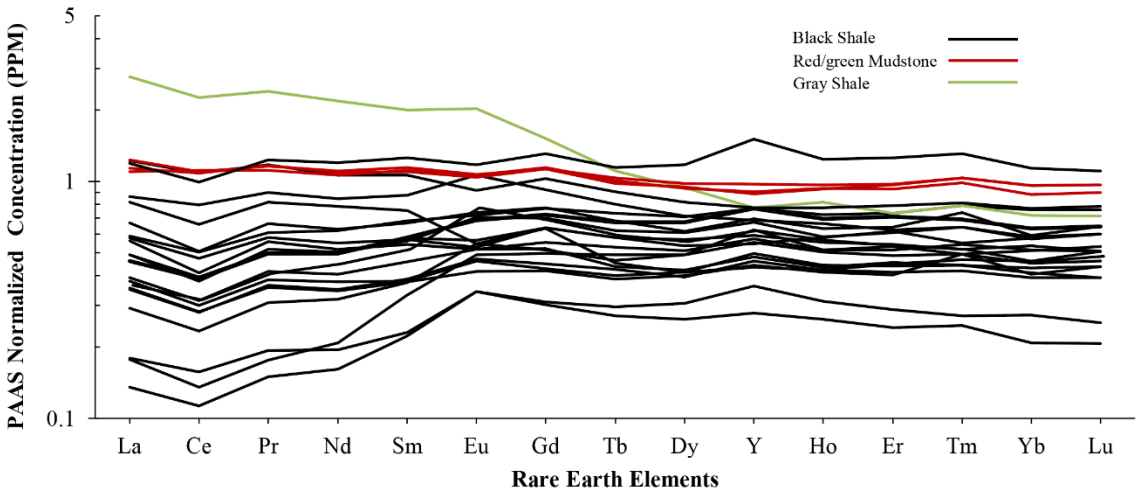

Figure 4.12: REE + Y trends of the Union Island Group black shale, red and green mudstone, and gray shale samples.

Y/Ho ratios

Y/Ho ratios range between 27.5 and 33.5 for black shales, with an average Y/Ho ratio of 30.3, which is higher than the chondritic value of 26 (Bolhar et al., 2004). In contrast, red and green mudstone Y/Ho ratios are closer to chondritic and crustal values,

with ratios ranging between 26.3 and 27.7, and averaging 26.9. The gray shale sample has a near-chondritic Y/Ho ratio of 26.2.

Cerium anomaly

Ce_{SN} anomalies for black shale, red and green mudstone, and gray shale samples from the Union Island Group were calculated using the same formula as the carbonates (see above). All black shale samples with the exception of one (UN-16-26) record a true negative Ce_{SN} anomaly (**Figure 4.13, Table 6**). UN-16-26 falls in the field that represents neither a positive La_{SN} anomaly nor Ce_{SN} anomaly. Two out of the three red and green mudstone samples fall inside of the field that represents a true negative Ce_{SN}, while the third sample (UN-16-38) falls within the field that records neither a positive La_{SN} anomaly nor a negative Ce_{SN} anomaly. The one gray shale sample analyzed falls within the field that records a true negative Ce_{SN} anomaly.

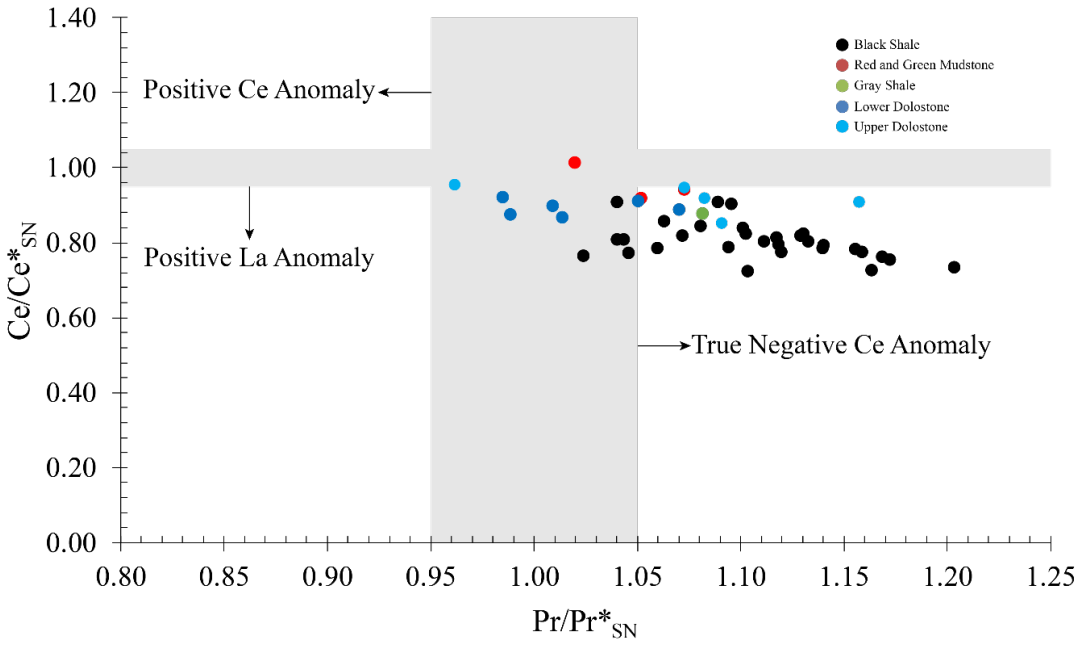

Figure 4.13: Ce/Ce^*_{SN} values [$Ce_{SN}/(0.5*La_{SN} + 0.5*Pr_{SN})$] plotted against Pr/Pr^*_{SN} values [$Pr_{SN}/(0.5*Ce_{SN} + Nd_{SN})$] to check for possible anomalous abundances of La as originally proposed by Bau and Dulski, (1996). The shaded region defines area with no true Ce_{SN} anomaly.

Europium anomaly

Eu_{SN} anomalies for black shale, red and green mudstone, and gray shale samples of the Union Island Group were calculated following the same process as the carbonates (see above). Positive Eu_{SN} anomalies were observed in black shales, with the total Eu/Eu^*_{SN} range from 0.84 to 1.43, and an average value of 1.14 (**Figure 4.12, Table 6**). Red and green mudstone samples display Eu/Eu^*_{SN} values near unity, with values ranging between 0.97 and 0.99, with the average value of 0.98. The gray shale sample also displays a positive Eu anomaly similar to the average value for the black shale samples, with an Eu/Eu^*_{SN} of 1.19.

Nitrogen content and $\delta^{15}N$ values

Total nitrogen (TN) content and nitrogen isotope ratios were measured on decarbonated powders for twenty-six black shale, three red and green mudstone, and one gray shale samples (**Figure 4.14, Table 3**). Black shale samples had the highest TN content, with values ranging between 0.01 and 0.13 wt %, and an average of 0.06 wt %. Both red and green mudstone and gray shale samples had the average nitrogen contents of 0.01 wt %. Black shale samples record positive $\delta^{15}N$ values ranging between +2.9 and +6.9 ‰ and had an average $\delta^{15}N$ value of +5.0 ‰. Red and green mudstone samples had $\delta^{15}N$ values ranging between +1.6 and +1.7 ‰, and the gray shale sample had a $\delta^{15}N$ value of +4 ‰.

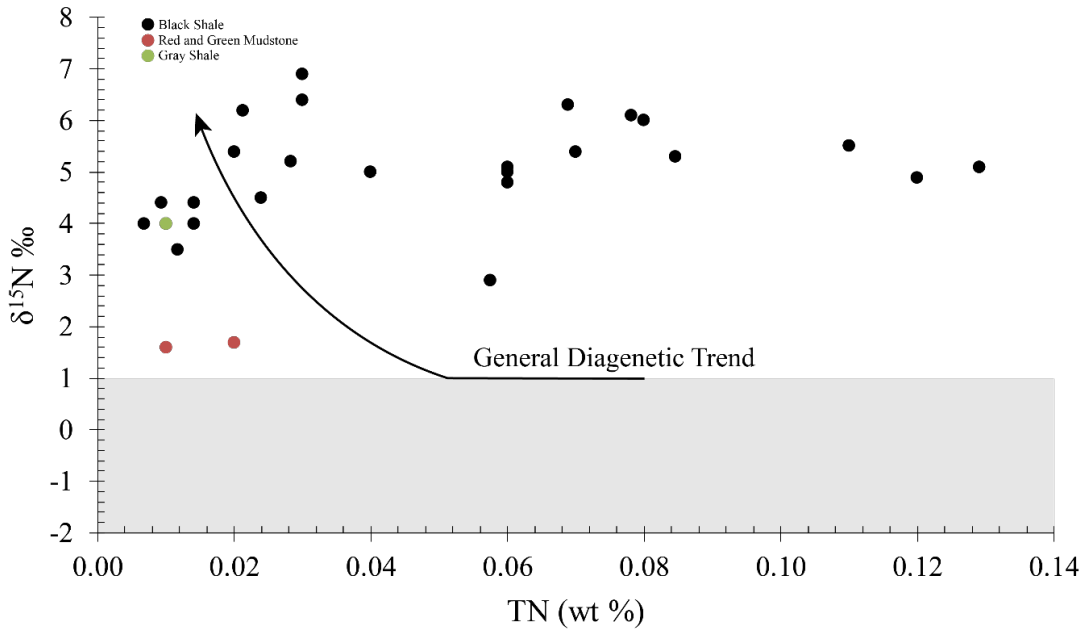

Figure 4.14: TN content (wt %) versus $\delta^{15}N$ values for black shale, red and green mudstone, and gray shale samples of the Union Island Group. Samples display invariably positive $\delta^{15}N$ values with decreasing TN content indicating good preservation of the primary $\delta^{15}N$ signal inconsistent with a trend reflecting post-depositional alteration (black line; cf. Stüeken et al., 2017). The shaded region represents the -2 to +1 ‰ field of nitrogen fixation (cf. Stüeken et al., 2017).

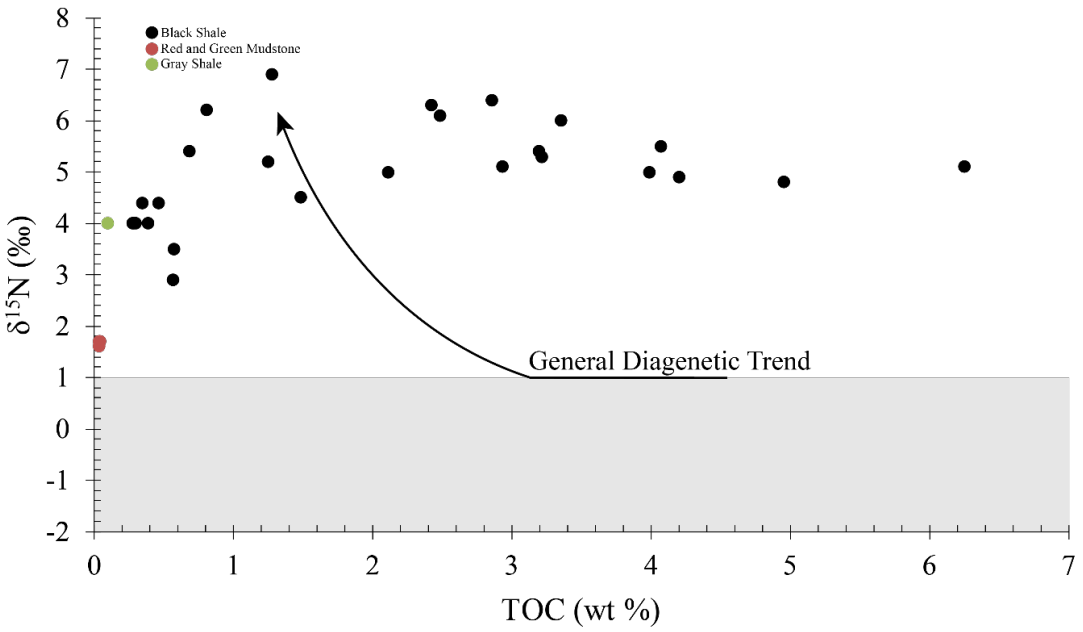

Figure 4.15: $\delta^{15}N$ values versus TOC for black shale, red and green mudstone, and gray shale samples of the Union Island Group (cf. Stüeken et al., 2015b). Lack of correlation between decreasing TOC and increasing $\delta^{15}N$ for black shale ($R^2 = 0.15$), red and green mudstone ($R^2 = 0.25$), and gray samples suggests Union Island Group has not been significantly altered and could preserve a primary signal.

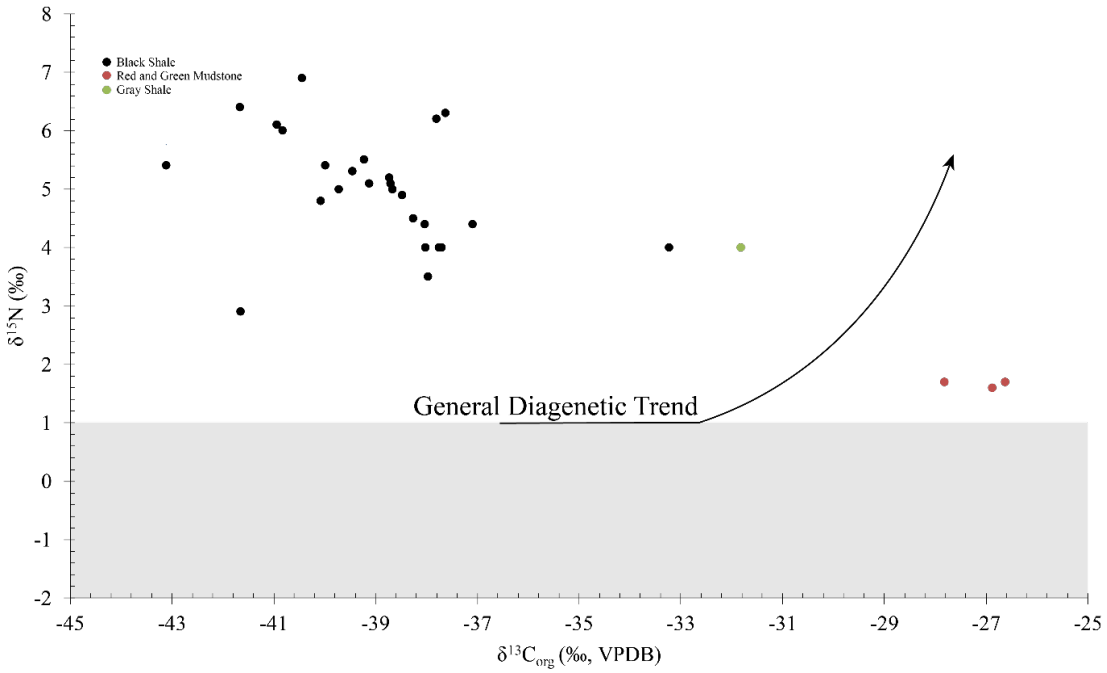

Figure 4.16: $\delta^{13}C_{org}$ versus $\delta^{15}N$ values for the black shale, red and green mudstone, and gray shale of the Union Island Group. Lack of a negative correlation between $\delta^{13}C_{org}$ and $\delta^{15}N$ for black shale ($R^2 = 0.13$), and red and green mudstone ($R^2 = 0.09$) samples indicates good preservation of a primary $\delta^{13}C_{org}$ and $\delta^{15}N$ signal, inconsistent with post-depositional alteration (black line cf. Stüeken et al., 2017). The shaded region represents the -2 to +1 ‰ field of nitrogen fixation (cf. Stüeken et al., 2017).

Carbon to nitrogen ratios

Carbon to nitrogen ratios (C/N) were calculated for decarbonated powders of the Union Island Group black shale, red and green mudstone, and gray shale (**Figure 4.17**). Black shale samples recorded the highest C/N ratios, ranging between 9.9 and 95.4 and averaging 44.8. Red and green mudstone samples contained lower C/N ratios, ranging between 1.8 and 3.6 and had an average value of 2.5. A gray shale sample recorded a C/N ratio of 9.8.

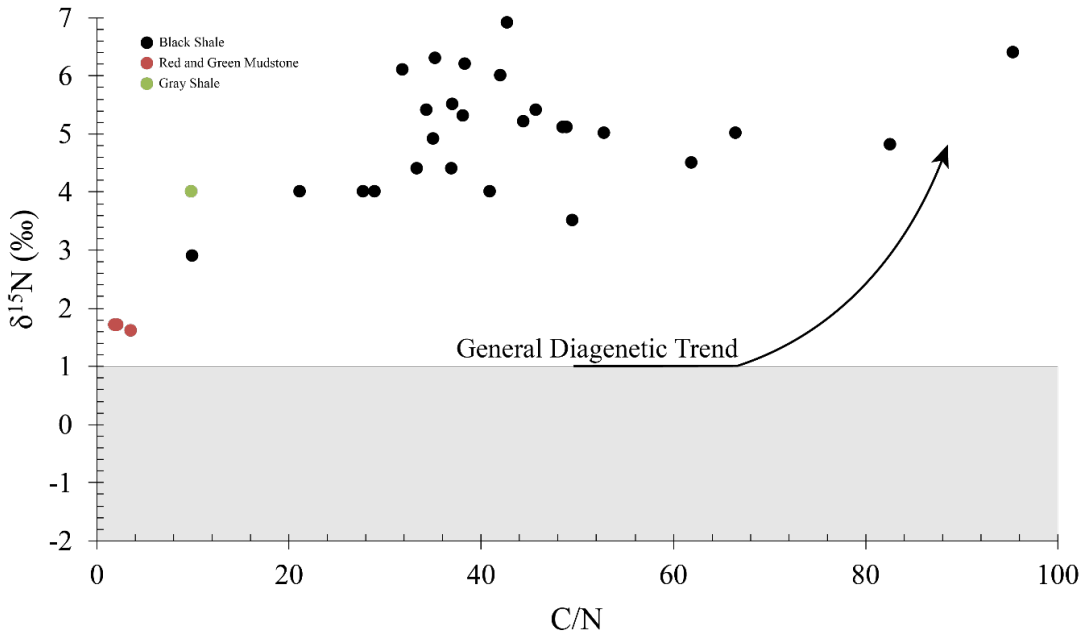

Figure 4.17: $\delta^{15}N$ vs C/N ratios in black shale, red and green mudstone, and gray shale samples for the Union Island Group. Lack of correlation between $\delta^{15}N$ and C/N ratios for black shales ($R^2 = 0.11$), suggests that $\delta^{15}N$ and C/N ratios have not been highly altered by post-depositional alteration. Red and green mudstones show a significant trend ($R^2 = 0.97$), but it is inconsistent with the diagenetic pattern (black line). The shaded region represents the -2 to +1 ‰ field of nitrogen fixation (cf. Stüeken et al., 2017).

Diagenesis

The Union Island Group has been subjected to lower greenschist facies metamorphism (Thorstad, 1976; Sheen et al., 2018). Trends on the $\delta^{13}C_{carb}$ vs. $\delta^{18}O_{carb}$ plot towards lighter values for both $\delta^{13}C_{carb}$ and $\delta^{18}O_{carb}$ is consistent with diagenetic alteration due to fluid-rock interaction (cf. Banner and Hanson, 1990, O'Neil, 1987). Both the data for the lower and upper dolostone units display covariation trending towards lighter values (**Figure 4.1**). The weak correlation between $\delta^{13}C_{carb}$ and $\delta^{18}O_{carb}$ values is stronger for the upper dolostone unit ($R^2 = 0.32$) compared to the lower dolostone unit ($R^2 = 0.15$). Although there are many geologic processes that can affect the original carbon isotope composition of carbonates, they have all been shown to shift carbon isotope composition to lower values (Baumgartner and Valley, 2001; Bekker et al., 2016; Valley, 1986). There is no post-depositional process known to drive carbon isotope values in carbonates to higher values (Baumgartner and Valley, 2001; Bekker et al., 2016; Valley, 1986).

Carbonates for the lower and upper dolostone units were also analyzed for major and trace element trends to further evaluate if the Union Island Group has been subjected to extensive post-depositional alteration during diagenesis and metamorphism. Cross-plots of $\delta^{13}C_{carb}$ and $\delta^{18}O_{carb}$ were plotted with $\delta^{13}C_{carb}$ vs 100[Fe/(Ca + Mg)], $\delta^{13}C_{carb}$ vs

Mn/Sr, and $\delta^{13}C_{carb}$ vs 1000[Mn/(Ca + Mg)] (**Figure 4.4**, Banner & Hanson 1990; Kaufman & Knoll 1995; Niemann & Read, 1988). Interaction of carbonates with fluids during diagenesis has been shown to correlate to an increase in concentrations of Mn and Fe (Barnaby & Rimstidt 1989; Niemann & Read, 1988), and an increase in the Mn/Sr ratio (Banner and Hanson, 1990). Neither the lower or upper dolostones show trends towards lighter carbon isotopes with increasing concentrations of Fe or Mn, or higher Mn/Sr ratios. For these reasons, the highly positive carbon isotope values for the lower dolostone unit are robust and considered as representative of basinal waters in the East Arm during deposition.

Nitrogen cycling insights from stable nitrogen isotope ratios

Nitrogen is a principal limiting nutrient on autotrophic CO_2 fixation. Understanding the biogeochemical nitrogen cycle in deep geologic time has become an area of great interest, due to the redox-sensitive behavior of nitrogen, and sparsity of data from the Paleoproterozoic. Positive $\delta^{15}N$ values (about +2 ‰ to +5 ‰) found in Neoarchean shales provide the earliest evidence that biological nitrification and denitrification had evolved by and had been operational since ca. 2.7 Ga, and there were at least local or transient oxygenation events prior to the onset of the GOE (Kipp et al., 2018; Stüeken et al., 2016; Zerkle et al., 2017).

Analyzing Precambrian sedimentary rocks for nitrogen isotopes requires careful examination to ensure that the signal is reflective of a primary signal rather than the result of secondary alteration. Rocks deposited as far back as the Paleoproterozoic have often been affected during early diagenesis and metamorphic alteration. Sedimentary organic nitrogen has undergone microbial respiration and fermentation through heterotrophic metabolisms during early diagenesis, and thermal maturation of organic matter during burial diagenesis and metamorphism (Thomazo and Papineau, 2013). Heterotrophic degradation of organic matter is known to only impart a small nitrogen isotope fractionation (<1 ‰), whereas other reactions that occur during early diagenesis in oxic or anoxic settings can impart nitrogen isotope fractionation on the order of 2-3 ‰ (Thomazo and Papineau, 2013). The net isotope effect on nitrogen resulting from metamorphism is typically on the order of +1-2 ‰ up to greenschist facies (Thomazo et al., 2011). The Union Island Group has been subjected to lower greenschist facies metamorphism (Hoffman et al., 1977; Kipp et al., 2018; Sheen et al., 2018), and thus, the $\delta^{15}N$ values are likely to have been slightly affected due to loss of nitrogen relative to carbon, and preferential loss of ^{14}N with respect to ^{15}N (Bebout and Fogel, 1992; Kipp et al., 2018). Post-depositional alteration by hydrothermal fluids has been shown to cause a negative correlation between $\delta^{15}N$ and $\delta^{13}C_{org}$ (Schimmelmann and Lis, 2010; Stüeken and Buick, 2018). A plot of $\delta^{15}N$ vs $\delta^{13}C_{org}$ (**Figure 4.16**) shows that there

is a general lack of covariation between $\delta^{15}N$ and $\delta^{13}C_{org}$ for black shale, red and green mudstone, and gray shale samples suggesting the Union Island Group samples have not been strongly affected by hydrothermal fluids during diagenesis and metamorphism (Schimmelmann and Lis, 2010; Schimmelmann et al., 2009). This is further supported by a general lack of covariation between $\delta^{15}N$ and TOC towards heavier $\delta^{15}N$ values with decreasing organic carbon content (Kipp et al., 2018, **Figure 4.15**). $\delta^{15}N$ values for black shale samples are positive and average +5.0 ‰ for both high and low TOC samples. Further $\delta^{15}N$ values do not show covariation with TN for the whole dataset (Haendel et al., 1986; Stüeken and Buick, 2018, **Figure 4.14**). Preferential loss of ^{14}N with respect to ^{15}N during burial diagenesis and metamorphism would manifest itself in a trend where $\delta^{15}N$ values would increase with decreasing TN (Haendel et al., 1986). As organic-bound nitrogen preferentially releases ^{14}N, the remaining organic-bound nitrogen would become enriched in ^{15}N, resulting in more positive $\delta^{15}N$ values (Haendel et al., 1986). Red and green mudstone samples also do not show expected diagenetic trends for $\delta^{15}N$ and $\delta^{13}C_{org}$, $\delta^{15}N$ and TOC, and $\delta^{15}N$ and TN. Lack of evidence for substantial alteration of nitrogen isotope values supports that the Union Island Group records a primary nitrogen signal representative of the organic matter from which it was derived.

There are many metabolic pathways through which nitrogen is utilized, such as fixation, nitrification, denitrification, anaerobic ammonium oxidation (anammox, Mulder et al., 1995; Van de Graafet al., 1995), dissimilatory nitrate reduction to ammonium (DNRA, Sørensen, 1978), and ammonia (NH_3) volatilization (Stüeken et al., 2015c; Talbot and Johannessen, 1992). Differences in $\delta^{15}N$ values between metabolic pathways are reflective of ambient redox state, but with limitations on resolution for specific pathways. For example, isotope fractionations imparted by anammox (Mulder et al., 1995; Van de Graafet al., 1995) are similar to those of canonical denitrifiers making difficult to distinguish between the two metabolic pathways in the geologic record (Brunner et al., 2013; Stüeken et al., 2016). In addition, the extent to which DNRA (Sørensen, 1978) played a role in the Precambrian remains an unanswered question due to current lack of criteria to confidently distinguish between DNRA and denitrification in the deep geologic time (Stüeken et al., 2016). The impact of specific pathways on the global $\delta^{15}N$ signal is also of significance as minor nitrogen pathways such as anammox, DNRA, and NH_3 volatilization pose the potential to be recorded in sediments but could be restricted to distinct environments or certain time periods (Stüeken et al., 2016). Ammonia volatilization (Stüeken et al., 2015c; Talbot and Johannessen, 1992) for example, occurs under highly alkaline waters and has been recorded in modern and ancient alkaline lakes. It could be important to deciphering the nitrogen isotope record in

the deep time as it imposes a large fractionation on the order of ~45 ‰ and can leave residual heavy NH_4^+ that gets incorporated and preserved in biomass (Stüeken et al., 2015c; Stüeken et al., 2016; Talbot and Johannessen, 1992). Positive $\delta^{15}N$ values resulting from NH_3 volatilization between +8.6 and +50.4 ‰ (Thomazo et al., 2011) recorded in alkaline lacustrine sediments of the 2.72 Ga (Arndt et al., 1991) Tumbiana Formation, Pilbara craton, Western Australia are inconsistent with the +5.0 ‰ average $\delta^{15}N$ values of the Union Island Group. Based on the disparity between the $\delta^{15}N$ values of the Tumbiana Formation and the Union Island Group, it is unlikely that the Union Island Group was deposited in a soda lake or setting undergoing extensive NH_3 volatilization.

Consistently positive $\delta^{15}N$ values across the Paleoproterozoic is cited as strong evidence for the expansion of oxygenated surface waters and growth of the bioavailable NO_3^- reservoir (Kipp et al., 2018). Modelling of nitrogen isotope composition of organic matter by Kipp et al., 2018 show that oxygen concentrations required to have accumulation of a bioavailable nitrate reservoir occur at as low as >4.5 μM O_2, well below levels in the well-oxygenated modern ocean. Cross-basinal trends in $\delta^{15}N$ recorded in late Paleoproterozoic and Mesoproterozoic sediments suggest that nitrate availability was abundant in near-shore environments but became depleted in off-shore deepwater settings (Godfrey et al., 2013; Stüeken et al., 2016). Deposition of the 1.88–1.85 Ga

Gunflint and Biwabik Iron Formations of North America on the outer shelf under ferruginous conditions record positive $\delta^{15}N$ values from +2 to +9 ‰ (Godfrey et al., 2013). The overlying near-shore 1.85–1.83 Ga Rove and Virginia Formations deposited at mid-depth under euxinic conditions records positive $\delta^{15}N$ values from +5 to +9 ‰ and are on average +1.5 ‰ heavier than the deeper water ferruginous facies (Godfrey et al., 2013; Stüeken et al., 2016). The ~1.4 Ga Belt Supergroup (Sears et al., 1998) also shows a gradient in $\delta^{15}N$, with positive $\delta^{15}N$ values (~+5 ‰) consistent with aerobic nitrogen cycling recorded in marginal setting facies and $\delta^{15}N$ values consistent with nitrogen fixation (~0 ‰) in the deeper part of the basin (Koehler et al., 2017; Stüeken et al., 2013). In the correlative Roper (~1.4-1.5 Ga, Jackson et al., 1999) and Bangemall (~1.5 Ga, Wingate, 2002) Groups a similar cross-basinal trend is found with nearshore facies recording positive $\delta^{15}N$ values (+7.5 ‰) and slightly negative $\delta^{15}N$ values (-1 ‰) in offshore facies (Koehler et al., 2017). Aerobic nitrogen cycling in most modern marine settings produces $\delta^{15}N$ values between +4 ‰ and +6 ‰ (Tesdal et al., 2013), resulting from rapid nitrification, non-quantitative denitrification in suboxic part of the water column, and quantitative assimilation of residual heavy NO_3^- in the photic zone (Kipp et al., 2018). The positive $\delta^{15}N$ values recorded in the Union Island Group black shale, red and green mudstone, and gray shale are most consistent with nitrification, and are

believed to reflective of aerobic nitrogen cycling in the shallow waters of the East Arm basin at 2045.8 ± 1 Ma.

Section 5.2: Marine versus Lacustrine Setting

Tectonic setting

The East Arm basin is located on the southeastern margin of the Slave craton and is bordered to the south by the Paleoproterozoic (<1986 Ma) Taltson magmatic zone, hosting mylonites of the ca. 1.97-1.92 Ga Great Slave Lake shear zone (Kjarsgaard et al., 2013), and to the east by the Paleoproterozoic (ca. 2.0-1.9 Ga) Thelon tectonic zone along the boundary between the Archean Slave and Rae cratons (Sheen et al., 2018). The northeast-southwest trending, dextral 1.86 Ga McDonald Fault (Bowring et al., 1984; Hoffman et al., 1977) with 70-125 km of displacement partially separates the Great Slave Lake shear zone from the East Arm basin. Strata in the basin in general gently dip towards the Slave craton but become tightly folded in synclinal structures with closer proximity to the Great Slave Lake shear zone (Hoffman et al., 1977; Thorstad, 1976). The strata of the Union Island Group have previously been thought to be deposited in a stagnant basin as basinal marine to platformal shallow-marine sedimentary rocks with intervening mafic volcanics and intrusive rocks (Hoffman et al., 1977; Thorstad, 1976).

Strata of the ca. 1.93 Wilson Island Group are allochthonous to the East Arm (Hoffman et al., 1977; Johnson, 1990; Kjarsgaard et al., 2013), and their position in the stratigraphy of the East Arm basin has remained uncertain until recently. Structural isolation of the Wilson Island Group has further complicated this when attempting to reconstruct basal stratigraphy in the past, due to lack of visible contacts with the Union Island Group (Sheen, 2017). The 2045.8 ± 1.0 Ma age for the Union Island Group (Sheen et al., 2018) has provided the first high-precision geochronological constraints, but the

origin of the Wilson Island Group in relation to the Paleoproterozoic supracrustal successions in the East Arm remains open. Traditionally, the origin of the Wilson Island Group is believed to have stemmed from collision between the Slave and Rae cratons at 1.99-1.91 Ga (Bowring et al., 1984; Kjarsgaard et al., 2013), followed by thrusting of the Wilson Island Group and the Great Slave Supergroup to the northwest to form the East Arm fold-and-thrust belt (Hoffman, 1968, 1988; Hoffman et al., 1977; Kjarsgaard et al., 2013). There is growing evidence however that the collision between the Slave and Rae cratons occurred in a Tian-Shan style intracratonic underthrusting during the Archean (Chacko et al., 2000). In the model proposed by Chacko et al,. (2000), the Taltson magmatic zone and Thelon orogen are not the result of collision between the Slave and Rae cratons, but rather formed in a plate-interior setting distal to where active subduction was taking place, analogous to active mountain belts in central Asia. If this model is correct, the collision between the Slave and Rae cratons precedes the Wilson Island Group and would make the current model invalid.

Plume-induced rifting of the Slave craton is thought to be associated with breakup of the Neoarchean supercontinent Sclavia and is constrained between ~2.2 and 2.0 Ga (Bleeker, 2003; Hoffman et al., 2011; Sheen et al., 2018). Preservation of voluminous mafic volcanism and associated feeder dike systems along rift margins after continental breakup and ocean basin formation has been linked to periods of supercontinent breakup (Courtillot et al., 1999; Morgan, 1971; Sheen et al., 2018). Rifting in the East Arm basin has been constrained to begin at ~2.05 Ga with the emplacement of Union Island dikes (Sheen et al., 2018). Deposition of the lower dolostone unit and subsequent deposition of

the black shale during subsidence of the Slave craton suggests that the Slave craton was undergoing passive rifting rather than active (Sheen et al., 2018).

The 1.93 Ga Wilson Island Group has been interpreted as a rift succession (Bowring et al., 1984) within the East Arm basin. Detrital zircon data for sandstones of the Wilson Island Group display a prominent peak at 2.0-1.9 Ga, which has been linked to provenance from the nearby Taltson magmatic zone and the Thelon tectonic zone (Sheen et al., 2018; Van Breeman et al., 2013). The absence of this signature in the Union Island Group (Sheen et al., 2018), further supports that deposition of the Wilson Island Group occurred during a later stage in rifting and development of the East Arm basin at the time when active magmatism took place in the surrounding Taltson magmatic zone and Thelon tectonic zone.

Sedimentary Provenance

Weathering of felsic and mafic igneous rocks produces variations trace elements that are incorporated into shales and can be utilized in determining sedimentary provenance. Incompatible elements are generally enriched in felsic rocks compared to mafic rocks. Higher concentrations of incompatible elements such as La and Th (enriched in felsic rocks) and compatible elements such as Sc and Cr (enriched in mafic rocks) has been used as a proxy in determining the contribution of felsic and mafic components to sedimentary provenance (Condie, 1993; Cullers et al., 1988, 2000; Cullers, 1994; Floyd and Leveridge, 1987; McLennan and Hemming, 1992; McLennan et al., 1993; Taylor and

McLennan, 1985; Wronkiewicz and Condie, 1987,1990). Cross-plots of Th/Sc versus La/Sc (cf. Condie, 1993; McLennan and Taylor, 1991; McLennan and Hemming, 1992; Taylor and McLennan, 1985) show a majority of the black shale samples fall within the quadrant indicating a higher contribution of mafic material (**Figure 4.7**). This conflicts with Sm-Nd data (see below) which suggests the sediments derived from weathering of the granitic Slave craton to be the source of the provenance. Red and green mudstone samples plot in close to the boundary separating felsic and mafic source composition, and do not definitively show a majority contribution from either source. Sm-Nd isotope data (see below) for the red and green mudstone samples is inconsistent with this, as they record more positive ε_{Nd} values, and produce younger Sm-Nd model ages (see Figure #). The gray shale sample displays a higher La/Sc ratio than all of the other samples, but a low Th/Sc ratio plotting just below the quadrant representing a felsic provenance and is thus likely derived from weathering of a felsic source.

Black shale, red and green mudstone, and gray shale samples are enriched in Sc compared to crustal concentrations (Rudnick and Gao, 2013). Enrichment in Sc in shales above crustal concentrations has been suggested to be hosted in residual clays during weathering (Condie, 1993; Cullers, 1988). It is possible that the La/Sc and Th/Sc ratios for Union Island Group samples could diluted by excess Sc hosted in clay minerals from weathering.

Th/Cr and La/Cr ratios are a second proxy that has been invoked to resolve sedimentary provenance (Bhatia and Crook, 1986; Cullers and Podkovyrov, 2000). The

incompatibility of Th and La in the melt phase produces felsic igneous rocks bearing Th and La enrichments. Cr is generally compatible in igneous melts and enriched with respect to Th and La in rocks of mafic composition (Cullers, 1994). Due the source specific enrichment of Th, La, and Cr, analyzing the ratios of Th/Cr versus La/Cr is a method of determining a felsic or mafic source composition of sediments to the provenance. The Union Island Group black shale, red and green mudstone, and gray shale samples all plot along the boundary for felsic composition (**Figure 4.8**), with La/Cr ratios well above those of a mafic provenance. Cr has been shown to have an affinity to be incorporated into shales during weathering rather than upper continental crust and adsorbed into clay minerals (Condie and Wronkiewicz, 1990; Wronkiewicz and Condie, 1987; Wronkiewicz, 1989). Black shale, red and green mudstone, and gray shale samples are enriched in Cr compared to continental crust. Increased concentrations of Cr sourced from weathering of the provenance could lower the ratios of Th/Cr and La/Cr below a felsic source provenance. Interestingly, red and green mudstone samples plot within a felsic provenance conflicting with Sm-Nd data (see below). Due to the vulnerability of Th/Cr and La/Cr ratios to weathering and sedimentation, the use of the ratios may not monitor sediment provenance (Condie and Wronkiewicz, 1990) and should be interpreted with caution.

A final provenance proxy that was utilized was Th/Sc versus Zr/Sc (McLennan et al., 1993). The ratio of Zr/Sc is a useful provenance parameter due to the differing geochemical behavior of Zr with respect to Sc. Zr is enriched in heavy minerals such as zircon, while Sc is generally representative of the provenance similar to REE (McLennan,

1989a; McLennan et al., 1993). Recycling of sediments and aeolian transport of zircon grains has been shown to be a source of enrichments of Zr (Brimhall et al., 1991; Taylor et al., 1983) rather than reflecting compositional variation of the provenance. The Th/Sc ratio is used to assess igneous chemical differentiation of the provenance based on the incompatibility of Th in igneous systems with respect to the Sc (McLennan et al., 1993). Plotting the ratio of Th/Sc versus Zr/Sc discriminates between compositional variation in the provenance and zircon addition from recycling of sediments (**Figure 4.9**, cf. McLennan et al., 1993). All of the Union Island Group samples, with the exception of one outlying black shale sample (UN2-15) plotted close to the line denoting compositional variation to sediment in the provenance, suggesting that sediments of the Union Island Group preserve the source composition of sediment to the provenance and have not been extensively recycled.

Samarium/Neodymium systematics

The black shale unit of the Union Island Group records predominantly negative ε_{Nd}, ranging between -7.6 and 0. Depletion of samarium (Sm) relative to neodymiun (Nd) in continental crust results in $^{143}Nd/^{144}Nd_{sample}$ ratios below that of Chondritic Uniform Reservoir (CHUR) and generally negative ε_{Nd} values (DePaolo and Wasserburg, 1976). Sm-Nd model ages (TDM) generated for the black shale unit are consistently Archean in age, ranging from 2.8 to 3.1 Ga, and suggest the provenance dominated by weathering of the 2622-2581 Ma Archean granitic basement of the Slave craton (Kjarsgaard et al.,

2013b). In contrast, red and green mudstone samples display a spread of ε_{Nd} values, ranging between -1.6 and +3.2, consistent with a change in the provenance to the dominance of the juvenile material. TDM model ages generated for the red and green mudstone are between 2.2 and 2.6 Ga, indicating significant contribution from the Union Island volcanics.

Sr Isotope Values for the Union Island Group carbonates

The $^{87}Sr/^{86}Sr$ isotope ratios in carbonates has been extensively used to constrain seawater secular trend from the Archean through the modern time. The two main sources of Sr to the oceans are submarine weathering of oceanic crust providing unradiogenic Sr with low $^{87}Sr/^{86}Sr$ ratios (~0.703) and subaerial weathering of continental crust and its overlying sediments delivering radiogenic Sr with $^{87}Sr/^{86}Sr$ ratios as high as ~0.712 (Veizer, 1989). A compilation of $^{87}Sr/^{86}Sr$ isotope ratios through time by Shields and Veizer, (2002) shows that the ratio of $^{87}Sr/^{86}Sr$ has steadily increased from the Archean through the Paleozoic (Kuznetsov et al., 2010). A caveat in using $^{87}Sr/^{86}Sr$ isotope ratios to constrain the isotope composition of seawater is that the preservation of a primary seawater Sr signal in carbonates decreases further back in geologic time. Major difficulties with trying to obtain a primary seawater Sr isotope signal back during the Paleoproterozoic are: 1.) a limited number of carbonate formations, 2.) a higher potential for post-depositional alteration of ancient carbonates, 3.) a higher level of uncertainties regarding depositional reconstructions, and 4.) a limited number of reliable and precise

geologic constraints (Kuznetsov et al., 2010). This has contributed to sparsity of data for this time period and large error bars for ages. Current best estimates for the $^{87}Sr/^{86}Sr$ of seawater at the beginning of the Paleoproterozoic is between 0.70314 and 0.70339, with $^{87}Sr/^{86}Sr$ values increasing by ca. 2.32 Ga to between 0.70433 and 0.70452 (Bekker et al., 2003b; Frauenstein et al., 2009; Kuznetsov et al., 2010). A decrease in $^{87}Sr/^{86}Sr$ ratios during the period of 2.1-2.0 Ga has been attributed to an increase in hydrothermal flux at mid-ocean ridges related to the breakup of the Kenorand supercontinent (Bekker et al., 2003a; Daly et al., 2006; Kuznetsov et al., 2010; Pesonen et al., 2003; Wanke and Melezhik, 2005).

Highly radiogenic $^{87}Sr/^{86}Sr$ ratios have been described from the Lomagundi-aged rift-related lacustrine carbonates of the 2.22 Ga Kuetsjärvi Sedimentary Formation (KSF) in NW Russia (Melezhik et al., 2005a). Carbonates of this formation display highly positive $\delta^{13}C_{carb}$ values ranging between +5.8 and +8.9 ‰, and $^{87}Sr/^{86}Sr$ ratios from 0.70406 to 0.70623 (Melezhik et al., 2005a). High $^{87}Sr/^{86}Sr$ ratios (0.70560-0.70623) recorded in the lower and middle dolostone members of the Kuetsjärvi Sedimentary Formation were considered to reflect the original composition of non-marine basinal waters, while a decrease in $^{87}Sr/^{86}Sr$ ratios towards the top of the section was interpreted to represent a short-term marine invasion (Melezhik et al., 2005a).

Strontium concentrations of carbonates from both the lower and upper dolostone units are generally higher in the lower dolostone unit. Lower dolostone Sr concentrations average at 70.8 ppm and range from 22.22 to 150.5 ppm, whereas the upper dolostone

concentrations average at 32.3 ppm and range from 19.1 to 68.3 ppm. Post-depositional alteration has been shown to result in higher $^{87}Sr/^{86}Sr$ ratios and low Sr concentrations (Banner and Hanson, 1990; Kuznetsov et al., 2010; Shields and Veizer, 2002). A cross-plot of $^{87}Sr/^{86}Sr$ vs. Sr content (**Figure 4.3**) shows a lack of correlation between $^{87}Sr/^{86}Sr$ ratio and Sr content for the lower ($R^2 = 0.01$) and upper ($R^2 \approx 0$) dolostones, arguing for preservation of the primary Sr isotope signal. Alteration of carbonates during post-depositional processes has also been shown to result in a positive correlation between $^{87}Sr/^{86}Sr$ ratios and Mn/Sr ratios, as Sr is preferentially lost through interaction with fluids (Banner and Hanson, 1990). A cross-plot of $^{87}Sr/^{86}Sr$ ratios vs. Mn/Sr (**Figure 4.5**) ratios in the lower ($R^2 = 0.05$) and upper ($R^2 = 0.03$) dolostones do not display the expected positive correlation and further supports that the Sr isotope signal of the Union Island Group has not been significantly affected by post-depositional processes.

Samples from both the lower and upper dolostone units that underwent Sr analysis show presence of quartz, feldspar, and an absence of clays in the insoluble residue. Terrigenous input of feldspar could contribute ^{87}Rb to the sediments, which decays to ^{87}Sr, thereby increasing the $^{87}Sr/^{86}Sr$ ratio (Shields and Veizer, 2002).

Continental crust $^{87}Sr/^{86}Sr$ ratios are similar to the $^{87}Sr/^{86}Sr$ values for the lower and upper dolostone unit carbonates. ε_{Nd} values for the black shale unit are predominately negative (-7.6 to 0), indicating the granitic Slave craton provenance. Using the lowest $^{87}Sr/^{86}Sr$ ratios as an upper bound for the $^{87}Sr/^{86}Sr$ ratio of the basinal waters (cf., Kuznetsov et al., 2010; Shields and Veizer, 2002), the $^{87}Sr/^{86}Sr$ ratios of the Union Island

Group carbonates are too high to reflect of a marine signal and suggest a strong degree of basin isolation. Slight addition of marine waters into the non-marine realm would result in a marine $^{87}Sr/^{86}Sr$ ratio due to the orders of magnitude higher concentrations of Sr in marine versus non-marine waters (Veizer et al., 1992a; Veizer and Compston, 1974). The lowest $^{87}Sr/^{86}Sr$ values for the lower and upper dolostone units are 0.7084 and 0.7095 respectively, strongly suggesting that the Union Island Group carbonates do not preserve a primary seawater Sr isotope signal, thus supporting a plausible restricted depositional setting.

REE Systematics of the Union Island Group Shales

Rare earth elements (REE) and yttrium (Y) (REE + Y) are supplied to the oceans through aeolian input, continental runoff, and hydrothermal vents, and are removed via particle scavenging (Bau and Dulski, 1999; Byrne and Kim, 1990; Douville et al., 1999; Elderfield et al., 1990). Yttrium is often included alongside the fourteen REE due to its geochemical similarity to Ho (both are trivalent with nearly identical ionic radii; Bohlar et al., 2004) but is scavenged by particulate matter at half the rate of other REE (Planavsky et al., 2010). Y/Ho ratios for PAAS and chondrites are 27.5 and 26, respectively, with variability representing higher or lower abundance of Y relative to neighboring heavy rare earth elements (HREE) (Bohlar et al., 2004).

The Y/Ho ratio has been a valuable redox proxy due to the redox-sensitive behavior of Ho relative to Y under suboxic to anoxic conditions. Under oxic conditions,

more particle-reactive Ho would be scavenged onto the surface of Mn-Fe oxyhydroxides precipitating out of solution, and organic matter particles (Masuzawa and Koyama, 1989; Piper, 1974b; Planavsky et al., 2010; Sholkovitz et al., 1994), resulting in higher Y/Ho ratios in seawater, and positive Y_{SN} anomalies (Bau et al., 1997b; Nozaki et al., 1997; cf. Planavsky et al., 2010). In the redox-stratified aquatic environments which were prominent during much of the Proterozoic, Mn-Fe oxyhydroxides precipitated out of oxic shallow-waters, across the redoxcline into suboxic or anoxic waters, where they were reduced back into solution (Bau and Dulski, 1996; Planavsky et al., 2010). High Y/Ho ratios, as seen in modern marine waters (40-80 in open-marine settings; Bau et al., 1997b; Tostevin et al., 2016) are a strong signature of a fully oxygenated water column where Ho is scavenged by organic matter and reactive particles (Bau and Dulski, 1996). Y/Ho>36 are often used as a support for the preservation of a primary marine signal (Tostevin et al., 2016).

The Y/Ho ratios for the Union Island Group black shale unit have the highest value at 30.3, followed by that for the red and green mudstone at 26.9, and for the gray shale at 26.2. While the Y/Ho ratio for the black shale unit is higher than that for PAAS and chondrites, it is well below the threshold of >36 that is generally associated with a primary seawater signal. A decrease in the Y/Ho ratio for the red and green mudstone and gray shale samples to chondritic values is indicative of a higher contribution of siliciclastic material derived from weathering of the Slave craton with respect to basinal water signal. Red and green mudstone samples also record a small true negative Ce_{SN} anomaly on plots of Ce/Ce^*_{SN} versus Pr/Pr^*_{SN} (**Figure 4.13**), which typically suggests

oxic conditions. Alternatively, dissolution of Mn-Fe oxyhydroxides in the deep suboxic to anoxic parts of the basin have been shown to record small negative and sometimes positive Ce_{SN} anomalies (Bau et al., 1997b). Reactive particle surfaces can shuttle the adsorbed Ce into the suboxic to anoxic parts of the basin and upon dissolution across the redoxcline reintroduce heavy Ce into deeper water generating a small negative, to positive Ce anomaly (Bau et al., 1997b; Masuzawa and Koyama, 1989; Sholkovitz et al., 1994). This process could plausibly explain the decrease in the Y/Ho ratio to near chondritic and PAAS values, while also accounting for the small negative Ce_{SN} anomaly recorded in the red and green mudstone samples.

Light rare-Earth element to heavy rare-Earth element ratios

All REE are trivalent, with the exception of Ce, which under highly oxidizing conditions can be oxidized to Ce^{4+}, and Eu, which under reducing conditions is stable as Eu^{2+} (MacRae et al., 1992). In the modern ocean, preferential incorporation of heavy rare-earth elements (HREE) into carbonate ions leaves a residual pool of REE enriched in light rare-earth elements (LREE) (Bolhar et al., 2004). Sinking of LREE preferentially sequestered onto particle surfaces depletes seawater with respect to LREE and leaves a higher proportion of HREE behind in solution (Bolhar et al., 2004), ultimately producing seawater that is enriched in HREE compared to LREE. Under anoxic conditions in redox-stratified basins, dissolution of sinking Mn-Fe oxyhydroxides below the redoxcline return LREE to HREE ratios of seawater to values approaching crustal composition (Bau et al., 1997b; Planavsky et al., 2010). Continental crust is enriched with respect to chondrites in

LREE compared to HREE (PAAS Pr/Yb = 3.13), and thus the terrestrial flux carries LREE enrichment (Bau and Dulski, 1999).

The ratio of Pr/Yb_{SN} is typically used to characterize fractionation of LREE vs HREE (Lawrence et al., 2006; Planavsky et al., 2010). Pr is used rather than La to account for the possible La anomaly since no Pr anomaly has been reported (Bau and Dulski, 1996). The Union Island Group black shale unit shows a flat LREE to HREE pattern with an average Pr/Yb_{SN} ratio of 0.98 (**Figure 4.12**) below the Pr/Yb ratio of 3.13 for PAAS. In contrast, red and green mudstone, and gray shale samples display enrichment in LREE with respect to HREE, with the averages of 1.22 and 3.33, respectively. LREE enrichment has been found in terrigenous sediments derived from Archean cratons, suspended load in rivers, and in modern detrital ocean sediments (Goldstein and Jacobsen, 1988). The provenance during deposition of the red and green mudstone shifted to the one dominated by weathering of mafic juvenile volcanics as indicated by slightly negative to positive ε_{Nd} values. A return of Y/Ho ratios to near chondritic (~26) values in the red and green mudstone implies LREE enrichment coming from terrigenous flux. The chondritic (Y/Ho = 26.2) ratio of the gray shale and LREE/HREE (Pr/Yb_{SN} = 3.33) ratio of the gray shale is consistent with a crustal signature.

Europium anomaly

Eu anomaly (Eu/Eu^*_{SN}) [calculated as $Eu_{SN}/(0.67*Sm_{SN} + 0.33*Tb_{SN})$] is the measure of the fractionation of Eu relative to Sm and Tb (Gao and Wedepohl, 1995). There is a number of processes responsible for generating a positive or negative Eu anomaly: 1.) derivation of Eu from rocks of either a mafic or felsic source, 2.) eolian input of clay minerals that host Eu, 3.) precipitation from porewaters enriched in Eu^{2+}, and 4) precipitation of authigenic minerals from waters influenced by hydrothermal fluids (Bau and Dulski, 1999; MacRae et al., 1992; Nath et al., 1997). The predominant host of Eu^{2+} in felsic and mafic igneous rocks is in plagioclase. Granites, for example, are known to display a strong negative Eu anomaly due to plagioclase segregation and Eu^{2+} rich residuum (Gao and Wedepohl, 1995). None of the shale samples display a negative Eu anomaly so this mechanism is considered invalid. Eolian transport of clays (predominantly kaolinite derived from felsic rocks, and smectite derived from mafic rocks), produced from decomposition of plagioclase, can preferentially release Eu^{2+}, resulting in a positive Eu anomaly. XRD analysis of a black shale sample showed that the minerals found in association with the shales were predominately quartz and mica with some dolomite. It is unlikely that these minerals are the major hosts for Eu^{2+} and are not believed to be responsible for the positive Eu anomaly in the black shales. Reducing conditions within the sediments during diagenesis were shown to lead to upward mobilization of Fe^{2+}, Mn^{2+}, and Eu^{2+} (MacRae et al., 1992). Migration of Fe^{2+} into more oxidizing conditions lead to the development of Fe-rich crust, under which there is an enrichment in Eu, producing a positive Eu anomaly (MacRae et al., 1992). Generation of

a positive Eu anomaly through precipitation in porewaters is unlikely to have been responsible for the positive Eu anomaly as there is no evidence for the formation of an Fe-rich crust in association with the black shales. Unlike in case of Ce anomaly, reducing, acidic hydrothermal fluids typically show a distinct positive Eu anomaly in otherwise uniformly light to middle REE enriched patterns when normalized to shale composites (Michard et al., 1983; Bau and Dulski,1999; Wheat et al., 2002). The Union Island black shale unit shows predominantly flat light to heavy REE patterns when normalized to PAAS, with the average Pr/Yb_{SN} ratio of 0.98, but has a slight enrichment in MREE (Sm/Yb_{SN} = 1.05) and displays a positive Eu anomaly (average Eu/Eu^*_{SN} = 1.14) (**Figure 4.12**). Interaction with hydrothermal fluids thus seems the most plausible explanation of the positive Eu anomaly recorded in the black shales. The one gray shale, which also displays a positive Eu anomaly (Eu/Eu^*_{SN} = 1.19) is also thought to be influenced by interaction with reducing hydrothermal fluids, given lack of evidence to support other mechanisms. In contrast, the red and green mudstone samples do not display a positive Eu anomaly with the average Eu/Eu^*_{SN} value of 0.99. Lack of a positive Eu anomaly in the red and green mudstone along with Y/Ho ratios close to PAAS and chondrite, and negative Ce_{SN} anomalies could be further evidence of terrigenous sediment input in the REE + Y patterns (**Figure 4.12**).

Section 5.3: Basin-scale Origin of Highly Positive Carbon Isotope Values

Carbon isotope composition of unaltered, ancient marine carbonates might reflect the seawater composition. The 2045.8 ± 1.0 Ma age of the Union Island Group basalt is younger than the generally accepted terminus of the LE at ca. 2060 Ma and older than the ca. 2031 Ma carbon isotope excursion recorded by the Wooly Dolomite, opening the question of whether the Union Group lower dolomite unit highly positive carbon isotope values are indicative of a global signal or local processes. To evaluate effect of post-depositional alteration on carbonates of the Union Island Group, $\delta^{13}C_{carb}$ vs. $\delta^{18}O_{carb}$ data were plotted (**Figure 4.1**). Data for carbonates of the lower dolostone unit ($R^2 = 0.15$), upper dolostone unit ($R^2 = 0.31$), and black shale unit ($R^2 = 0.29$) only display a weak positive linear relationship, suggesting that C and O isotope compositions were not significantly affected by a diagenetic overprint. Although carbonates of the Union Island Group appear to have been affected to some degree by post-depositional alteration during diagenesis and metamorphism as reflected by their pervasive recrystallization, there is no known post-early diagenetic process to produce high carbon isotope values in carbonates (Baumgartner and Valley, 2001; Bekker et al., 2016; Valley, 1986). For this reason, the highly positive carbon isotope values of the lower dolostone unit are considered to record the highly positive carbon isotope values of basin waters during deposition of this unit. In

contrast, negative carbon isotope values for the carbonate fraction of samples from the black shale unit could indicate their diagenetic origin. The Wilson Island Group dolostones display a stronger positive correlation ($R^2 = 0.62$), indicating that their $\delta^{13}C_{carb}$ values were subjected to a stronger post-depositional alteration.

Carbonates containing highly positive carbon isotope values of local origin have been associated with basins having evaporative conditions, high organic productivity, and methanogenic conditions during early diagenesis (Claypool, 1973; Claypool and Kaplan, 1974; Irwin et al., 1977; Lazar and Erez, 1990; Melezhik et al., 1999; Stiller et al., 1985). In contrast to the highly positive carbon isotope values (~ +7 ‰) of the lower dolostone unit, carbon isotope values for the upper dolostone unit are closer to 0 ‰, consistent with the carbon isotope composition of seawater during most of the Earth's history.

The LE is associated with the first extensive deposition of marine sulfate evaporites, and shortly after 2.0 Ga they become rare again (Bekker and Holland, 2012; Grotzinger and Kasting, 1993; Hodgskiss et al., 2019; Pope and Grotzinger, 2003) until 1.2 Ga or even later at 0.8 Ga when thick, extensive marine sulfate evaporites reappeared in the rock record (Bekker and Holland, 2012; Kah et al., 2001; Turner and Bekker, 2016; Young, 1981). The lower dolostone unit does not show high oxygen isotope values that would be consistent with evaporative conditions. One sample from the lower dolostone

unit, UN-16-34-5m, revealed on petrographic analysis carbonate associated with length-slow chalcedony. Folk and Pittman, (1971) described a length-slow form of chalcedony, with the c-axis parallel to the fibers, almost exclusively found in association with sulfates. Sulfate minerals are often completely replaced by the length-slow chalcedony and can record a former existence of salt-flat, sabkha, or sulfate-rich environments (Folk and Pittman, 1971). Pseudomorphs or lenses and beds of sulfate evaporites are commonly associated with Lomagundi-aged carbonate platforms (Bekker et al., 2006, 2016; Melezhik et al., 2005a, b; Schröder et al., 2008). Although petrographic observations suggest that sulfate-replete conditions might have existed at least locally during deposition of the lower dolostone unit, many Precambrian and more recent sedimentary basins where evaporite settings developed are not characterized by high C isotope values in carbonates. In contrast to the lower dolostone unit, the upper dolostone unit does not display any evidence for evaporite minerals in the field or in samples.

Methanogenesis below the sediment-water interface results in the production of carbon dioxide with highly positive carbon isotope values and methane with highly negative carbon isotope values (Claypool & Kaplan 1974; Friedman & Murata 1979; Irwin et al., 1977; Talbot & Kelts 1986). Carbonates formed near the sediment-water interface in association with methanogenesis typically display highly variable positive

and negative carbon isotope values (over a short vertical and lateral distance), ranging from several per mil to several tens of per mil (Bekker et al., 2016; Friedman and Murata 1979; Hennessy and Knauth 1985; Winter and Knauth 1992a,b). Organic carbon from the lower dolostone unit is highly ^{12}C-enriched, indicating contribution of organic matter produced by methanotrophic microorganisms. $\delta^{13}C_{org}$ values for the lower dolostone unit range from -42.1 to -22.7 ‰, with an average of -31.8 ‰. Three partial sections of the lower dolostone unit were taken across the study area to constrain if the highly positive $\delta^{13}C_{carb}$ values of the lower dolostone unit are reflective of local processes or a basin-scale signal. Organic carbon isotope values for the three partial sections within the lower dolostone unit are highly variable, consistent with a methanotrophic signal (see **Figures 5.3.1-5.3.3**). The three partial sections, UN-16-31, UN-16-34, and UN-16-35, all record highly negative $\delta^{13}C_{org}$ values, reaching as low as -37.9 ‰, -42.1 ‰, and -40.6 ‰, respectively. Variability in $\delta^{13}C_{org}$ within each respective section is 13.8 ‰, 17.1 ‰, and 17.9 ‰. Fractionation between $\delta^{13}C_{carb}$ and $\delta^{13}C_{org}$ ($\Delta^{13}C$) for the lower dolostone unit sections is as high as 50.0 ‰, indicating some contribution of organic matter produced by methanotrophs. Importantly, large variations in $\delta^{13}C_{org}$ values within the lower dolostone unit are not mirrored by the $\delta^{13}C_{carb}$ record, which is highly positive and relatively invariant throughout, suggesting that both primary and secondary productivity

contributed to organic matter in the sediments, but the inorganic carbon pool remained relatively stable on a basin scale.

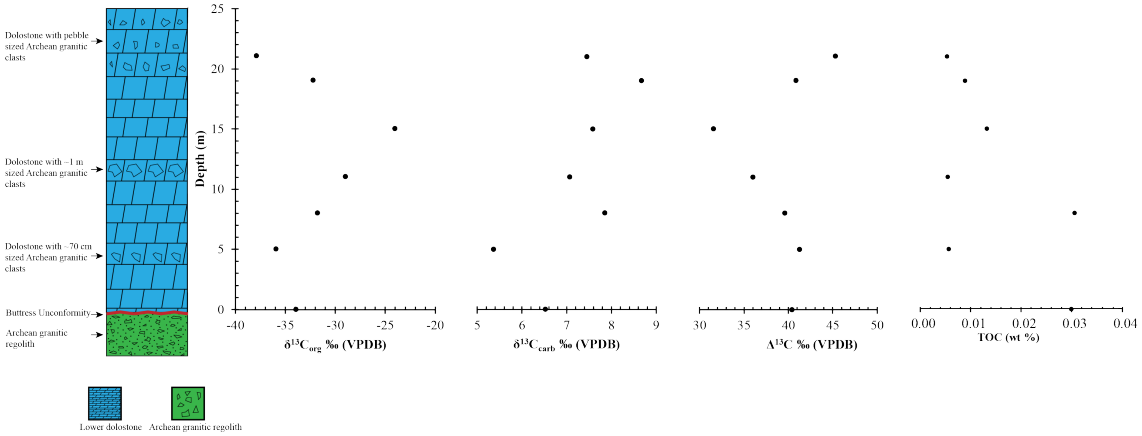

Figure 5.3.1: Partial stratigraphic section of the Union Island Group lower dolostone unit (section UN-16-31). From left to right data are plotted for $\delta^{13}C_{org}$ (‰), $\delta^{13}C_{carb}$ (‰), $\Delta^{13}C_{carb}$ (‰), and TOC (wt %). All isotopes are measured relative to the VPDB scale.

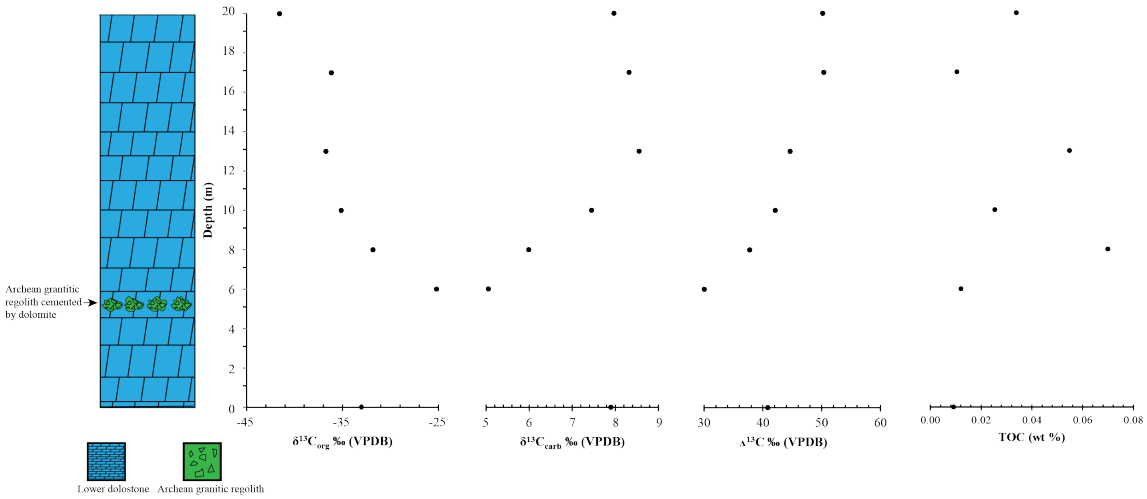

Figure 5.3.2: Partial stratigraphic section of the Union Island Group lower dolostone unit (section UN-16-34). From left to right data are plotted for $\delta^{13}C_{org}$ (‰), $\delta^{13}C_{carb}$ (‰), $\Delta^{13}C_{carb}$ (‰), and TOC (wt %). All isotopes are measured relative to the VPDB scale.

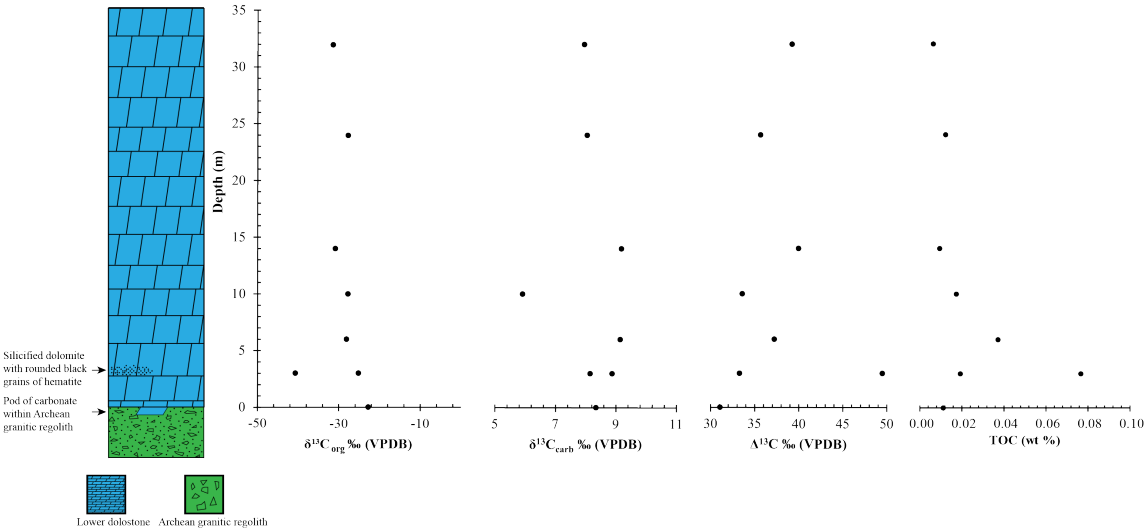

Figure 5.3.3: Partial stratigraphic section of the Union Island Group lower dolostone unit (section UN-16-35). From left to right data are plotted for $\delta^{13}C_{org}$ (‰), $\delta^{13}C_{carb}$ (‰), $\Delta^{13}C_{carb}$ (‰), and TOC (wt %). All isotopes are measured relative to the VPDB scale.

Two partial sections from the upper dolostone unit showed similar trends (see **Figures 5.2.4-5.2.5**). The two sections UN-16-6 and UN-16-27 have highly negative $\delta^{13}C_{org}$ values reaching as low as -36.5 and -37.5 ‰, respectively. Variability in $\delta^{13}C_{org}$ values within each respective section was 14.4 ‰ and 13.2 ‰. $\Delta^{13}C$ values for the upper dolostone unit were not as large as those for the lower dolostone unit, but were still as high as 38.1 ‰, also indicating some contribution from methanotrophic productivity.

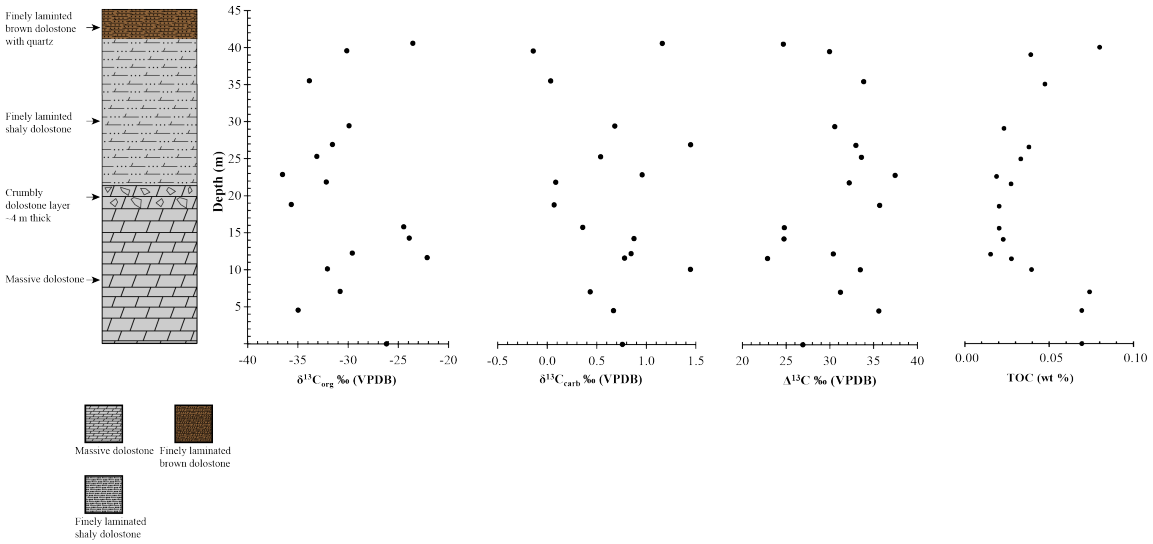

Figure 5.3.4: Partial stratigraphic section of the Union Island Group upper dolostone unit (section UN-16-6). From left to right data are plotted for $\delta^{13}C_{org}$ (‰), $\delta^{13}C_{carb}$ (‰), $\Delta^{13}C_{carb}$ (‰), and TOC (wt %). All isotopes are measured relative to the VPDB scale.

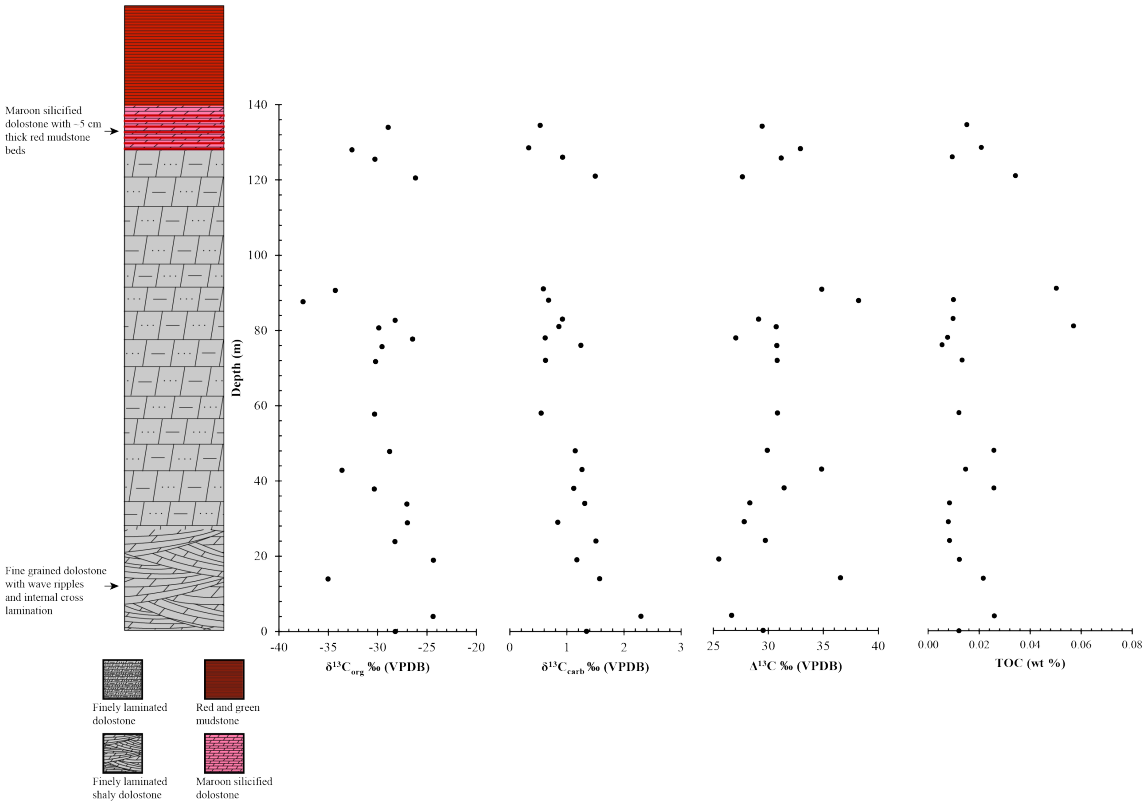

Figure 5.3.5: Partial stratigraphic section of the Union Island Group upper dolostone unit (section UN-16-27). From left to right data are plotted for $\delta^{13}C_{org}$ (‰), $\delta^{13}C_{carb}$ (‰), $\Delta^{13}C_{carb}$ (‰), and TOC (wt %). All isotopes are measured relative to the VPDB scale.

Unlike the highly positive $\delta^{13}C_{carb}$ values recorded in the lower dolostone unit, $\delta^{13}C_{carb}$ values for the upper dolomite unit are stable and near-to-zero, with an average of 0.5 ‰. These values are inconsistent with the highly variable $\delta^{13}C_{carb}$ values that are typical of carbonates associated with methanogenesis near the sediment-water interface. Like for the lower dolostone unit, the variability in $\delta^{13}C_{org}$ values was not seen in the $\delta^{13}C_{carb}$ record, suggesting that while the source of organic carbon was variable on a local scale, the dissolved inorganic carbon pool for the basin remained stable. Although variability in $\delta^{13}C_{org}$ values was slightly lower in the upper dolostone unit than in the

lower dolostone unit, highly fractionated $\Delta^{13}C$ values for both units indicate a contribution of organic matter derived from methanotrophic organisms.

High $\delta^{13}C_{carb}$ values could also be related to high primary productivity, such as that of microbial mats preferentially incorporating ^{12}C into their organic matter (Broecker, 1970; Hayes, 1983). Removal of light carbon results in enrichment in ^{13}C in the residual inorganic carbon pool. Burne and Morre, (1987) found that carbonate precipitating on calcifying microbial mats has highly positive $\delta^{13}C_{carb}$ values on the order of +5 to +10 ‰. However, in contrast to most Paleoproterozoic stromatolite-rich carbonate successions, stromatolites are practically lacking in the Union Island Group carbonates, with the exception of one locality on the northeastern tip of Union Island, where Sheen, (2017) reported them in the lower dolostone unit immediately on the contact with the Archean basement in a shallow-water setting. In addition, the presence of stromatolites by itself does not conclusively identify areas of high productivity. For example, in modern settings stromatolites are commonly found in low productivity, oligotrophic settings (Bekker et al., 2016).

The high TOC content of the Union Island black shale unit, ranging between 0.3 and 6.3 wt %, indicates that there was high organic carbon burial in the deeper-water settings of the East Arm basin. In areas of high primary productivity such as in cyanobacterial mats, nitrate is rapidly consumed, and nitrogen fixation compensates for nitrogen limitation (Quan and Falkowski, 2009; Woebken et al., 2015). If the Union Island Group was deposited in the basin with high primary productivity, the $\delta^{15}N$ and $\delta^{13}C_{org}$ composition of organic matter in the black shale unit would be expected to reflect

values associated with nitrogen fixation and primary producers, respectively (Ader et al., 2016). $\delta^{15}N$ values for the black shale unit are positive for both high and low TOC samples, averaging +5.0 ‰, which is consistent with aerobic nitrogen cycling, while $\delta^{13}C_{org}$ values with the average of -39.4 ‰ indicate contribution of organic matter produced by secondary productivity. The black shale unit samples do not show expected diagenetic trends on scatter plots between $\delta^{15}N$ and TN content **(Figure 4.14)** ($R^2 = 0.09$, Haendel et al., 1986; Stüeken and Buick, 2018), $\delta^{15}N$ and $\delta^{13}C_{org}$ (**Figure 4.16**) ($R^2 = 0.13$, Schimmelmann et al., 2009; Schimmelmann and Lis, 2010), or $\delta^{15}N$ and TOC content (**Figure 4.15) (**$R^2 = 0.15$, Stüeken et al., 2015b), suggesting that $\delta^{15}N$ and $\delta^{13}C_{org}$ values of the black shale unit have not been extensively altered and are reflective of redox conditions and biogeochemical carbon cycling in basinal waters. $\delta^{15}N$ values inconsistent with nitrogen fixation and $\delta^{13}C_{org}$ values reflecting some contribution of secondary production suggests the Union Island Group was not deposited in the basin with sufficiently high primary productivity to induce nitrogen fixation and cyanobacterial blooms.

Highly positive and relatively invariable $\delta^{13}C_{carb}$ values in the lower dolostone unit and near-to-zero $\delta^{13}C_{carb}$ values in the upper dolostone unit reflect a significant change in the $\delta^{13}C$ composition of the dissolved inorganic carbon reservoir in the Union Island basin. Weak covariation of $\delta^{13}C_{carb}$ and $\delta^{18}O_{carb}$ values for the lower dolostone ($R^2 = 0.15$) and upper dolostone ($R^2 = 0.31$) units indicates that the two units were subjected to insufficient alteration during early diagenesis and metamorphism to completely

obliterate the primary signals. Highly negative $\delta^{13}C_{org}$ values recorded in the lower and upper dolostone units are reflective of deposition in an area with high organic carbon burial as also indicated by deposition of organics-rich shales of the black shale unit deeper in the basin. Contribution of organic matter produced by methanotrophy imparted large fractionations in $\Delta^{13}C$, reaching as high as 50.0 ‰ in the lower dolostone unit and 38.1 ‰ in the upper dolostone unit. Relatively invariable, highly positive $\delta^{13}C_{carb}$ values in the lower dolostone unit, and near-to-zero $\delta^{13}C_{carb}$ values for the upper dolostone unit in association with variable and highly negative $\delta^{13}C_{org}$values suggest that $\delta^{13}C_{org}$ values of organic matter reflect a local-scale, biogeochemical carbon processing, while the dissolved inorganic carbon pool does not. Positive $\delta^{15}N$ values recorded in the black shale unit, inconsistent with nitrogen fixation, indicate that the Union Island Group was not deposited in the basin with high primary productivity. For these reasons, it seems most likely that the highly positive $\delta^{13}C_{carb}$ values of the lower dolostone unit and the near-to-zero $\delta^{13}C_{carb}$ values for the upper dolostone unit are representative of conditions developed throughout the East Arm basin, potentially linked to the global biogeochemical cycling of carbon at ca. 2046 Ma ago.

Section 5.4: Distinguishing the Lomagundi Event versus the Aftermath

Irreversibly oxidizing conditions in the atmosphere-ocean system developed with the onset of the GOE between 2.4 and 2.3 Ga (Bekker et al., 2004; Gumsley et al., 2017; Lyons et al., 2014). The disappearance of mass-independent fractionation (MIF) of sulfur isotopes in the sedimentary record between 2.43 and 2.31 Ga is a strong evidence that oxygen concentration in the atmosphere rose above the 10^{-5} PAL threshold required to preserve a MIF-S signal and have remained above that level ever since (Bekker et al., 2004; Farquhar et al., 2000; Gumsley et al., 2017). Even during the "Boring Billion" of the Middle Proterozoic, when oxygen concentration in the atmosphere stabilized at a lower level, it remained well above that in the Archean required to preserve a MIF signal ($>10^{-5}$ PAL) (Farquhar et al., 2000; Lyons et al., 2014). The LE that lasted from ca. 2.22 to 2.06 Ga, marks a period during which estimated 12-22 times the PAL of oxygen was released to surface environments through extensive burial of organic matter, resulting in the so called "oxygen overshoot" (Bekker and Holland, 2012; Karhu and Holland, 1996). Burial of ^{12}C-enriched organic matter produced carbonates with $\delta^{13}C_{carb}$ values averaging +8 ‰, but reaching as high as +28 ‰, that have been identified on all continents with the exception of Antarctica (Bekker, 2014; Bekker et al., 2003; Karhu and Holland, 1996).

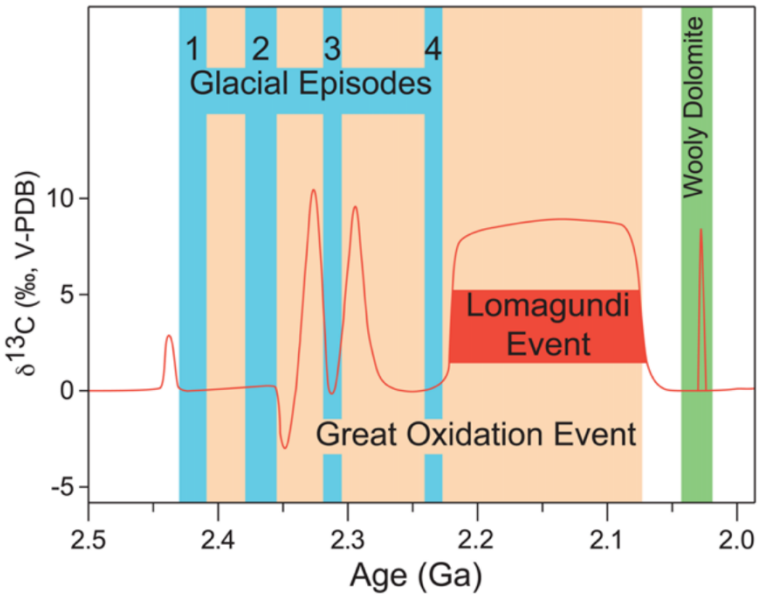

Figure 5.4.1: Secular carbon isotope curve for the early Paleoproterozoic carbonates from Bekker et al., (2016). Note the ca. 160 Ma long highly positive Lomagundi carbon isotope excursion (LE; Karhu and Holland, 1996; red box), and short-lived, but highly positive carbon isotope excursion recorded by the ca. 2.03 Ga Wooly Dolomite (Bekker et al., 2016; green bar) and the potentially correlative ca. 2.02 Ga Gumbi Group (Buick et al., 2003).

Termination of the LE is marked by a return of carbon isotope values in carbonates to around 0 ‰ (Bekker and Holland, 2012; Karhu and Holland, 1996; Maheshwari et al., 2010; Melezhik et al., 1999), in association with deposition of organics-rich lithologies (Martin et al., 2013; Melezhik et al., 1999). A shift from carbonate to organics-rich siliciclastic lithologies has been linked to sea level rise associated with the supercontinent breakup (Aspler and Chiarenzelli, 1998; Bekker, 2014; Bekker et al., 2003; Karhu, 1993). Other changes that accompanied the end of the LE are a crash in the seawater sulfate reservoir (Bekker and Holland, 2012), deposition of Mn-rich sediments (Bekker et al., 2013; Ossa Ossa et al., 2018), the first appearance of phosphorite deposits (Bekker et al., 2003, 2012; Maheshwari et al., 2010; Papineau,

2010), and deposition of iron formation (Bekker et al., 2013; Ossa-Ossa et al., 2018). While the mechanism responsible for the termination of the LE remains open to debate, a decrease in carbon isotopic values in carbonates of the ca. 2113 ± 4 Ma Lower Viistola Formation and ca. 2062 ± 2 Ma Upper Petonen Formation in Finland (Karhu, 1993; Karhu and Holland, 1996) has constrained the termination of the Lomagundi Event between 2113 ± 4 Ma and 2062 ± 2 Ma in Fennoscandia. Intrusion of the Bushveld Complex into the Pretoria Group has similarly constrained the age of the termination of the LE to be older than 2061 ± 1 Ma in South Africa (Scoates and Friedman, 2008).

In the aftermath of the LE, there has conventionally been perceived long-term stability in the carbon cycle up until the NOE between 0.85 and 0.54 Ga (Buick et al., 1995; Holland, 2006; Och and Shields-Zhou, 2012). Growing evidence from the slightly younger than the LE sedimentary successions is challenging this view for the one favoring biogeochemical instability in its immediate aftermath. The most notable evidence comes from the Wooly Dolomite Formation in the upper Wyloo Group in the Horseshoe Rift basin of western Australia (Bekker et al., 2016). The Wooly Dolomite is a ~325 m thick shale-dolostone succession deposited under shallow-water conditions, when the Horseshoe basin was not fully open to an ocean, but was connected to the ocean through a north-trending rift (Bekker et al., 2016). Carbon isotope values from the depositional sequence 3 (Bekker et al., 2016; Krapež et al., 2015) are highly positive, reaching as high as +8.4 ‰ VPDB (Bekker et al., 2016). U-Pb SHRIMP zircon dating by Müller et al. 2005 of the tuff in the depositional sequence 1 obtained an age of 2031 ± 6 Ma, post-dating the termination of the LE by 30 million years. Intriguingly, the granulite

metamorphic facies Gumbi Group of the Limpopo Belt in South Africa has detrital zircons with an age of 2028 ± 7 Ma, and marbles with carbon isotope values as high as +7.0 ‰ VPDB (Buick et al., 2003), confirming that in the aftermath of the LE there was at least one short-lived highly positive carbon isotope excursion. Highly positive carbon isotope values of the Wooly Dolomite and Gumbi Group marbles point to a highly volatile biogeochemical carbon cycle in the aftermath of the LE, in contrast to the perceived long-term stability.

Deposition of carbonates recording the end of the carbon isotope excursion in association with black shales is a characteristic the Union Island Group shares with sedimentary successions deposited at the end of the LE. Two such successions are the ca. 2083 ± 6 Ma Francevillian Series in Gabon (Horie et al., 2005) and the 2090 ± 70 Ma Tulomozero Formation in the Onega basin in Karelia (Ovchinnikova et al., 2007; Martin et al., 2015). The U-Pb zircon age of 2045.8 ± 1.0 Ma for the Union Island Group places it chronostratigraphically between the ca. 2.22-2.06 Ga LE (Karhu and Holland, 1996) and a short-lived highly positive carbon isotope excursion of the ca. 2031 Ma Wooly Dolomite (Bekker et al., 2016). Carbon isotope data for the lower dolostone and upper dolostone units reveal that at ca. 2046 Ma the biogeochemical carbon cycle might have been also volatile, fluctuating between highly positive and near-to-zero values.

Negative $\delta^{13}C_{org}$ values associated with the lower dolostone unit range between -42.1 and -22.7 ‰ and average at -31.1 ‰. Highly positive $\delta^{13}C_{carb}$ values of the lower dolostone unit (**Figures 5.3.1-5.3.3**) indicate that the dissolved inorganic carbon pool in the East Arm basin during that time was heavy. Assuming that the highly positive $\delta^{13}C_{carb}$

values are representative of the dissolved inorganic carbon pool in the East Arm basin during deposition, a carbon isotope fractionation as large as 50.0 ‰ was associated with the production of bulk organic matter in the basin.

Large isotope fractionations between the carbonate and organic carbon, likely due secondary productivity, have been documented in a number of LE-aged basins. In the 2083 ± 6 Ma Francevillian Series of Gabon (Horie et al., 2005), carbonates with highly positive carbon isotope values up to +8.5 ‰ are overlain by organic-rich shales having $\delta^{13}C_{org}$ as low as -46.2 ‰ and associated with deposition under euxinic conditions (Bekker et al., 2008; Gauthier-Lafaye, 2006; Ossa-Ossa et al., 2018). The Sengoma Argillite Formation of Botswana, deposited along the northern margin of the Kaapvaal craton in the Pretoria basin during the LE, shows the fractionation between inorganic and organic carbon pools on the order of 36 ‰, likely reflecting a shallow redoxcline, with methanogenesis in the deep part of the basin, and methanotrophy at the redoxcline (Bekker et al., 2008). A $\Delta^{13}C$ as large as 50.0 ‰ for the Union Island Group strongly indicates influence by secondary productivity, and a contribution of organic matter derived from methanotrophy.

A shift in $\delta^{13}C_{carb}$ values to those of the upper dolostone unit that are close to zero indicates a significant change in the dissolved inorganic carbon pool in the Union Island Group basin to lighter values. In contrast, $\delta^{13}C_{org}$ values for the upper dolostone unit are on the average heavier, ranging between -37.5 ‰ and -22.1 ‰ with the average value of -29.5 ‰. The upper dolostone unit records $\Delta^{13}C$ values as large as 38.1 ‰, consistent with a weaker organic carbon contribution from secondary productivity such as

methanotrophy or sulfide oxidation. Fe-speciation data for the black shale unit (**Figure 4.11**) indicate deposition of the black shale unit under anoxic, ferruginous conditions. The true negative Ce_{SN} anomalies of the lower and upper dolostone units indicate that they were likely deposited under at least mildly oxygenated conditions above a redoxcline consistent with their deposition at shallower water depths compared to those for the black shale unit (**Figure 4.13**).

For all three partial sections of the lower dolostone (UN-16-31, UN-16-34, and UN-16-35) $\delta^{13}C_{carb}$ values are consistently highly positive, while $\delta^{13}C_{org}$ values display much higher spatial variability on the order of tens per mil (**Figure 5.3.1-5.3.3**). Positive covariation between $\delta^{13}C_{carb}$ and $\delta^{13}C_{org}$ is seen in the UN-16-31 section (**Figure 5.3.1**). No covariation between $\delta^{13}C_{carb}$ and $\delta^{13}C_{org}$ values was observed in the other two sections. The consistently positive $\delta^{13}C_{carb}$ values with relatively minor stratigraphic variability, but highly negative $\delta^{13}C_{org}$ values with a much more pronounced stratigraphic variations suggest that the $\delta^{13}C_{org}$ values likely reflect a mixed signal from primary and secondary productivity rather than high amplitude changes in the dissolved inorganic carbon pool. Two partial sections were measured and sampled from the upper dolostone unit (**Figures 5.3.4** and **5.3.5**). For both UN-16-6 and UN-16-27 sections, $\delta^{13}C_{carb}$ and $\delta^{13}C_{org}$ values covary. There is however significantly more scatter in the $\delta^{13}C_{org}$ than $\delta^{13}C_{carb}$ values, as is also seen for the lower dolostone unit, similarly reflecting a mixture of primary and secondary productivity rather than changes to the dissolved inorganic carbon pool.

$\delta^{13}C_{carb}$ values for carbonates from the ca. 1.93 Ga Wilson Island Group are similar with those obtained for the upper dolostone unit, ranging between -2.1 and +1.7

‰, with the average of +0.5 ‰. Despite being allochthonous to the East Arm basin, the near-to-zero values for the Wilson Island Group carbonates suggest that the biogeochemical carbon cycle had stabilized by the time these carbonates were deposited to "normal" conditions typical of the mid-Proterozoic.

Section 5.5: Redox Conditions During Deposition of the Black Shale Unit

Nitrogen

Positive $\delta^{15}N$ values have been recorded in sediments spanning the Earth's history, likely reflecting redox cycling of nitrogen in oceans with spatially heterogeneous NO_3^- availability (Stüeken et al., 2016) (**Figure 5.5.1**). The positive $\delta^{15}N$ values of the Union Island black shale unit (+2.9 to +6.9 ‰) (**Figure 4.14-4.17**) suggest deposition in settings with high enough oxygen concentrations to maintain a bioavailable NO_3^- reservoir with the nitrification- and denitrification-dominated nitrogen isotope signal. Late diagenetic and metamorphic processes are unlikely to be the source of the positive $\delta^{15}N$ values seen in the Union Island Group black shale unit because of a small nitrogen isotope effect, typically on the order of +1 to +2 ‰, up to greenschist facies (Thomazo et al., 2011). In the aftermath of the GOE, the photic zone on the continental shelves remained at least mildly oxygenated as anoxia and redox-stratified conditions expanded during the Mesoproterozoic (Kipp et al. 2018; Stüeken, 2013; Stüeken et al. 2016). $\delta^{15}N$ values are reflective of ocean surface redox conditions and sinking of organic matter has been shown to carry its isotopic signature to deeper-water sediments (Stüeken et al.,

2016). It could be argued that the positive $\delta^{15}N$ values are not reflective of the redox state deep in the basin where the black shale unit was deposited, but rather reflective of aerobic processes in the overlying surface waters. While Fe-speciation indicates anoxic, ferruginous conditions deep in the basin, positive $\delta^{15}N$ values recorded in the black shale unit suggest that there were high enough dissolved oxygen concentrations for the growth of a bioavailable NO_3^- reservoir in the overlying shallow waters. Modeling of biogeochemical nitrogen cycle by Kipp et al. (2018) has showed that positive $\delta^{15}N$ values associated with nitrification outpacing denitrification can develop at dissolved oxygen concentrations > 4.5 μM O_2.

$\delta^{15}N$ values for the red and green mudstone (see **Figure 4.14-4.17**) are between -2 and +1 ‰ with the average of +1.7 ‰ and similar to those associated with nitrogen fixation (Kipp et al., 2018). Accounting for the possible +1 to +2 ‰ isotopic shift in greenschist facies (Thomazo et al., 2011), the red and green mudstone was likely deposited in an environment where the nitrogen cycle was dominated by fixation. One scenario that could explain this signature is nitrogen cycling within a photosynthetic microbial mat. Photosynthetic microbial mats have high biological productivity and high requirements for bioavailable nitrogen that are partially met through nitrogen fixation (Woebken et al., 2015). Oxygenic photosynthesis in the mat during the day produces oxygen, and bioavailable nitrogen is utilized through aerobic processes (Woebken et al., 2015). During the night when photosynthesis does not occur, the mat becomes anoxic, and nitrogen fixation dominates (Burow et al., 2013; Woebken et al., 2015). This scenario would require shallow-water depositional setting and is in disagreement with the

interpretation of Sheen et al. (2018), which suggested deposition of the red and green mudstone during subsidence in the East Arm basin. Furthermore, no microbial mat structures have been reported in the red and green mudstone. Another possible scenario is that deposition of the red and green mudstone occurred in deeper waters of the basin where nitrate was limited and fixation was the dominant process. In this case, cross-basinal trend in $\delta^{15}N$ values would be consistent with basinal trends recorded in the Mesoproterozoic Belt Supergroup and correlative Roper and Bangemall groups (Koehler et al. 2017; Stüeken et al. 2013), which show positive $\delta^{15}N$ values in shallow, near-shore facies, and $\delta^{15}N$ values consistent with nitrogen fixation in the deepwater facies.

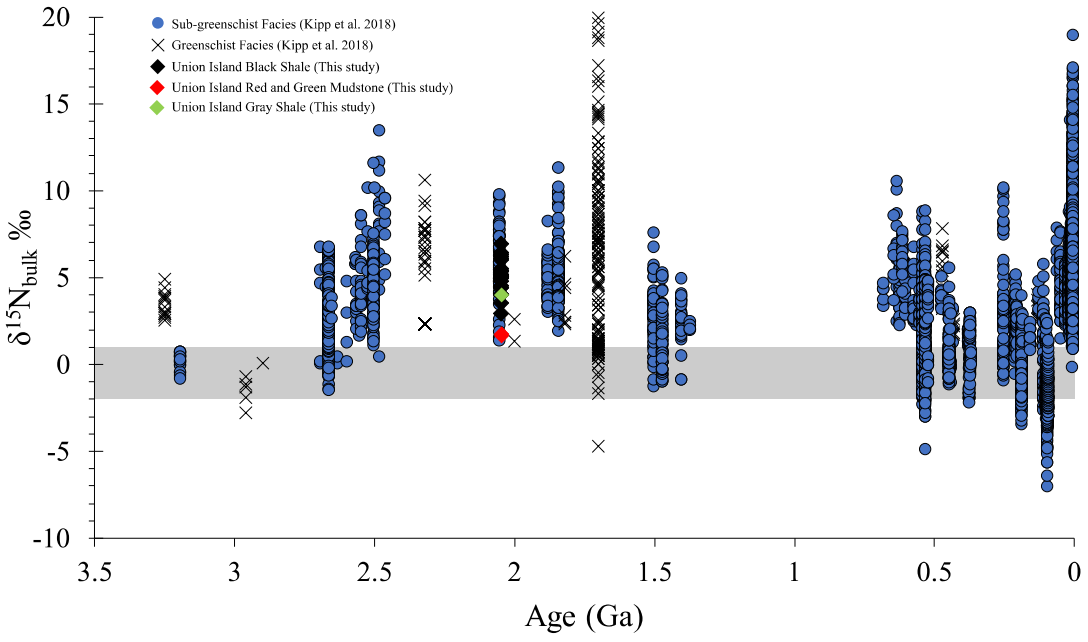

Figure 5.5.1: Nitrogen isotope values through time; modified from Kipp et al. (2018). Positive $\delta^{15}N$ values in the black shale unit (black diamonds) and gray shale (green diamond) are consistent with an aerobic nitrogen cycling. Nitrogen isotope values for red and green mudstone unit (red diamonds) are close to -2 to +1 ‰ values typically associated with nitrogen fixation (gray shaded area).

Organic carbon isotope values of organic matter have been linked to microbial processes during deposition and are controlled by the carbon isotopic values of the dissolved organic carbon (DOC) and dissolved inorganic carbon pools (DIC) (Melezhik et al., 1999). $\delta^{13}C_{org}$ values in settings where methanogenesis and methanotrophy take place are typically highly negative (Claypool & Kaplan 1974; Irwin et al. 1977; Friedman & Murata 1979; Talbot & Kelts 1986), whereas biomass that utilizes the enzyme Rubisco is generally heavier and has organic carbon isotope values of -26 ± 7 ‰ (Schidlowski, 2001). The organic carbon isotope record is difficult to constrain on a global scale due to its susceptibility to local factors such as redox state, nutrient supply, and aqueous CO_2 levels (Bekker et al., 2008; Hayes et al., 1999). Sediments with high TOC content are stronger influenced by secondary productivity, especially during the Precambrian when dissolved oxygen concentrations in the oceans were likely lower (Hayes et al., 1999; Slack et al., 2007).

Deposition of the black shale unit is thought to have occurred in deep waters below the storm wave base (Kipp et al., 2018) under ferruginous conditions as reflected by Fe-speciation data (**Figure 4.11**). Despite evidence for shallow waters being oxygenated (average $\delta^{15}N$ = +5.0 ‰), the highly negative $\delta^{13}C_{org}$ values of the black shale unit suggest that secondary productivity was active deeper in the basin, with both methanogenesis and methanotrophy involved. The highly negative $\delta^{13}C_{org}$ values of the Union Island Group black shale unit (with the average of -39.4 ‰) (**Figure 4.2, Figure 4.16**) are consistent with a significant contribution of methanotrophs. The $\Delta^{13}C$ values for

the twelve black shale samples yielded an average fractionation of 36.9 ‰, consistent with a carbon cycle including both primary producers and methane processing.

Unlike carbon isotope values for the black shale unit, organic carbon isotope values in the red and green mudstone are significantly heavier than those seen in the black shale, averaging -27.1 ‰ (**Figure 4.2, Figure 4.16**) and are consistent with primary producers utilizing oxygenic photosynthesis. Daytime oxygenic CO_2 fixation using Rubisco would produce $\delta^{13}C_{org}$ values heavier than the values associated with methane cycling (methanogenesis and methanotrophy) as seen in the black shale unit.

The $\delta^{13}C_{org}$ values recorded by the Union Island Group provide information regarding redox conditions and metabolisms in the East Arm basin during deposition, however their application to understanding the global $\delta^{13}C_{org}$ record is more complicated compared to the $\delta^{13}C_{carb}$ values recorded in the lower and upper dolostone units. Shallow-water marine carbonates provide the most faithful records of $\delta^{13}C_{org}$ because secondary productivity is restricted there to the anoxic pore waters beneath the sediment-water interface (Bekker et al., 2008). Susceptibility to factors such as redox state and nutrient availability (Bekker et al., 2008) in a restricted setting means the $\delta^{13}C_{org}$ values of the Union Island Group black shale unit, red and green mudstone unit, and gray shale are reflective of local biogeochemical carbon cycling in the East Arm basin.

Molybdenum

Average upper continental crust concentrations of molybdenum are low, between 1 and 2 ppm (Taylor and McLennan, 1995), and it is the most abundant transition metal in the modern oxygenated ocean with concentrations of ~105 nM (Collier, 1985; Scott and Lyons, 2012). Molybdenum concentrations in the ocean are fairly homogeneous, varying by less than 5% in the open ocean and is primarily controlled by oxidative weathering of crustal sulfides and black shales (Scott and Lyons, 2012). Under oxidizing conditions, Mo reacts with oxygen to form the molybdate oxyanion (MoO_4^{2-}) and has a residence time of ~800,000 years in the modern ocean (Broeker and Peng, 1982; Scott and Lyons, 2012). Under mildly sulfidic conditions, MoO_4^{2-} undergoes a series of reactions that produce particle-reactive thiomolybdate ions ($MoS_{4-x}O_x^{2-}$), which is adsorbed onto organic matter, or is precipitated as authigenic sulfide minerals (Helz et al., 1996; Scott and Lyons, 2012). In environments with sufficient delivery of iron and organic matter in the presence of free hydrogen sulfide (i.e. euxinic conditions), sediments become enriched in Mo, with values reaching 100s of ppm (Algeo and Lyons, 2006; Lyons et al., 2003; Scott et al., 2012). Work by Scott and Lyons (2012) showed concentrations of Mo in blacks shales that are above 1-2 ppm crustal level and below 25 ppm were generated in an environment where dissolved sulfide was present, but restricted to the pore waters. Concentrations between 25 and 100 ppm are representative of an euxinic environment that can be modified by the contribution of four factors: 1.) intermittent euxinia, 2) dilution of Mo enrichment due to anomalously high sedimentation

rates, 3) depletion of dissolved Mo from the water column, and 4) the effect of pH on Mo speciation (Scott and Lyons, 2012).

Mo concentrations in the black shale unit of the Union Island Group are predominately higher than crustal values, with concentrations ranging from 0.1 to 19.5 ppm, and the average concentration of 7 ppm. The concentration of Mo in the black shales of the Union Island Group indicates deposition in an anoxic, non-euxinic setting with hydrogen sulfide restricted to the pore waters, consistent with ferruginous conditions indicated by Fe-speciation (**Figure 4.11**). In contrast, the overlying red and green mudstone and gray shale do not appear to have been deposited under the same regime with Mo concentrations of 0.3 ppm and 0.1 ppm, respectively. The low concentrations of Mo below crustal levels is consistent with other proxies indicating oxic water column conditions at the depositional site.

Globally, black shales deposited under euxinic conditions have shown strong covariation between Mo concentrations and total organic carbon (Algeo and Lyons, 2006; Scott et al., 2008). TOC content for the Union Island Group black shales ranges between 0.3 and 6.3 wt % (**Table 2**) and averages 2.6 wt %. Covariation between Mo and TOC for the black shales is high ($R^2 = 0.51$), suggesting the Mo supplied to the East Arm basin during deposition of the black shale was adsorbed onto organic matter (**Figure 5.5.3**). Limited sample size for the red and green mudstone unit, and gray shale with low TOC content does not allow to constrain whether the same covariation is present.

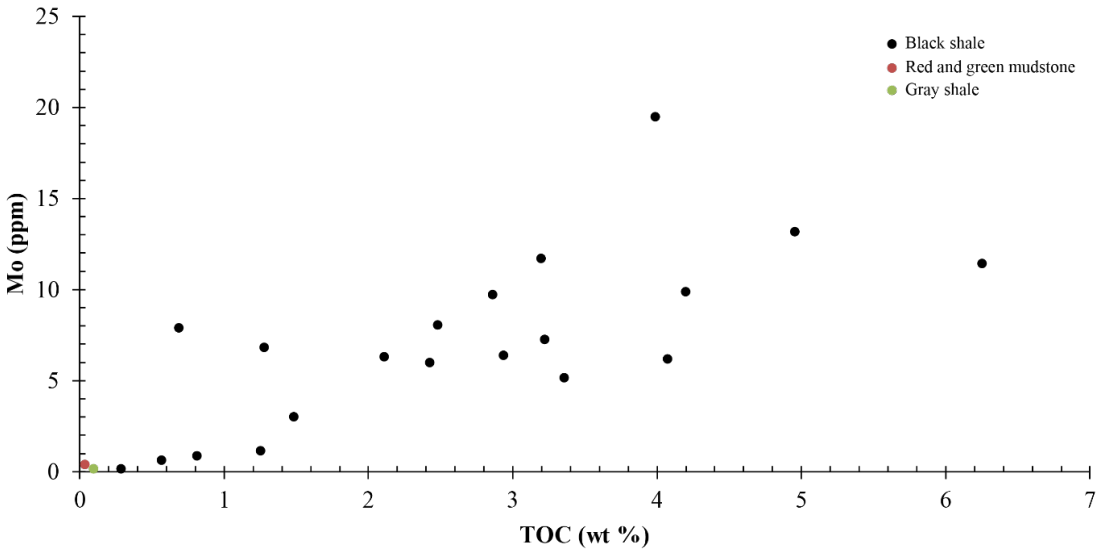

Figure 5.5.3: Mo concentrations in the Union Island Group black shale unit (black), red and green mudstone unit (red), and gray shale (green) samples. Covariation between Mo and TOC for the black shale unit ($R^2 = 0.54$) reflects adsorption of Mo onto organic matter (Algeo and Lyons, 2006; cf. Scott et al., 2012).

U/Th

There are two distinct geochemical states of uranium based on the local redox state (Partin et al., 2013). Under oxidizing regime, U^{6+} is mobilized to solution during weathering, while under reducing conditions U^{4+} is insoluble and precipitates out of solution (Langmuir, 1978). Unlike Mo, enrichment in U occurs under both low-oxygen and anoxic (both ferruginous and euxinic) water columns (Anderson et al., 1989; Dunk et al., 2002; Klinkhammer and Palmer, 1991; Partin et al., 2013), allowing for distinction between oxidizing and reducing settings, but not constraining the availability of free sulfide during deposition from the water column.

Uranium content for the Union Island Group black shale unit is higher than in the average upper continental crust, with values ranging between 2 and 14.1 ppm, and the average value of 6.6 ppm. Red and green mudstone samples have concentrations lower than those in the black shale unit ranging between 4.2 and 4.5 ppm, with the average value of 4.3 ppm. Unlike the black shale and red and green mudstone, the one gray shale sample had near crustal U concentration with a value of 2.5 ppm.

Insolubility of U^{4+} under reducing conditions can lead to enrichment in sediments above the average upper continental crustal concentration of 2.7 ppm (Rudnick and Gao, 2013), a signal that can be recorded in organics-rich shales (Anderson et al., 1989; Partin et al., 2013). The U content in organics-rich sediments roughly tracks the organic matter content (Dunk et al., 2002; Klinkhammer and Palmer, 1991; Tribovillard et al., 2006). Global compilation of U concentrations in organics-rich shales by Partin et al., (2013) divided Earth's history into four distinct stages on the basis of water column redox conditions: 1.) Archean through 2.32 Ga, 2.) 2.32 - 2.06 Ga, 3.) after ~2.06 Ga through the late Neoproterozoic, and 4.) the late Neoproterozoic through the entire Phanerozoic. Lomagundi-aged black shales fall within the stage 2, while deposition of the Union Island Group occurs during the early portion of the stage 3. The stage 2 organics-rich shales showed enrichments as high as 60 ppm in the ~2.32 Ga Timeball Hill and Rooihoogte formations in South Africa, with several shale units having between 40 and 50 ppm U (Partin et al., 2013). Average U content in the stage 2 organic-rich shales is 10.7 ppm (Partin et al., 2013), significantly higher than the average U concentrations of 6.4 ppm, 4.3 ppm, and 2.5 ppm in the Union Island Group black shale unit, red and green

mudstone unit, and gray shale. The stage 3 black shales during the period of ~2.06 Ga through the late Neoproterozoic show a substantial decrease in U content, with near the average upper continental crustal value of 3.8 ppm (Partin et al., 2013). This decrease in U concentrations across the stage 2 to stage 3 boundary, which coincides with the termination of the LE, suggests that there was a decrease in the U reservoir in the ocean stemming from the spread of ocean anoxia following an ocean deoxygenation event at the end of the Lomagundi excursion (Bekker and Holland, 2012; Kump et al., 2011; Ossa-Ossa et al., 2018; Partin et al., 2013). Uranium content in organics-rich sediments reflects the oxygenation state of the ocean-atmosphere system, with oxygen being required to mobilize oxidized U^{6+} to the ocean, and in reducing settings controls precipitation of insoluble reduced U^{4+} (Langmuir, 1978; Partin et al., 2013). With the exception of two outliers with the highest U contents, U concentrations and TOC content for the black shales show a positive linear correlation ($R^2 = 0.36$), suggesting that U enrichment in the black shale unit is likely tracking organic matter content.

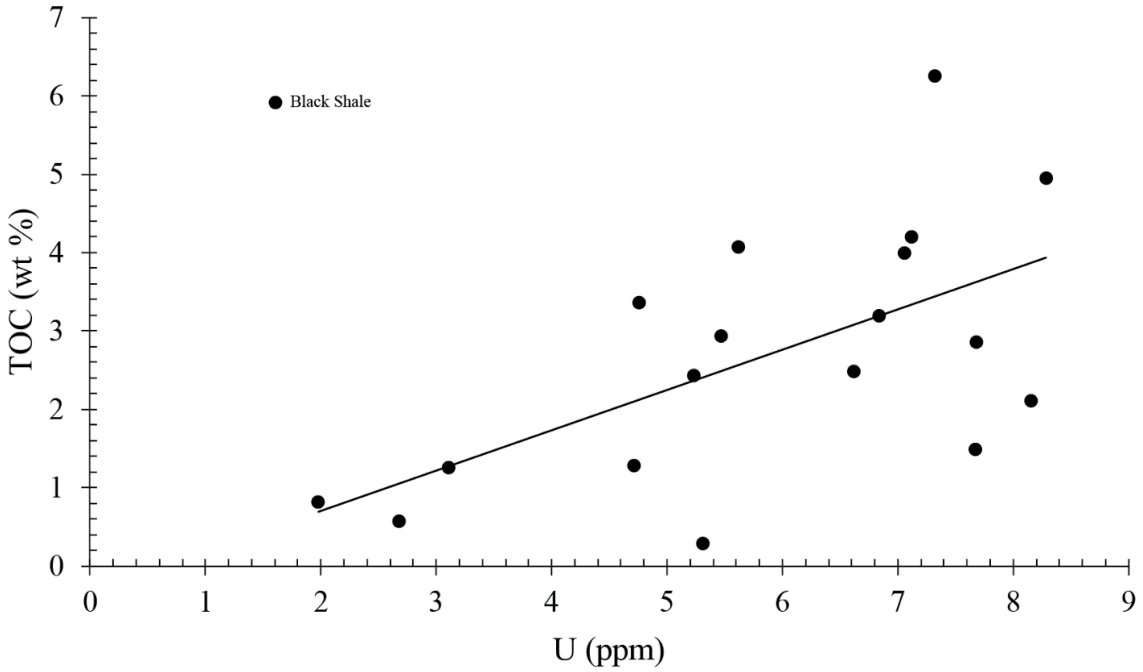

Figure 5.5.4: U (ppm) vs. TOC (wt. % C) for the Union Island Group black shale unit. Positive linear correlation ($R^2 = 0.36$) suggests that U concentrations track organic carbon content.

When U is assumed to be entirely in the detrital component of mudstones, the Th/U ratio is ~3 (Wignall and Myers, 1988). Authigenic enrichment in U is defined as $U_{auth} = U_{total}$-Th/3 (Wignall and Myers, 1988). Decarbonation of the carbonate fraction of the black shale samples accounts for the dilution effect by carbonate phases. Authigenic enrichment in U in the black shale supports deposition under anoxic conditions where U can be adsorbed onto particle-reactive surfaces such as organic matter or phosphate and precipitate out of solution to the sediments (Holland 1984; Kochenov et al., 1977). REE + Y patterns and Fe-speciation data suggest deposition of the black shale unit under ferruginous conditions in contrast to the U/Th proxy developed by Jones and Manning (1994) (see below). The red and green mudstone samples do not show authigenic

enrichment, potentially linked to deposition under more oxidizing conditions, while the gray shale appears to have also been deposited under ferruginous conditions consistent with Fe-speciation data.

Th at the surface conditions is highly immobile, and in mudstones is found in the detrital fraction associated with heavy minerals or clays (Jones and Manning, 1994). The average upper continental crust concentration of Th is 10.5 ppm (Rudnick and Gao, 2013). The Union Island Group black shale unit has Th content ranging from 2.8 to 26.6 ppm and is generally depleted compared to the average upper continental crust, with the average concentration of 8.7 ppm. The red and green mudstones are distinctly different, with all samples being enriched in Th compared to the average upper continental crust with concentrations ranging between 18.2 and 19.4 ppm, and the average of 18.9 ppm. The one gray shale sample is enriched in Th compared to the average upper continental crust with a Th having a concentration of 13.2 ppm. Enrichment in Th for the red and green mudstone and gray shale samples agrees well REE patterns reflecting terrigenous input from weathering of the crust (**Figure 4.12**). Delivery of detrital material enriched in Th via subaerial weathering on the land led to an excess of Th in the red and green mudstone and gray shale.

The redox-sensitive behavior of uranium results in higher U/Th in organic-rich sediments deposited under reducing conditions, allowing for U/Th ratios to be used as a redox indicator (Adams and Weaver, 1958; Jones and Manning, 1994; Rogers and Adams, 1969). Jones and Manning, (1994) showed that U/Th ratios are reflective of

redox state, and that sediments with U/Th ratios of <0.42 were characteristic of deposition under oxic conditions, >0.42 to <0.75 of dysoxic conditions, and >0.75 of suboxic to anoxic conditions. The black shales with the average U/Th ratio of U/Th = 0.86 suggest deposition under dysoxic conditions, while red and green mudstone (U/Th = 0.23) and gray shale (U/Th = 0.19) support deposition under oxic conditions (see **Figure 4.10**). The high U/Th ratios in the Union Island Group black shale unit are tracking organic matter content (see **Figure 5.4.5**) rather than siliciclastic contribution due to enrichments in U relative to crustal values and depletion in Th. The low TOC content in the red and green mudstone (0.04 wt %) and gray shale (0.1 wt %) indicates that organic matter is not a major host for U as it is in the black shale. U and Th enrichments in the red and green mudstone and Th enrichment in the grey shale deposited under oxic conditions can be explained by the composition of sediments derived from the provenance.

The application of the U/Th proxy of Jones and Manning (1994) to constrain paleoredox was developed on argillaceous rocks of Phanerozoic age, when oxygen concentrations in the atmosphere were consistently high. During the Precambrian when oxygen concentrations were lower, U content in the oceans was also likely lower, which could potentially result in U/Th ratios indicating oxic conditions according to the proxy developed by Jones and Manning (1994). For this reason, we prefer the use of Fe-speciation data as an indicator of redox conditions during deposition.

Ce Anomaly

REE+Y studies have shown that some REE, most notably Ce and Eu, are sensitive to redox conditions. The formation of the Ce_{SN} anomaly stems from the oxidation of Ce from its trivalent state to the less soluble Ce (IV), which is preferentially adsorbed onto particle surfaces (Bau and Dulski, 1996). In the modern ocean, oxygenated conditions drive Ce (III) oxidation to the less soluble Ce (IV), and its adsorption onto and removal with Mn-Fe oxyhydroxides, organic matter, and clay particles (Byrne and Sholkovitz, 1996; German et al., 1991; Planavsky et al., 2010). This results in modern seawater displaying a strong negative Ce anomaly when normalized to shale composites (Bolhar al., 2004; Planavsky et al., 2010). During much of the Precambrian however, shallow oxic waters were underlain by anoxic (ferruginous or euxinic) waters (Lyons et al., 2009; Reinhardt et al., 2013; Scott et al., 2008), separated by a redoxcline. Ce transported via adsorption onto Mn-Fe oxyhydroxides from the oxic shallow waters undergoes reductive dissolution across the redoxcline and released back into anoxic waters (Bau and Dulski, 1996; Planavsky et al., 2010). Under anoxic to suboxic ocean conditions, there is typically a lack of significant negative Ce_{SN} anomalies, with small negative or even positive Ce_{SN} anomalies typically occurring (Bau et al., 1997b; Byrne and Sholkovitz, 1996; German and Elderfield, 1990; Planavsky et al., 2010). Negative Ce_{SN} anomalies have been recorded in a few anoxic localities, namely in the Mesoproterozoic Zhengjiaya Formation and upper Taizi Formation on the Yangtze Black of the South China craton (Canfield et al., 2018), carbonate-rich sediments of the Arabian

Sea (Nath et al., 1997), and anoxic sediments of the Ordovician to early Silurian age in Scotland (Wilde et al., 1996).

Though Ce_{SN} anomalies commonly appear on REE + Y diagrams, it is necessary to determine whether they are representative of a true Ce_{SN} anomaly, or the result of a positive La anomaly (Bau and Dulski, 1996). Some marine metalliferous sediments and high-temperature hydrothermal fluids show anomalous concentrations of La (Bau and Dulski, 1996). Ce_{SN} anomaly $(Ce/Ce^*)_{SN}$[calculated as $Ce_{SN}/(0.5La_{SN} + 0.5Pr_{SN})$] is plotted versus Pr/Pr^*_{SN} [calculated as $Pr_{SN}/(0.5Ce_{SN} + 0.5Nd_{SN})$] to access the effect of anomalous concentrations of La onto the Ce_{SN} anomaly (cf. Bau and Dulski, 1996). $(Pr/Pr^*)_{SN} > 1$ results from a true negative Ce_{SN} anomaly, whereas $(Pr/Pr^*)_{SN} < 1$ could reflect a positive Ce_{SN} anomaly or a positive La anomaly if Ce_{SN} is less than 1. $(Pr/Pr^*)_{SN}$ between 0.95 and 1.05 are equivical to interpret (Bau and Dulski, 1996).

The Union Island Group black shale unit reveals that all black shale samples with the exception of one (UN-16-26) record a true negative Ce_{SN} anomaly (see **Figure 4.13**). UN-16-26 falls in the field that represents a positive La_{SN} anomaly with no Ce_{SN} anomaly (Bau and Dulski, 1996). Two of the three red and green mudstone samples and the gray shale sample fall inside of the field that represents a true negative Ce_{SN}, while the third red and green mudstone sample falls within the field that records neither a positive La_{SN} anomaly nor Ce_{SN} anomaly (Bau and Dulski, 1996) (**Figure 4.13**). Negative Ce_{SN} anomalies generally linked to deposition under oxic conditions. Oxygen concentrations must have been high enough in the East Arm basin to meet the threshold for oxidation of

Ce (III) and form a true negative Ce_{SN} anomaly. In redox-stratified waters, reductive dissolution of Mn-Fe oxyhydroxides across the redoxcline generally erases a negative Ce_{SN} anomaly from the underlying suboxic to anoxic waters (Byrne and Sholkovitz, 1996; German et al., 1991; Planavsky et al., 2010). Preservation of a negative Ce_{SN} anomaly in anoxic settings, though rare, is consistent with Fe-speciation data for the black shale and gray shale indicating ferruginous conditions. For this reason, it is inferred that the black shale and gray shale were deposited under anoxic, ferruginous conditions in close proximity to the redoxcline to preserve a true negative Ce_{SN} anomaly. In contrast, the red and green mudstone does not contain significant amounts of highly reactive iron or pyrite for Fe-speciation, has $\delta^{13}C_{org}$ values consistent with minor to no contribution from secondary productivity, and records a true negative Ce_{SN} anomaly suggesting that it was deposited under oxic conditions.

Section 5.6: Depositional setting and redox conditions during deposition of the Union Island Group

Utilization of proxy records for understanding environmental conditions during deposition is pivotal to understanding and evaluating past depositional environments. Integrating the geochemical proxies for the lower dolostone, black shale, upper dolostone, and red and green mudstone, reveals a dynamic depositional environment. We propose that the Union Island Group was deposited in redox-stratified basin in a restricted setting, where oxygenated shallow waters were underlain by deep waters with ferruginous conditions (**Figure 5.6.1**). Deposition of the lower dolostone, upper dolostone, and red and green mudstone are thought to have occurred under oxic

conditions, while the black shale was deposited under ferruginous conditions in close proximity to the redoxcline.

Deposition of the Union Island Group is envisioned within a failed rift developed in five stages originally described in Hoffman (1988b) and updated by Sheen et al. (2018). The lower dolostone and black shale were deposited during the stage one, when the Slave craton subsided (Sheen et al., 2018). Lower dolostones consistently record highly positive $\delta^{13}C_{carb}$ isotope values averaging +7.4 ‰, and $\delta^{13}C_{org}$ that are highly negative with the average of -31.1 ‰. Fractionation between $\delta^{13}C_{carb}$ and $\delta^{13}C_{org}$ produces $\Delta^{13}C$ values as large as 50.0 ‰ (see **Figures 5.3.1-5.3.3**) indicating contribution of organic matter from methanotrophs. Highly negative, but variable $\delta^{13}C_{org}$ values and consistently heavy $\delta^{13}C_{carb}$ values suggests that during deposition of the lower dolostone unit, secondary productivity was controlled by local factors, while the inorganic carbon pool for the basin was not.

Further subsidence of the Slave craton led to deposition of black shale in the deeper part of the basin during a transgression (Sheen et al., 2018). Fe-speciation of black shale samples (**Figure 4.11**) reveals that a majority of the samples have $Fe_{HR}/Fe_T > 0.38$ and $Fe_{py}/Fe_{HR} < 0.8$ consistent with deposition under anoxic ferruginous conditions (Anbar et al. 2008; Anderson and Raiswell, 2004; Lyons and Severmann, 2006). Y/Ho ratios are above that for PAAS, but well below open-marine values (40-80; Bau et al., 1997b; Tostevin et al., 2016), suggesting that the Union Island Group had limited connection to the ocean. High organic carbon content between 0.3 and 6.3 wt % recording highly negative $\delta^{13}C_{org}$ averaging -39.4 ‰ indicate high secondary productivity from

methanotrophs. Preservation of a true negative Ce_{SN} anomaly recorded in black shales suggests the presence of at least low concentrations of available oxygen in the overlying water column above the redoxcline. In redox-stratified waters, shuttling of Ce on particle-reactive surfaces such as Mn-Fe oxyhydroxides into reducing waters is quickly released as Mn-Fe oxyhydoxides are dissolved (Bau and Dulski, 1996; Planavsky et al., 2010). Preservation of a true negative Ce_{SN} anomaly under reducing conditions would require burial before Ce could be reduced and mobilized back into solution.

In the time immediately following the GOE, the photic zone on continental shelves remained mildly oxygenated, while extent of anoxia spread (Kipp et al., 2018; Stüeken, 2013; Stüeken et al., 2016). $\delta^{15}N$ values in black shales are positive (average = +5.0 ‰). These values are consistent +4 to +6 ‰ average in modern oceans reflecting aerobic nitrogen cycling (Tesdal et al., 2013). $\delta^{15}N$ values being typically reflective of surface processes, and through sinking can carry their isotopic signatures to deeper water lithologies (Stüeken, 2013; Stüeken et al., 2016). Deposition of organic matter derived from the oxygenated surface waters could transport their isotopic signal reflecting aerobic processes into the underlying anoxic waters deeper in the basin.

After emplacement of the lower basalt, and intrusions of mafic dikes and sills into the Slave craton during the stage two, a hiatus of volcanic activity and sea level regression lead to deposition of the upper dolostone during stage 3 (Sheen et al., 2018). The upper dolostone records $\delta^{13}C_{carb}$ values near zero averaging +0.5 ‰, and highly negative $\delta^{13}C_{org}$ averaging -29.5 ‰. Fractionation between the two pools reaches as high as 38.1 ‰ indicating a contribution of organic-matter from methanotrophs. Like the

lower dolostone unit, $\delta^{13}C_{carb}$ values were consistent, while $\delta^{13}C_{org}$ values were highly negative, with some variability. The same trend seen in the lower dolostone suggests that the dissolved inorganic carbon pool for the basin was not strongly affected by local secondary productivity.

Continued shallowing of the Slave craton during stage five led to deposition of the red and green mudstone (Sheen et al., 2018). $\delta^{13}C_{org}$ values in the red and green mudstone were heavier than those seen in the black shale, averaging -27.1 ‰, consistent -26 ± 7 ‰ $\delta^{13}C_{org}$ values associated with biological carbon fixation using Rubisco (Schidlowski, 2001; Stüeken and Buick, 2018). A shift in $\delta^{15}N$ towards the -2 to +1 ‰ range of nitrogen fixation (Zhang et al., 2014) is potentially reflective of basin gradients in nitrogen availability, with nitrate being more available in deeper-water settings. This is different from the trends in $\delta^{15}N$ values recorded in the Mesoproterozoic Belt Supergroup and correlative Roper and Bangemall groups (Koehler et al., 2017; Stüeken et al., 2013). $\delta^{15}N$ values of +1.7 ‰ in the red and green mudstone combined with preservation of a true negative Ce_{SN} anomaly suggest deposition under oxic conditions with low nitrate availability.

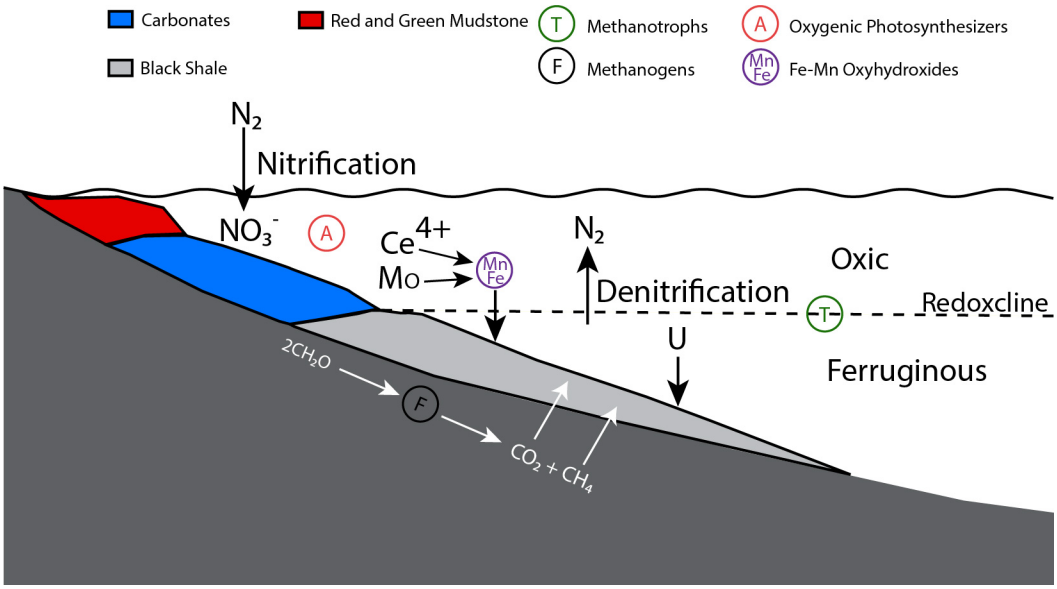

Figure 5.6.1: A biogeochemical model of carbon cycling and redox conditions in the East Arm basin during deposition of the Union Island Group (cf. Bekker et al., 2008). Oxygenated shallow waters harbored significant NO_3^- for aerobic nitrogen cycling and shuttling of trace metals (Mo) and REE (Ce^{4+}) on the surfaces of Mn-Fe oxyhydroxides into deeper waters below the redoxcline. Secondary productivity in the water column at the redoxcline (methanotrophy) and below the sediment-water interface (methanogenesis) contributed heavily to TOC during deposition of the black shale.

The carbon isotope values of the Union Island Group reflect significant changes to the biogeochemical carbon cycle in the East Arm basin. Highly positive $\delta^{13}C_{carb}$ isotopes recorded in the lower dolostone, followed by $\delta^{13}C_{carb}$ near zero in the upper dolostone reflects a major perturbation to the dissolved inorganic carbon pool, likely reflecting redox state of the ocean-atmosphere system. This challenges the conventional view that after the GOE there was long-term stability in the carbon cycle, and instead favors one that points towards a volatile state, fluctuating between highly positive and near zero values on short-term scales, likely tracking oxygen availability.

Conclusion

The Lomagundi Event (LE) is the longest-lived, highly positive carbon isotope excursion in Earth history, spanning 160 My between 2.22-2.06 Ga. It is characterized by high primary productivity and extensive organic carbon burial, releasing between 12 and 22 times the present atmospheric oxygen inventory to surface environments (Bekker and Holland, 2012; Karhu and Holland, 1996). Globally, $\delta^{13}C_{carb}$ values in carbonates deposited during the LE record highly positive values, averaging +8 ‰, and as high as +28 ‰ (Bekker, 2014; Bekker et al., 2003; Karhu and Holland, 1996). The termination of the LE is marked by the deposition of organic-rich lithologies in association with a proposed ocean deoxygenation event (Bekker and Holland, 2012; Kump et al., 2011). Conventionally, it has been believed that after the end of the LE carbon isotope values in carbonates return to "normal values" near 0 ‰ through the Mesoproterozoic during the "Boring Billion." Highly positive carbon isotope values in the ca. 2.03 Ga Wooly Dolomite of the Horseshoe rift basin in western Australia (Bekker et al., 2016) and the ca. 2.02 Ga Gumbi Group of the Limpopo Belt in South Africa (Buick et al., 2003) indicate there was at least one more highly positive carbon isotope excursion in the aftermath of the LE as opposed to the conventionally perceived long-term stability.

The Union Island Group has been interpreted as a stagnant, marine basinal to platformal succession (Hoffman et al., 1977; Sheen et al., 2018; Thorstad, 1976). We propose the Union Island Group was deposited in a restricted setting on the basis of highly radiogenic $^{87}Sr/^{86}Sr$ isotope values well above those of the contemporaneous seawater and Y/Ho ratios well below modern or ancient marine values. Rifting in the

Union Island basin at ca. 2045.1 ± 1 Ma (Sheen et al., 2018) did not result in a passive continental margin setting as the subsequent, ca. 1.93 Ga terrestrial rifting event during deposition of the Wilson Group (Bowring and Hoffman, 1984; Johnson, 1990) led to a passive continental margin deposition culminating with magmatism in the 1.86 Ga Taltson magmatic zone and deformation of the Great Slave Lake shear zone at 1.78 Ga (Hanmer et al., 1992; Sheen et al., 2018). This is further supported by a lack of oceanic crust and seismic reflection data at the Slave-Rae boundary arguing against ocean subduction (Snyder and Kjarsgaard, 2007).

U/Pb dating of zircons from a volcanoclastic unit in the lower basalt by Sheen et al. (2018) constrained the age of the Union Island Group to 2045 ± 1 Ma, post-dating the end of the LE, and pre-dating the highly positive carbon isotope excursion recorded by the ca. 2.03 Ga Wooly Dolomite. The highly positive $\delta^{13}C_{carb}$ values of the lower dolostone unit, averaging +7.4 ‰, are consistent with a highly positive carbon isotope excursion at ca. 2045 ± 1 Ma. Diagenetic cross-plots for the lower and upper dolostone units suggest that the Union Island Group dolostones have been subjected to post-depositional alteration, but do not explain the highly positive $\delta^{13}C_{carb}$ values recorded by the lower dolostone unit. Values near 0 ‰ recorded by the upper dolostone unit upsection show the inorganic carbon pool in the basin returned to "normal" carbon isotope composition. In addition, large $\Delta^{13}C$ values, as large as 50.0 ‰ for the lower dolostone unit and 38.1 ‰ for the upper dolostone unit, indicate contribution to organic matter derived from methanotrophic metabolism. Consistent, highly positive $\delta^{13}C_{carb}$ values in the lower dolostone unit and near-to-zero $\delta^{13}C_{carb}$ values in the upper dolostone unit, with

highly variable $\delta^{13}C_{org}$ values suggest that while $\delta^{13}C_{org}$ values were affected by local processes, the dissolved inorganic carbon pool in the basin was in a steady state. Lack of evidence for strong influence of evaporitic conditions, highly variable $\delta^{13}C_{carb}$ values due to methanogenesis near the sediment-water interface, and deposition under locally high primary productivity suggests that $\delta^{13}C_{carb}$ values in the lower and upper dolostone units are reflective of basin waters.

Deposition of the black shale unit between the two dolostone units reflects a period of high organic carbon burial with TOC content reaching as high as 6.3 wt. % and marks the end of the highly positive $\delta^{13}C_{carb}$ excursion. Highly negative $\delta^{13}C_{org}$ values as low as -43.1 ‰ and $\Delta^{13}C$ values as high as 36.9 ‰ indicate contribution to bulk organic matter from secondary productivity. Positive nitrogen isotopes recorded by the black shale unit point to oxygenated shallow waters undergoing nitrification-denitrification, while Fe-speciation indicates that ferruginous conditions prevailed in the deeper part of the basin. Preservation of a true negative Ce_{SN} anomaly in the black shale unit further suggests it was deposited in close proximity to, but below the redoxcline.

The red and green mudstone unit at the top of the Union Island Group records $\delta^{13}C_{org}$ values (~ -27.1 ‰) consistent with primary productivity and preserves a negative Ce_{SN} anomaly, reflecting deposition in shallower and, at least mildly, oxic waters. $\delta^{15}N$ values, slightly above those characteristic for nitrogen fixation and averaging +1.7 ‰, suggest that nitrate availability was limited, potentially linked to a contraction in oxygen availability during deposition of the underlying upper dolostone unit.

Carbon isotopes of carbonates from the Union Island Group in the East Arm basin suggest that the lower dolostone unit of the Union Island Group records potential evidence for a previously unrecognized, highly positive carbon isotope excursion in the aftermath of the GOE at ca. 2045 Ma and before the Wooly Dolomite carbon isotope excursion. The global extent of the carbon isotope excursion remains uncertain, but opens up the possibility that some units with poor age constraints that have been correlated to the LE might coincide with a short-lived highly positive excursion at ca. 2045 Ma. Volatility in the carbon isotope values of carbonates deposited in the aftermath of the LE suggest that there was a prolonged instability in the biogeochemical carbon cycle tied to the redox state of the atmosphere marking the transition from the LE to the Boring Billion of the Middle Proterozoic.

References

Adams, J.A.S. and Weaver, C.E., 1958. Thorium to uranium ratios as indicators of sedimentary processes -- Examples of the concept of geochemical facies. Am. Assoc. Pet. Geol. Bull., 42: 387-430.

Ader M., Thomazo C., Sansjofre P., Busigny V., Papineau D., Laffont R., Cartigny P. and Halverson G. P. (2016) Interpre- tation of the nitrogen isotopic composition of Precambrian sedimentary rocks: Assumptions and perspectives. Chem. Geol. 429, 93–110.

Algeo, T.J., 2004. Can marine anoxic events draw down the trace element inventory of seawater? Geology 32, 1057–1060.

Algeo, T. J., & Lyons, T. W. (2006). Mo-total organic carbon covariation in modern anoxic marine environments: Implications for analysis of paleoredox and paleohydrographic conditions. *Paleoceanography*, *21*(1). https://doi.org/10.1029/2004PA001112

Anderson, R.F., Fleisher, M.Q., LeHuray, A.P., 1989. Concentration, oxidation state, and particulate flux of uranium in the Black Sea. Geochim. Cosmochim. Acta 53, 2215–2224.

Anderson, T. F., & Raiswell, R. (2004). Sources and mechanisms for the enrichment of highly reactive iron in euxinic Black Sea sediments. American Journal of Science, 304, 203233. https://doi.org/10.2475/ ajs.304.3.203

Arndt, N.T., Nelson, D.R., Compston, W., Trendall, A.F., Thorne, A.M., 1991. The age of the Fortescue Group, Hamersley Basin, Western Australia, from ion microprobe zircon U–Pb results. Aust. J. Earth Sci. 38, 261–281

Bachan, A. & Kump, L. R. The rise of oxygen and siderite oxidation during the Lomagundi event. Proc. Natl Acad. Sci. 112, 6562–6567 (2015).

Badham, J. P. N., Stanworth, C. W (1984). Lower Proterozoic red beds, evaporites and secondary sedimentary uranium deposits from the East Arm, Great Slave Lake, Canada. *Journal of the Geological Society of London*, *141*(2), 235–242. https://doi.org/10.1144/gsjgs.141.2.0235

Bau, M., Dulski, P., 1996. Distribution of yttrium and rare-earth elements in the Penge and Kuruman iron-formations, Transvaal Supergroup, South Africa. Precambrian Res. 79, 37–55.

Bau, M., Möller, P., Dulski, P., 1997. Yttrium and lanthanides in eastern Mediterranean seawater and their fractionation during redox-cycling. Mar. Chem. 56, 123–131. http://dx.doi.org/10.1016/S0304-4203(96)00091-6.

Bau, M., 1999. Scavenging of dissolved yttrium and rare earths by precipitating iron oxyhydroxide: experimental evidence for Ce oxidation, Y-Ho fractionation, and lanthanide tetrad effect. Geochim. Cosmochim. Acta 63, 67–77.

Bekker, A., Karhu, J. A., Eriksson, K. A., & Kaufman, A. J. (2003). Chemostratigraphy of Paleoproterozoic carbonate successions of the Wyoming Craton: tectonic forcing of biogeochemical change? (Vol. 120).

Bekker, A., Sial, A.N., Karhu, J.A., Ferreira, V.P., Noce, C.M., Kaufman, A.J., Romano, A.W., Pimentel, M.M., 2003b. Chemostratigraphy of carbonates from Minas Supergroup, Quadrilatero Ferifero (Iron Quadrangle), Brazil: a stratigraphic record of early Proterozoic atmospheric, biogeochemical and climatic change. Am. J. Sci. 303, 865–904.

Bekker, A., Holland, H. D., Wang, P. L., Rumble, D., Stein, H. J., Hannah, J. L., … Beukes, N.J. (2004). Dating the rise of atmospheric oxygen. *Nature*, *427*(6970), 117–120. https://doi.org/10.1038/nature02260

Bekker, A., Holmden, C., Beukes, N. J., Kenig, F., Eglingtone, B., & Patterson, W. P. (2008). Fractionation between inorganic and organic carbon during the Lomagundi (2.22-2.1?? Ga) carbon isotope excursion. *Earth and Planetary Science Letters*, *271*(14), 278 291. https://doi.org/10.1016/j.epsl.2008.04.02

Bekker, A., Beukes, N. J., Strauss, H., & Niekerk, H. S. Van. (2008). Rise in seawater sulphate concentration associated with the Paleoproterozoic positive carbon isotope excursion: evidence Lucknow Formation, South Africa. https://doi.org/10.1111/j.13653121.2008.00795.x

Bekker, A., & Holland, H. D. (2012). Oxygen overshoot and recovery during the early Paleoproterozoic. *Earth and Planetary Science Letters*, *317–318*, 295–304. https://doi.org/10.1016/j.epsl.2011.12.012

Bekker, A., Planavsky, N. J., Krapez, B., Rasmussen, B., Hofmann, A., Slack, J. F., … Konhauser, K. O. (2013). Iron Formations: Their Origins and Implications for Ancient Seawater Chemistry. Treatise on Geochemistry: Second Edition (2nd ed., Vol. 9). Elsevier Ltd. https://doi.org/10.1016/B978-0-08-095975-7.00719-1

Bekker, A., 2014. Lomagundi carbon isotope excursion. In: Encyclopedia of Astrobiology. Springer-Verlag, pp. 1–6.

Bekker, A., Krapež, B., Müller, S. G., & Karhu, J. a. (2016). A short-term, post Lomagundi positive C isotope excursion at *c.* 2.03 Ga recorded by the Wooly Dolomite, Western Australia. *Journal of the Geological Society*, *173*(4), 689 700.https://doi.org/10.1144/jgs2015-152

Bellefroid, E. J., Hood, A. v. S., Hoffman, P. F., Thomas, M. D., Reinhard, C. T., and Planavsky, N. J., 2018, Constraints on Paleoproterozoic atmospheric oxygen levels: Proceedings of the National Academy of Sciences of the United States of America, v. 115, n. 32, p. 8104–8109, https://doi.org/10.1073/ pnas.1806216115

Berman, R.G., Sanborn-Barrie, M., Stern, R.A., Carson, C.J., 2005. Tectonometamorphism at ca. 2.35 and 1.85 Ga in the Rae domain, Western Churchill Province, Nunavut, Canada: insights from structural, metamorphic and in situ geochronological analysis of the southwestern Committee Bay Belt. Can. Mineral. 43, 409–442.

Berman, R.G., Pehrsson, S., Davis, W.J., Ryan, J.J., Qui, H., Ashton, K.E., 2013. The Arrowsmith orogeny: geochronological and thermobarometric constraints on its extent and tectonic setting in the Rae craton, with implications for pre-Nuna supercontinent reconstruction. Precambrian Res. 232, 44–69

Berner RA, Raiswell R. 1983. Burial of organic carbon and pyrite sulfur in sediments over Phanerozoic times: A new theory. Geochim. Cosmochim. Acta 47:855–62

Berner, R.A., 1984. Sedimentary pyrite formation: an update. Geochim. Cosmochim. Acta, 48: 605-615.

Berner R. A. and Raiswell R. (1984) C/S method for distinguishing freshwater from marine sedimentary rocks. Geology 12,365-368.

Berner, R.A., 2009. Phanerozoic atmospheric oxygen: new results using the Geocarbsulf Model. Am. J. Sci. 309, 603–606.

Bhatia, M. R, and Crook, K.A.W, 1986, Trace element characteristics of graywackes and tectonic setting discrimination of sedimentary basins: Contributions to Mineralogy and Petrology, v. 92, p. 181-193.

Bleeker, W., Stern, R., & Sircombe, K. (2000). Why the Slave Province, Northwest Territories, got a little bigger. *Geological Survey of Canada, Current Research*, *2000-C2*, 9 pp.

Bleeker, W., 2003. The late Archean record: a puzzle in ca. 35 pieces. Lithos 71, 99–134

Bleeker, W., and Hall, B., 2007. The Slave Craton: geological and metallogenic evolution. In: Goodfellow, W.D. (Ed.), Mineral Resources of Canada: A Synthesis of Major Deposit-types, District Metallogeny, the Evolution of Geological Provinces, and Exploration Methods. Geological Survey of Canada Special Publication 5, pp. 849–879.

Bolhar, R., Kamber, B. S., Moorbath, S., Fedo, C. M., & Whitehouse, M. J. (2004). Characterisation of early Archaean chemical sediments by trace element signatures, *222*, 43–60. https://doi.org/10.1016/j.epsl.2004.02.016

Bowring, S. A., Schmus, W. R. Van, & Hoffman, P. F. (1984). U–Pb zircon ages from Athapuscow aulacogen, East Arm of Great Slave Lake, N.W.T., Canada. Canadian Journal of Earth Sciences, 21(11), 1315–1324. https://doi.org/10.1139/e84-136

Broecker, W.S., 1970. A boundary condition on the evo- lution of atmospheric oxygen. J. Geophys. Res., 75: 3553-3557.

Broecker, W.S., Peng, T.H., 1982. Tracers in the Sea. Eldigio Press, Columbia University, Palisades, NY. 689 pp.

Brimhall, C. H, and 9 others, 1991, Deformational mass transport and invasive processes in soil evolution: Science, v. 255, p. 695-702.

Buchan, K.L., Ernst, R.E., Bleeker, W., Davis, W.J., Villeneuve, M., van Breemen, O., Hamilton, M.A., and Soderlund, U. 2010. Proterozoic magmatic events of the Slave craton, Wopmay Orogen and environs. Open File 5958, Geological Survey of Canada, Ottawa, Ont.

Buchan, K.L., LeCheminant, A.N., van Breemen, O., 2012. Malley diabase dykes of the Slave craton, Canadian Shield: U–Pb age, paleomagnetism, and implications for continental reconstructions in the early Paleoproterozoic. Canadian Journal of Earth Sciences 49, 435–454.

Buick, R., Des Marais, D.J., Knoll, A.H., 1995. Stable isotopic compositions of carbonates from the Mesoproterozoic Bangemall group, northwestern Australia. Chemical Ge- ology 123 (1–4), 153–171.

Buick, I. S.,Williams, I. S., Gibbson, R. L., Cartwright, I. & Miller, J. A. (2003). Carbon and U-Pb evidence for a Palaeoproterozoic crustal component in the Central Zone of the Limpopo Belt, South Africa. Journal of the Geological Society, London 160, 601-612.

Burow, L. C., Woebken, D., Marshall, I. P. G., Lindquist, E. A., Bebout, B. M., Prufert-Bebout, L., … Singer, S. W. (2013). Anoxic carbon flux in photosynthetic microbial mats as revealed by metatranscriptomics. *ISME Journal*, *7*(4), 817–829. https://doi.org/10.1038/ismej.2012.150

Byrne, R.H., Kim, K.-H., 1990. Rare earth element scavenging in seawater. Geochim. Cosmochim. Acta 54, 2645–2656. http://dx.doi.org/10.1016/0016 7037(90)90002-3.

Byrne R. and Sholkovitz E. (1996) Marine chemistry and geochemistry of the lanthanides. In Handbook on the Physics and Chemistry ofthe Rare Earths (eds. K. A. Gschneider Jr. and L. Eyring). Elsevier, Amsterdam.

Canfield, D.E., 1998. A new model for Proterozoic ocean chemistry. Nature 396, 450 -453.

Canfield, D. E., Zhang, S., Frank, A. B., Wand, X., Wang, H., Su, J., Ye, Y., and Frei, R., 2018, Highly fractionated chromium isotopes in Mesoproterozoic-aged shales and atmospheric oxygen: Nature Communications, v. 9, n. 1, article number 2871, https://doi.org/10.1038/s41467-018-05263-9

Cavell, P.A., Baadsgaard, H., 1986. Geochronology of the Big Spruce Lake alkaline intrusion. Canadian Journal of Earth Sciences 23, 1–10.

Claypool, G., Presley, B. J. & Kaplan, I. R. in Initial Reports of the Deep Sea Drilling Project 19, 879 (US Government Printing Office, Washington D.C. 1973).

Claypool, G.E. & Kaplan, I.R. 1974. The origin and distribution ofmethane in marine sediments. In: Kaplan, I.R. (ed.) Natural Gases in Marine Sediments. Plenum, New York, 99–139.

Collier, R.W., 1985. Molybdenum in the Northeast Pacific Ocean. Limnology and Oceanography 306, 1351–1354.

Condie, K.C. and Wronkiewicz, D.J., 1990. A new look at the Archean-Proterozoic boundary: Sediments and the tectonic setting constraint. In: S.M. Naqvi (Editor), Precambrian Continental Crust and Its Economic Resources. Elsevier, Amsterdam, pp. 61-84.

Condie, K.C., 1993. Chemical composition and evolution of the upper continental crust: contrasting results from surface samples and shales. Chem. Geol. 104, 1–37.

Courtillot, V., Jaupart, C., Manighetti, I., Tapponnier, P., Besse, J., 1999. On causal links between flood basalts and continental breakup. Earth Planet. Sci. Lett. 166, 177 195.

Cullers, R.L., Basu, A., Suttner, L.J., 1988. Geochemical signature of provenance in sand-size material in soils and stream sediments near the Tobacco Root batholith, Montana, U.S.A. Chem. Geol. 70, 335–348. https://doi.org/10.1016/0009 2541(88)90123-4

Cullers, R.L., 1994. The controls on the major and trace element variation of shales, siltstones, and sandstones of Pennsylvanian-Permian age from uplifted continental blocks in Colorado to platform sediment in Kansas, USA. Geochim. Cosmochim. Acta 58, 49554972. https://doi.org/10.1016/0016-7037(94)90224-0

Cullers, R., 2000. Geochemistry of the Mesoproterozoic Lakhanda shales in southeastern Yakutia, Russia: implications for mineralogical and provenance control, and recycling. Precambrian Res. 104, 77–93. https://doi.org/10.1016/S0301 9268(00)00090-5

Daly, J.S., Balagansky, V.V., Timmerman, M.J., Whitehouse, M.J., 2006. The Lapland -Kola orogen: Palaeoproterozoic collision and accretion of the northern lithosphere. In: Gee, D.G., Stephenson, R.A. (Eds.), European Lithosphere Dynamics, 32. Geol. Soc. London Memoirs, pp. 561–578.

DePaolo, D.J., Wasserburg, G.J., 1976. Nd isotopic variations and petrogenetic models. Geophys. Res. Lett. 3, 249–252.

Diamond, C. W., Planavsky, N. J., Wang, C., & Lyons, T. W. (2018). What the ~1.4 Ga Xiamaling Formation can and cannot tell us about the mid-Proterozoic ocean. *Geobiology*, (October 2017), 1–18. https://doi.org/10.1111/gbi.12282

Douville, E., Bienvenu, P., Charlou, J.L., Donval, J.P., Fouquet, Y., Appriou, P., Gamo, T., 1999. Yttrium and rare earth elements in fluids from various deep-sea hydrothermal systems. Geochim. Cosmochim. Acta 63, 627–643. 7037(99)00024 1.

Dunk, R.M., Mills, R.A., Jenkins, W.J., 2002. A reevaluation of the oceanic uranium budget for the Holocene. Chem. Geol. 190, 45–67

Elderfield, H.,Upstill-Goddard,R., Sholkovitz,E.R., 1990.The rare earth elements in rivers, estuaries, and coastal seas and their significance to the composition of ocean waters. Geochim. Cosmochim. Acta 54, 971–991. http://dx.doi.org/10.1016/00167037(90)90432-K.

Elderfield, H., C. J. Hawkesworth, M. J. Greaves and S. E. Calvert, Rare earth element geochemistry of oceanic ferromanganese nodules and associated sediments, Geochim. Cosmochim. Acta, 45, 513-528, 1981.

Emerson, S. R., and S. S. Huested (1991), Ocean anoxia and the concentrations of molybdenum and vanadium in seawater, Mar. Chem., 34, 177–196.

Farquhar, J., Bao, H. & Thiemens, M. Atmospheric influence of Earth's earliest sulfur cycle. Science 289, 756–758 (2000)

Floyd, P.A., Leveridge, B.E., 1987. Tectonic environment of the Devonian Gramscatho basin, south Cornwall: framework mode and geochemical evidence from turbiditic sandstones. J. Geol. Soc. 144, 531–542. https://doi.org/10.1144/gsjgs.144.4.0531

Frauenstein, F., Veizer, J., Beukes, N., van Niekerk, H.S., Coetzee, L.L., 2009. Transvaal Supergroup carbonates: implications for Paleoproterozoic $\delta^{18}O$ and $\delta^{13}C$ records. Precambrian Res. 175, 149–160.

Friedman, I. &Murata, K.J. 1979. Origin of dolomite in Miocene Monterey Shale and related formations in the Temblor Range, California. Geochimica et Cosmochimica Acta, 43,1357–1365.

Frimmel, H. E. (2009). Trace element distribution in Neoproterozoic carbonates as palaeoenvironmental indicator. *Chemical Geology*, *258*(3–4), 338–353. https://doi.org/10.1016/j.chemgeo.2008.10.033

Gao, S., & Wedepohl, K. H. (1995). The negative Eu anomaly in Archean sedimentary rocks: Implications for decomposition, age and importance of their granitic sources. *Earth and Planetary Science Letters*, *133*(1–2), 81–94. https://doi.org/10.1016/0012-821X(95)00077-P

Gauthier-Lafaye, F., 2006. Time constraint for the occurrence of uranium deposits and natural nuclear fission reactors in the Paleoproterozoic Franceville Basin (Gabon). Geol. Soc. Am. Mem. 198, 157–167.

German C. R. and Elderfield H. (1990) Application of the Ce- anomaly as a paleoredox indicator: the ground rules. Paleoceanography 5, 823–833.

German C. R., Holliday B. P. and Elderfield H. (1991) Redox cycling of rare earth elements in the suboxic zone of the Black Sea. Geochim. Cosmochim. Acta 55, 3553–3558.

Gibb, R.A., and Thomas, M.D. 1977. The Thelon front: a cryptic suture in the Canadian Shield? Tectonophysics, 38: 211–222.

Goldstein, S.J., Jacobsen, S.B., 1988. Nd and Sr isotopic systematics of river water suspended material: implications for crustal evolution. Earth and Planetary Science Letters 87 (3),249–265.

Grotzinger, J.P., Kasting, J.F., 1993. New constraints on Precambrian ocean composition. J. Geol. 101, 235–243.

Gumsley, A.P., Chamberlain, K.R., Bleeker, W., Söderlund, U., de Kock, M.O., Larsson, E.R., Bekker, A., 2017. Timing and tempo of the Great Oxidation Event. Proc. Natl. Acad. Sci.USA 114, 1811–1816. https://doi .org /10 .1073 /pnas .1608824114.

Haendel, D., Muehle, K., Nitzsche, H.-M., Stiehl, G., Wand, U., 1986. Isotopic variations of the fixed nitrogen in metamorphic rocks. Geochim. Cosmochim. Acta 50, 749

Hayes, J.M., 1983. Geochemical evidence bearing on the origin of aerobiosis, a speculative hypothesis. In: Schopf, J.W. (Ed.), Earths Earliest Biosphere: Its Origin and Evolution. Princeton University Press, Princeton.

Helz, G.R., Miller, C.V., Charnock, J.M., Mosselmans, J.F.W., Patrick, R.A.D., Garner, D.D., Vaughan, D.J., 1996. Mechanism of molybdenum removal from the sea and its concentration in black shales: EXAFS evidence. Geochimica et Cosmochimica Acta 60, 3631–3642.

Hennessy, J. & Knauth, L.P. 1985. Isotopic variations in dolomite concretions from the Monterey Formation, California. Journal of Sedimentary Petrology, 55, 120–130. 758.

Hoffman, P. F. (1968). Stratigraphy of the Great Slave Supergroup (Aphebian), East Arm of Great Slave Lake, District of Mackenzie. Geological Survey of Canada, Paper 68-42, 92p

Hoffman, P. (1969). Proterozoic paleocurrents and depositional history of the East Arm fold belt Great Slave Lake, Northwest Territories. Canadian Journal of Earth Sciences, 6, pp. 441-462.

Hoffman, P.F. (1973). Evolution of an Early Proterozoic continental margin: The Coronation geosyncline and associated aulacogens, northwest Canadian Shield. In Evolution of the Precambrian crust. Edited by J. Sutton and B. F. Windley. Philosophical Transactions of the Royal Society of London, Series A, 273, pp.547-581.

Hoffman, P., Dewey, J. F., & Burke, K. (1974). Aulacogens and their genetic relations to geosynclines, with a Proterozoic example from Great Slave Lake, Canada. *Modern and Ancient Geosynclinal Sedimentation*, (1964), 38–55.

Hoffman, P. F., Bell, I. R., Hildebrand, R. S., and Thorstad, L. 1977. Geology of the Athapuscow aulacogen, East Arm of Great Slave Lake, District of Mackenzie. In Report of activities, part A. Geological Survey of Canada, Paper 77-IA, pp. 117-129

Hoffman, P.F., 1987. Continental transform tectonics: great Slave Lake shear zone (ca. 1.9 Ga), northwest Canada. Geology 15, 785–788

Hoffman, P.F., 1988a. Geology and tectonics. East Arm of Great Slave Lake, Northwest Territories. Geological Survey of Canada Map 1628A, 2 sheets.

Hoffman, P.F., 1988b. United plates of America, the birth of a Craton: early Proterozoic assembly and growth of Laurentia. Annu. Rev. Earth Planet. Sci. 16, 543–603.

Hoffman, P.F., Bowring, S.A., Buchwaldt, R., Hildebrand, R.S., 2011. Birthdate for the Coronation paleocean: age of initial rifting in Wopmay orogen, Canada. Can. J. Earth Sci.48, 281–293.

Holland, H.D., 1984, The chemical evolution of the atmosphere and oceans: Princeton, New Jersey, Princeton University Press, Series in Geochemistry, 582 p.

Holland, H.D., 2002. Volcanic gases, black smokers, and the Great Oxidation Event: Geochim. Cosmochim. Acta 66, 3811–3826.

Holland, H.D., 2006. The oxygenation of the atmosphere and oceans. Philosophical Transactions of the Royal Society B: Biological Sciences 361 (1470), 903–915.

Horie, K., Hidaka, H., Gauthier-Lafaye, F., 2005. U–Pb geochronology and geochemistry of zircon from the Franceville series at Bidoudouma, Gabon. In: Goldschmidt Conference Abstracts, Accessory Mineral Geochemistry I, p. A11.

Irwin, H., Curtis, C. & Coleman, M. 1977. Isotopic evidence for source of diagenetic carbonates formed during burial of organic-rich sediments. Nature, 269, 209–213.

Izon, G., Zerkle, A. L., Williford, K. H., Farquhar, J., Poulton, S. W., & Claire, M. W. (2017). Biological regulation of atmospheric chemistry en route to planetary oxygenation. *Proceedings of the National Academy of Sciences*, *114*(13), E2571–E2579. https://doi.org/10.1073/pnas.1618798114

Jackson M. J., Sweet I. P., Page R.W. & Bradshaw B. E. 1999. The South Nicholson and Roper Groups: evidence for the early Mesoproterozoic Roper Superbasin. In: Bradshaw B. E. & Scott D. L. eds. Integrated Basin Analysis of the Isa Superbasin using Seismic, Well-log and Geopotential Data: an Evaluation of the Economic Potential of the Northern Lawn Hill Platform (unpaginated). Australian Geological Survey Organisation Record 1999/19.

Johnson, B.J., 1990. Stratigraphy and structure of the Early Proterozoic Wilson Island Group, East Arm thrust-fold belt, N.W.T. Can. J. Earth Sci. 27, 552–569.

Jones, B., & Manning, D. A. C. (1994). Comparison of geochemical indices used for the interpretation of palaeoredox conditions in ancient mudstones. *Chemical Geology*, *111*(14), 111–129. https://doi.org/10.1016/0009-2541(94)90085-X

Karhu, J. A., 1993, Paleoproterozoic evolution of the carbon isotope ratios of sedimentary carbonates in the Fennoscandian Shield: Geological Survey of Finland Bulletin 371, 87 p.

Karhu, J. A., & Holland, H. D. (1996). Carbon isotopes and the rise of atmospheric oxygen. *Geology*, *24*(10), 867–870. https://doi.org/10.1130/00917613(1996)024<0867:CIATRO>2.3.CO

Kaufman, A.J. & Knoll, A.H. 1995. Neoproterozoic variations in the C-isotopic composition of seawater: stratigraphic and biogeochemical implications. Precambrian Research, 73,27–49.

Keith, M. L. and Weber, J. N., 1964, Isotopic composition and environmental classification of selected limestones and fossils: Geochim. et Cosmochim. Acta, v. 28, p. 1787 1816.

Kipp, M. A., Stüeken, E. E., Bekker, A., & Buick, R. (2017). Selenium isotopes record extensive marine suboxia during the Great Oxidation Event. *Proceedings of the National Academy of Sciences*, 201615867. https://doi.org/10.1073/pnas.1615867114

Kipp, M. A., Stüeken, E. E., Yun, M., Bekker, A., & Buick, R. (2018). Pervasive aerobic nitrogen cycling in the surface ocean across the Paleoproterozoic Era. *Earth and Planetary Science Letters*, *500*, 117–126. https://doi.org/10.1016/j.epsl.2018.08.007

Kjarsgaard, B.A., Pearson, D.G., DuFrane, A., and Heaman, L.M., 2013a. Proterozoic geology of the east arm basin wth emphasis on Paleoproterozoic magmatic rocks, Thaidene Nene MERA study area. In: Wright, D.F., Ambrose, E.J., Lemkow, D., and Bonham-Carter, G. (Eds.), Mineral and energy resource assessment of the proposed Thaidene Nene National Park Reserve in the area of the east arm of Great Slave Lake, Northwest Territories. Geological Survey of Canada Open File 7196, pp. 51–92.

Kjarsgaard, B.A., Tella, S., Lemkow, D., 2013b. Bedrock geology of the proposed Thaidene Nene National Park Reserve in the area of the East Arm of Great Slave Lake, Northwest Territories. In: Wright, D.F., Ambrose, E.J., Lemkow, D., and Bonham-Carter, G. (Eds.), Mineral and energy resource assessment of the proposed Thaidene Nene National Park Reserve in the area of the east arm of Great Slave Lake, Northwest Territories. Geological Survey of Canada Open File 7196, sheet.

Klinkhammer, G., Palmer, M., 1991. Uranium in the oceans—where it goes and why. Geochim. Cosmochim. Acta 55, 1799–1806.

Kochenov, A.V., Korolev, K.G., Dubinchuk, V.T., and Medvedev, Y.L., 1977, Experimental data on the conditions of precipitation of uranium from aqueous solutions (translated from Geokhimiya, v. 11, p. 1711-1716): Geochemistry International, 1977, p. 82-87.

Koehler, M. C., Stüeken, E. E., Kipp, M. A., Buick, R., & Knoll, A. H. (2017). Spatial and temporal trends in Precambrian nitrogen cycling: A Mesoproterozoic offshore nitrate minimum. *Geochimica et Cosmochimica Acta*, *198*, 315–337. https://doi.org/10.1016/j.gca.2016.10.050

Koehler, M. C., Buick, R., Kipp, M. A., Stüeken, E. E., & Zaloumis, J. (2018). Transient surface ocean oxygenation recorded in the ~2.66-Ga Jeerinah Formation, Australia. *Proceedings of the National Academy of Sciences*, *115*(30), 7711–7716. https://doi.org/10.1073/pnas.1720820115

A.B. Kuznetsov, V. A. Melezhik, I. M. Gorokhov, N. N. Melnikov, G. V. Konstantinova, E. P. Kutyavin, T. L. Turchenko, Sr isotopic composition of Paleoproterozoic 13C rich carbonate rocks: The Tulomozero Formation, SE Fennoscandian Shield. Precambrian Res.182, 300–312 (2010).

Krapež, B., Müller, S.G. & Bekker, A. 2015. Stratigraphy of the Late Palaeoproterozoic (~2.03 Ga) Wooly Dolomite, Ashburton Province, Western Australia: a carbonate platform developed in a failed rift basin. Precambrian Research, 271,1–19.

Kump, L. R., Junium, C., Arthur, M. A., Brasier, A., Fallick, A., Melezhik, V., … Luo, G. (2011). Isotopic Evidence for Massive Oxidation of Organic Matter Following the Great Oxidation Event. *Science*, *334*(6063), 1694–1696 https://doi.org/10.1126/science.1213999

Langmuir, D., 1978. Uranium solution-mineral equilibria at low temperatures with applications to sedimentary ore deposits. Geochim. Cosmochim. Acta 42, 547 569.

Lawrence, M. G., Greig, A., Kenneth, D., & Kamber, B. S. (2006). Rare Earth Element and Yttrium Variability in South East Queensland Waterways, 39–72. https://doi.org/10.1007/s10498-005-4471-8

Lazar, Boaz., Erez, Jonathon; Extreme ^{13}C depletions in seawater-derived brines and their implications for the past geochemical carbon cycle. *Geology* ; 18 (12): 1191–1194. doi: https://doi.org/10.1130/0091-7613(1990)018<1191:ECDISD>2.3.CO;2

Luo, G., Junium, C. K., Izon, G., Ono, S., Beukes, N. J., Algeo, T. J., … Summons, R. E. (2018). Nitrogen fixation sustained productivity in the wake of the palaeoproterozoic great oxygenation event. *Nature Communications*, *9*(1). https://doi.org/10.1038/s41467-018-03361-2

Lyons, T.W., Werne, J.P., Hollander, D.J., Murray, R.W., 2003. Contrasting sulfur geochemistry and Fe/Al and Mo/Al ratios across the last oxic-to-anoxic transition in the Cariaco Basin, Venezuela. Chemical Geology 195, 131–157.

Lyons, T. W., & Severmann, S. (2006). A critical look at iron paleoredox proxies: New insights from modern euxinic marine basins. Geochimica et Cosmochimica Acta, 70, 5698–5722. https://doi.org/10.1016/j. gca.2006.08.021

Lyons, T. W., Anbar, A. D., Severmann, S., Scott, C., & Gill, B. C. (2009). Tracking euxinia in the ancient ocean: A multiproxy perspective and Proterozoic case study. Annual Review of Earth and Planetary Sciences, 37, 507–534. https://doi.org/10.1146/annurev. earth.36.031207.124233

Lyons, T. W., Reinhard, C. T., & Planavsky, N. J. (2014). The rise of oxygen in Earth's Early ocean and atmosphere. Nature, 506(7488), 307-315. https://doi.org/10.1038/nature13068

Maheshwari, A., Sial, A. N., Gaucher, C., Bossi, J., Bekker, A., Ferreira, V. P., & Romano, A. W. (2010). Global nature of the Paleoproterozoic Lomagundi carbon isotope excursion: A review of occurrences in Brazil, India, and Uruguay. *Precambrian Research*, *182*(4), 274–299. https://doi.org/10.1016/j.precamres.2010.06.017

Martin, A. P., Condon, D. J., Prave, A. R., Melezhik, V. A., Lepland, A., & Fallick, A. E. (2013). Dating the termination of the Palaeoproterozoic Lomagundi-Jatuli carbon isotopic event in the North Transfennoscandian Greenstone Belt. *Precambrian Research*, *224*, 160–168. https://doi.org/10.1016/j.precamres.2012.09.010

Martin, A. P., Prave, A. R., Condon, D. J., Lepland, A., Fallick, A. E., Romashkin, A. E., … Rychanchik, D. V. (2015). Multiple Palaeoproterozoic carbon burial episodes and excursions. *Earth and Planetary Science Letters*, *424*, 226–236. https://doi.org/10.1016/j.epsl.2015.05.023

MacRae, N.D., Nesbitt, H.W. and Kronberg, B.I., 1992. Development of a positive Eu anomaly during diagenesis. Earth Planet. Sci. Lett., 109: 585-591.

Masuzawa, T. and Koyama, M., 1989. Settling particles with positive Ce anomalies from the Japan Sea. Geophys. Res. Lett., 16: 503-506.

McLennan, S. M., 1989a, Rare earth elements in sedimentary rocks: Influence of provenance and sedimentary processes: Mineralogical Society of America Reviews in Mineralogy, v. 21, p. 169-200.

McLennan, S. M., and Hemming, S., 1992, Samarium/neodymium elemental and isotopic systematics in sedimentary rocks: Geochimica et Cosmochimica Acta, v. 56, p. 887-898.

McLennan, S.M., Hemming, S., McDaniel, D.K., Hanson, G.N., 1993. Geochemical approaches to sedimentation, provenance, and tectonics, in: Geological Society of America Special Papers. Geological Society of America, pp. 21–40. https://doi.org/10.1130/SPE284-p21

McLennan, S.M., Bock, B., Hemming, S.., Hurowitz, J.A., Lev, S.., McDaniel, D.K., 2003. The roles of provenance and sedimentary processes in the geochemistry of sedimentary rocks, in: Geochemistry of Sediments and Sedimentary Rocks: Evolutionary Considerations to Mineral Deposit-Forming Environments. Geological Association of Canada, pp. 7–38.

McCrea, J.M., 1950. On the isotopic chemistry of carbonates and a paleotemperature scale. J. Chem. Phys. 18, 849–857.

Melezhik, V. A. (1999). Karelian shungite — an indication of 2.0-Ga-old metamorphosed oil-shale and generation of petroleum: geology , lithology and geochemistry.

Melezhik, V.A., Fallick, A.E., Medvedev, P.V., Makarihin, V.V., 1999. Extreme 13Ccarb enrichment in ca 2.0 Ga magnesite-stromatolite-dolomite-"red beds" association in a global context: a case for the world-wide signal enhanced by a local environment. Earth Sci. Rev. 48, 71–120.

Melezhik, V.A., Fallick, A.E., Kuznetsov, A.B., 2005a. Palaeoproterozoic, rift-related, 13C-rich, lacustrine carbonates, NW Russia. Part II: Global isotopic signal recorded in the lacustrine dolostone. Trans. Roy. Soc. Edinburgh Earth Sci. 95, 423–444.

Melezhik, V.A., Fallick, A.E., Rychanchik, D.V., Kuznetsov, A.B., 2005b. Palaeoproterozoic evaporites in Fennoscandia: implications for seawater sulphate, the rise of atmospheric oxygen and local amplification of the ʕ13C excursion. Terra Nova 17, 141–148.

V.A. Melezhik et al. (eds.), Reading the Archive of Earth's Oxygenation, Volume 3: Global Events and the Fennoscandian Arctic Russia - Drilling Early Earth Project, DOI 10.1007/978-3-642-29670-3_3, # Springer-Verlag Berlin Heidelberg 2013

Melezhik VA, Huhma H, Condon DJ, Fallick AE, Whitehouse MJ (2007) Temporal constraints on the Paleoproterozoic Lomagundi- Jatuli carbon isotopic event. Geology 35:655–658

Meyer, E. E., Quicksall, A. N., Landis, J. D., Link, P. K., & Bostick, B. C. (2012). Trace and rare earth elemental investigation of a Sturtian cap carbonate, Pocatello, Idaho: Evidence for ocean redox conditions before and during carbonate deposition. *Precambrian Research*, *192–195*(1), 89–106. https://doi.org/10.1016/j.precamres.2011.09.015

Michard, A., Albarede, F., Michard, G., Minster, J.F., Charlou, J.L., 1983. Rare-earth elements and uranium in high-temperature solutions from East Pacific Rise hydrothermal vent field (13 Degrees North). Nature 303, 795–797.

Mitchell, R.N., Bleeker, W., van Breemen, O., LeCheminant, T.N., Peng, P., Nilsson, M.K., Evans, D.A., 2014. Plate tectonics before 2.0 Ga: Evidence from paleomagnetism of cratons within supercontinent Nuna. American Journal of Science 314, 878–894

Morgan, W.J., 1971. Convective plumes in the lower mantle. Nature 230, 42–43.

Mulder, A., Van de Graaf, A.A., Robertson, L.A., Kuenen, J.G., 1995. Anaerobic ammonium oxidation discovered in a denitrifying fluidized-bed reactor. FEMS Microbiol. Ecol 16 (3), 177–183.

Mumford, T.R., Cousens, B.C., 2014. Constraints on the relationships between Paleoproterozoic intrusions and dyke swarms, East Arm of Great Slave Lake, N.W.T., Canada. Can. J. Earth Sci. 51, 19–438.

Nagender Nath, B., Bau, M., Ramalingeswara Rao, B., & Rao, C. M. (1997). Trace and rare earth elemental variation in Arabian Sea sediments through a transect across the oxygen minimum zone. *Geochimica et Cosmochimica Acta*, *61*(12), 2375 2388. https://doi.org/10.1016/S0016-7037(97)00094-X

Niemann, J.C. & Read, J.F. 1988. Regional cementation from unconformity- recharged aquifer and burial fluids, Mississippian Newman Limestone, Kentucky. Journal of Sedimentary Petrology, 58, 688–705.

Y. Nozaki, Y.S. Zhang, H. Amakawa, The fractionation between Y and Ho in the marine environment, Earth and Planetary Science Letters 148 (1997) 329–340.

Och, L. M., & Shields-Zhou, G. A. (2012). The Neoproterozoic oxygenation event: Environmental perturbations and biogeochemical cycling. Earth-Science Reviews, 110(1–4), 2657. https://doi.org/10.1016/j.earscirev.2011.09.004

O'Neil, J.R. (1987) Preservation of H, C, and O isotopic ratios in the low temperature environment., in: Kyser, T.K. (Ed.), Stable Isotope Geochemistry of Low Temperature Fluids. Mineralogical Association of Canada, Saskatoon, pp. 85-128.

Ossa, F., Eickmann, B., Hofmann, A., Planavsky, N. J., Asael, D., Pambo, F., & Bekker, A. (2018). Two-step deoxygenation at the end of the Paleoproterozoic Lomagundi Event. *Earth and Planetary Science Letters*, *486*, 70–83. https://doi.org/10.1016/j.epsl.2018.01.009

G. V. Ovchinnikova, A. B. Kuznetsov, V. A. Melezhik, I. M. Gorokhov, I. M. Vasil'eva, B. M. Gorokhovskii, Pb-Pb age of Jatulian carbonate rocks: The Tulomozero Formation of southeast Karelia. Stratigr. Geol. Correl. 15, 359–372 (2007). doi:10.1134/S0869593807040028

Partin, C. A., & Konhauser, K. (2013). Large-scale fluctuations in Precambrian atmospheric and oceanic oxygen levels from the record of U in shales, (June). https://doi.org/10.1016/j.epsl.2013.03.031

Pesonen, L.J., Elming, S.A., Mertanen, S., Pisarevsky, S., D'Agrella-Filho, M.S., Meert, J.G., Schmidt, P.W., Abrahamsen, N., Bylund, G., 2003. Palaeomagnetic configuration of continents during the Proterozoic. Tectonophysics 375, 289–324.

Piper, D. Z., Rare earth elements in ferromanganese nodules and other marine phases, Geochim. Cosmochim. Acta, 38, 1007-1022, 1974b.

Planavsky, N.J., Reinhard, C.T., Wang, X., Thomson, D., McGoldrick, P., Rainbird, R.H., Johnson, T., Fischer, W.W., Lyons, T.W., 2014b. LowMid-Proterozoic atmospheric oxygen levels and the delayed rise of animals. Science 346 (6209), 635–638.

Planavsky, N., et al., 2010. Rare earth element and yttrium compositions of Archean and Paleoproterozoic Fe formations revisited: new perspectives on the significance and mechanisms of deposition. Geochim. Cosmochim. Acta 74 (22), 6387–6405.

Pope, M.C., Grotzinger, J.P., 2003. Paleoproterozoic Stark Formation, Athapsuscow Basin, Northwest Canada: record of cratonic-scale salinity crisis. J. Sed. Res. 73, 280–295.

Poulton, S. W., & Canfield, D. E. (2005). Development of a sequential extraction procedure for iron: Implications for iron partitioning in continentally derived particulates. *Chemical Geology*, *214*(3–4), 209–221. https://doi.org/10.1016/j.chemgeo.2004.09.003

Quan, T. M. and Falkowski, P. G. (2009), Redox control of N:P ratios in aquatic ecosystems. Geobiology, 7: 124-139. doi:10.1111/j.1472-4669.2008.00182.x

Raiswell R. and Bemer R. A. (1986) Pyrite and organic matter in Phanerozoic normal marine shales. Geochim. Cosmochim. Acta 50, 1967- 1976.

Raiswell, R., Buckley, F., Berner, R.A. and Anderson, T.F., 1988. Degree of pyritization of iron as a paleoenvironmental indicator of bottom-water oxygenation. J. Sedi-iment. Petrol., 58:812-819.

Reinhard C. T., Planavsky N. J., Robbins L. J., Partin C. A., Gill B. C., Lalonde S. V., Bekker A., Konhauser K. O. and Lyons T. W. (2013) Proterozoic ocean redox and biogeochemical stasis. Proc. Natl. Acad. Sci. U.S.A. 110, 5357–5362.

Rogers, J.J.W. and Adams, J.A.S., 1969. Abundances in rock forming minerals (I), uranium minerals (II). In: K.H. Wedepohl (Editor), The Handbook of Geo-chemistry, Sect. 92-D. Springer, Berlin, pp. 92-D1-92- D2.

Rudnick, R. L., & Gao, S. (2013). *Composition of the Continental Crust*. *Treatise on Geochemistry: Second Edition* (2nd ed., Vol. 4). Elsevier Ltd. https://doi.org/10.1016/B978-0-08-095975-7.00301-6

Schidlowski, M., Eichmann, R., and Junge, C. E., 1976, Carbon isotope geochemistry of the Precambrian Lomagundi carbonate province, Rhodesia: Geochimica et Cosmochimica Acta, v. 40, p. 449–455

Schidlowski, M., 2001. Carbon isotopes as biogeochemical recorders of life over 3.8 Ga of Earth history: evolution of a concept. Precambr. Res. 106, 117–134.

Schröder, S., Bekker, A., Beukes, N.J., Strauss, H. & Niekerk, H.S.V. 2008. Rise in seawater sulphate concentration associated with the Paleoproterozoic positive carbon isotope excursion: evidence from sulphate evaporites in the ~2.2–2.1 Gyr shallow-marine Lucknow Formation, South Africa. Terra Nova, 20, 108–117.

Scoates, J.S., Friedman, R.M., 2008. Precise age of the platiniferous Merensky Reef, Bushveld Complex, South Africa, by the U–Pb zircon chemical abrasion ID TIMS technique. Econ. Geol. 103, 465–471.

Scott, C., Lyons, T. W., Bekker, A., Shen, Y., Poulton, S. W., Chu, X., & Anbar, A. D. (2008). Tracing the stepwise oxygenation of the Proterozoic ocean. *Nature*, *452*(7186), 456–459. https://doi.org/10.1038/nature06811

Scott, C., Wing, B. A., Bekker, A., Planavsky, N. J., Medvedev, P., Bates, S. M., … Lyons, T. W. (2014). Pyrite multiple-sulfur isotope evidence for rapid expansion and contraction of the early Paleoproterozoic seawater sulfate reservoir. *Earth and Planetary Science Letters*, *389*, 95–104. https://doi.org/10.1016/j.epsl.2013.12.010

Schimmelmann, A., Mastalerz, M., Gao, L., Sauer, P.E., Topalov, K., 2009. Dike intrusions into bituminous coal, Illinois Basin: H, C, N, O isotopic responses to rapid and brief heating. Geochim. Cosmochim. Acta 73 (20), 6264–6281.

Schimmelmann, A., Lis, G.P., 2010. Nitrogen isotopic exchange during maturation of organic matter. Org. Geochem. 41 (1), 63–70.

Severmann S, Lyons TW, Anbar A, McManus J, Gordon G. 2008. Modern iron isotope perspective on Fe shuttling in the Archean and the redox evolution of ancient oceans. Geology 36:487–90

Sheen, A.I., 2017. Geochronological and geochemical constraints on the origin of the Paleoproterozoic Union Island Group mafic magmatism, East Arm Basin, N.W.T. MSc thesis. University of Alberta, Edmonton, pp. 170.

Sheen, A. I., Heaman, L. M., Kjarsgaard, B., Ootes, L., Graham Pearson, D., & Creaser, R. A. (2018). Athapuscow aulacogen revisited: geochronology and geochemistry of the 2046 Ma Union Island Group mafic magmatism, East Arm of Great Slave Lake, Northwest Territories, Canada. *Precambrian Research*, *321*(November 2018), 85–102. https://doi.org/10.1016/j.precamres.2018.11.012

Shields, G., Veizer, J., 2002. Precambrian marine carbonate isotope database: Version 1.1. Geochem. Geophys. Geosyst. 3, 1–12.

Sholkovitz, E.R., Landing, W.M. and Lewis, B.L., 1994. Ocean particle chemistry: the fractionation of rare earth elements between suspended particles and seawater. Geochim. Cosmochim. Acta, 58: 1567-1579.

Sinclair, W.D., Hunt, P.A., and Birkett, T.C., 1994. U-Pb zircon and monazite ages of the Grace Lake Granite, Blatchford Lake Intrusive Suite, Slave Province, Northwest Territories, In Radiogenic Age and Isotopic Studies: Report 8; Geological Survey of Canada, Current Research 1994-F, p. 15-20.

Slack, J.F., Grenne, T., Bekker, A., Rouxel, O.J., Lindberg, P.A., 2007. Suboxic deep seawater in the late Paleoproterozoic: evidence from hematitic chert and iron formation related to seafloor-hydrothermal sulfide deposits, central Arizona, USA. Earth Planet. Sci. Lett. 255, 243–256

Snyder, D.B., Kjarsgaard, B.A., 2013. Mantle roots of major Precambrian shear zones inferred from structure of the Great Slave Lake shear zone, northwest Canada. Lithosphere 5, 539–546.

Stiller, M., Rounick, J.S., and Shasha, S., 1985, Extreme carbon-isotope enrichments in evaporating brines: Nature, v. 316, p. 434-435.

Stüeken, E. E. (2013). A test of the nitrogen-limitation hypothesis for retarded eukaryote radiation: Nitrogen isotopes across a Mesoproterozoic basinal profile. *Geochimica et Cosmochimica Acta*, *120*, 121–139. https://doi.org/10.1016/j.gca.2013.06.002

Stüeken, E. E., Buick, R., & Schauer, A. J. (2015). Nitrogen isotope evidence for alkaline lakes on late Archean continents. *Earth and Planetary Science Letters*, *411*(2), 1–10. https://doi.org/10.1016/j.epsl.2014.11.037

Stüeken, E. E., Kipp, M. A., Koehler, M. C., & Buick, R. (2016). The evolution of Earth's biogeochemical nitrogen cycle. *Earth-Science Reviews*, *160*, 220–239. https://doi.org/10.1016/j.earscirev.2016.07.007

Stüeken, E. E., Zaloumis, J., Meixnerová, J., & Buick, R. (2017). Differential metamorphic effects on nitrogen isotopes in kerogen extracts and bulk rocks. *Geochimica et Cosmochimica Acta*, *217*, 80–94. https://doi.org/10.1016/j.gca.2017.08.019

Stüeken, E. E., & Buick, R. (2018). Environmental control on microbial diversification and methane production in the Mesoarchean. *Precambrian Research*, *304*(August 2017), 64–72. https://doi.org/10.1016/j.precamres.2017.11.003

Talbot, M.R. & Kelts, K. 1986. Primary and diagenetic carbonates in the anoxic sediments of Lake Bosumtwi, Ghana. Geology, 14, 912–916.

Taylor, S. R., McLennan, S. M,, and McCulloch, M. T,, 1983, Geochemistry of loess, continental crustal composition and crustal model ages: Geochimica et Cosmochimica Acta, v. 47, p. 1897-1905.

Tesdal, J. E., Galbraith, E. D., & Kienast, M. (2013). Nitrogen isotopes in bulk marine sediment: Linking seafloor observations with subseafloor records. *Biogeosciences*, *10*(1), 101–118. https://doi.org/10.5194/bg-10-101-2013

Thorstad, L., 1976. Structure, stratigraphy and petrology of the Union Island group, East Arm of Great Slave Lake, NWT. Unpublished B.Sc. thesis. University of British Columbia, Vancouver, pp. 55 p.

Tirrul, R., Grotzinger, J.P., 1990. Early Proterozoic collisional orogeny along the northern Thelon tectonic zone, Northwest Territories, Canada: evidence from the foreland. Tectonics 9, 1015–1036.

Tostevin, R., Shields, G. A., Tarbuck, G. M., He, T., Clarkson, M. O., & Wood, R. A. (2016). Effective use of cerium anomalies as a redox proxy in carbonate-dominated marine settings. *Chemical Geology*, *438*, 146–162. https://doi.org/10.1016/j.chemgeo.2016.06.027

Tribovillard, N., Algeo, T.J., Lyons, T., Riboulleau, A., 2006. Trace metals as paleoredox and paleoproductivity proxies: an update. Chem. Geol. 232, 12–32

van Breemen, O., Kjarsgaard, B.A., Tella, S., Lemkow, D., Aspler, L., 2013. U–Pb detrital zircon geochronology of clastic sedimentary rocks of the Paleoproterozoic Nonacho and EastArm basins, East Arm MERA study area, Chapter 4. In: Wright, D.F., Ambrose, E.J., Lemkow, D., and Bonham-Carter, G. (Eds.), Mineral and energy re- source assessment of the proposed Thaidene Nene National Park Reserve in the area of the east arm of Great Slave Lake, Northwest Territories. Geological Survey of Canada Open File 7196, pp. 95–118.

Van de Graaf, A.A., Mulder, A., de Bruijn, P., Jetten, M.S., Robertson, L.A., Kuenen, J.G., 1995. Anaerobic oxidation of ammonium is a biologically mediated process. Appl. Environ. Microbiol 61 (4), 1246–1251.

Veizer, J. (1989). Strontium Isotopes in Seawater Through Time Strontium Isotope Systematics. *Ann. Rev. Earth Planet. Sci*, *17*(3), 14167. https://doi.org/10.1146/annurev.ea.17.050189.001041

Veizer J., Clayton R. N., and Hinton R. W. (1992a) Geochemistry of Precambrian carbonates: IV. Early Paleoproterozoic (2.25 2 ± 0.25 Ga) seawater. Geochim. Cosmochim. Acta 56, 875-885.

Veizer J., Plumb K. A., Clayton, R. N., Hinton, R. W., and Grotzinger, J. P. (1992b) Geochemistry of Precambrian carbonates: V. Late Paleoproterozoic (1.8 ± 0.25 Ga) sea water. Geochim. Cosmochim. Acta 56, 2487-2501.

Veizer J. and Compston W. (1974) $^{87}Sr/^{86}Sr$ composition of seawater during the Phanerozoic. Geochim. Cosmochim. Acta 38, 1461-1484.

Wanke, A., Melezhik, V.A., 2005. Palaeoproterozoic sedimentation and stromatolite growth in an advanced intracontinental rift associated with the marine realm: a record of the Neoarchaean continent breakup? Precambrian Res. 140, 1–35.

Weber, J.N., Bergenback, R.E., Williams, E.G. and Keith, M.L. (1965) Reconstruction of depositional environments in the Pennsylvanian Vanport basin by carbon isotope ratios. Journal of Sedimentary Petrology 35, 36-48.

Wheat, C.G., Mottl, M.J., Rudnicki, M., 2002. Trace element and REE composition of a low-temperature ridge-flank hydrothermal spring. Geochimica et Cosmochimica Acta 66, 3693–3705.

Wignall, P.B., Myers, K.J., 1988. Interpreting benthic oxygen levels in mudrocks: a new approach. Geology 16, 452–455.

Wilde, P., 1987. Model of progressive ventilation of the late Precambrian–early Paleozoic ocean. Am. J. Sci. 287, 442–459.

Wingate, M.T.D., 2002. Age and palaeomagnetism of dolerite sills of the Bangemall Supergroup on the Edmund 1:250000 map sheet W.A. Western Australia Geological Survey, pp. 48.

Winter, B.L. & Knauth, L.P. 1992a. Stable isotope geochemistry of carbonate fracture fills in the Monterey Formation, California. Journal of Sedimentary Petrology, 62, 208–219.

Winter, B.L. & Knauth, L.P. 1992b. Stable isotope geochemistry of cherts and carbonates from the 2.0 Ga Gunflint Iron Formation: implications for the depositional setting, and the effects of diagenesis and metamorphism. Precambrian Research, 59, 283–313.

Woebken, D., Burow, L. C., Behnam, F., Mayali, X., Schintlmeister, A., Fleming, E. D., Bebout, B. M. (2015). Revisiting N2 fixation in Guerrero Negro intertidal microbial mats with a functional single-cell approach. *ISME Journal*, *9*(2), 485–496. https://doi.org/10.1038/ismej.2014.144

Wronkiewicz, D.J., Condie, K.C., 1987. Geochemistry of Archean shales from the Witwatersrand Supergroup, South Africa: Source-area weathering and provenance. Geochim. Cosmochim. Acta 51, 2401–2416. https://doi.org/10.1016/0016-7037(87)90293-6

D.J. Wronkiewicz, Geochemical and mineralogic investigation of Precambrian metasediments from the Kaapvaal craton, South Africa, Ph.D. Diss., New Mexico Institute of Mining and Technology, Socorro, NM, 1989.

Wronkiewicz, D.J., Condie, K.C., 1990. Geochemistry and mineralogy of sediments from the Ventersdorp and Transvaal Supergroups, South Africa: Cratonic evolution during the early Proterozoic. Geochim. Cosmochim. Acta 54, 343–354. https://doi.org/10.1016/0016-7037(90)90323-D

Young, G.M., 1981. The Amundsen embayment, northwestern territories; relevance to the Upper Proterozoic evolution of North America. In: Campbell, F.H.A. (Ed.), Proterozoic basins of Canada. Geol. Surv. Canada Paper 81-10, pp. 203–218.

Zerkle, A. L., Poulton, S. W., Newton, R. J., Mettam, C., Claire, M. W., Bekker, A., & Junium, C. K. (2017). Onset of the aerobic nitrogen cycle during the Great Oxidation Event. *Nature*, *542*(7642), 465–467. https://doi.org/10.1038/nature20826

Zhang, X., Sigman, D.M., Morel, F.M., Kraepiel, A.M., 2014. Nitrogen isotope fractionation by alternative nitrogenases and past ocean anoxia. Proc. Natl. Acad. Sci. USA 111, 4782–4787.

Tables

Table 1: Map coordinates for Union Island Group samples.

Sample	ID #	Rock Unit	Latitude	Longitude
Union Island Group				
UN-16-1	[1]	Upper Dolostone	62°02'4.3" N	111°43'55.4" W
UN-16-2	[2]	Upper Dolostone	62°02'3.9" N	111°43'56.5" W
UN-16-3	[3]	Black Shale	62°02'3.0" N	111°44'06.7" W
UN-16-4	[4]	Lower Dolostone	62°02'3.1" N	111°44'08.2" W
UN-16-5	[5]	Black Shale	62°02'3.0" N	111°44'08.4" W
UN-16-6 (Section)	[6]	Upper Dolostone	62°01'55.0" N	111°44'21.6" W
UN-16-7	[7]	Black Shale	62°01'27.2" N	111°46'02.2" W
UN-16-8	[8]	Pyrite Nodules	62°01'25.0" N	111°46'06.8" W
UN-16-9	[9]	Regolith	62°01'24.3" N	111°46'07.7" W
UN-16-10	[10]	Regolith	62°00'53.2" N	111°40'14.0" W
UN-16-11	[11]	Lower Dolostone	62°00'51.9" N	111°48'18.1" W
UN-16-12	[12]	Upper Dolostone	62°00'51.8" N	111°48'20.0" W
UN-16-13	[13]	Black Shale	62°00'47.7" N	111°48'44.0" W
UN-16-14	[14]	Lower Dolostone	62°00'23.6" N	111°50'42.3" W
UN-16-15	[15]	Black Shale	62°00'22.0" N	111°50'44.6" W
UN-16-16	[16]	Upper Dolostone	62°00'19.3" N	111°50'39.6" W
UN-16-17	[17]	Upper Dolostone	62°00'19.3" N	111°50'39.6" W
UN-16-18	[18]	Upper Dolostone	61°59'09.4" N	111°55'12.0" W
UN-16-19	[19]	Lower Dolostone	61°59'04.7" N	111°51'41.7" W
UN-16-20	[20]	Lower Dolostone	61°59'40.3" N	111°50'35.7" W
UN-16-21	[21]	Sulfide Veins/Pyrobitumen	62°00'12.9" N	111°47'56.9" W
UN-16-22	[22]	Black Shale	62°00'12.9" N	111°47'56.9" W
UN-16-23	[23]	Upper Dolostone	62°00'37.9" N	111°45'56.0" W
UN-16-24	[24]	Gray Shale	62°00'37.9" N	111°45'56.0" W
UN-16-25	[25]	Black Shale	61°54'33.0" N	111°02'50.9" W
UN-16-26	[26]	Black Shale	61°54'33.0" N	111°02'50.9" W
UN-16-27 (Section)	[27]	Upper Dolostone	61°54'40.5" N	112°02'47.3" W
UN-16-28	[28]	Black Shale	61°56'17.4" N	112°06'23.5" W
UN-16-29	[29]	Black Shale	61°56'14.9" N	112°06'24.6" W
UN-16-30	[30]	Black Shale	62°01'03.6" N	111°33'16.0" W
UN-16-31 (Section)	[31]	Lower Dolostone	62°01'45.3" N	111°31'31.2" W
UN-16-32	[32]	Lower Dolostone	62°01'53.4" N	111°31'17.6" W
UN-16-33	[33]	Upper Dolostone	62°00'51.6" N	111°43'21.1" W
UN-16-34 (Section)	[34]	Lower Dolostone	61°56'29.5" N	112°04'47.6" W
UN-16-35 (Section)	[35]	Lower Dolostone	61°56'16.7" N	112°05'33.7" W
UN-16-36-1/2	[36]	Red and Green Mudstone	61°59'28.6" N	111°46'13.6" W
UN-16-37	[37]	Red and Green Mudstone	61°57'57.8" N	111°50'01.0" W
UN-16-38	[38]	Red and Green Mudstone	61°58'54.3" N	111°48'41.0" W

Table 1 (continued): Map coordinates for Union Island Group samples.

Sample	ID #	Rock Unit	Latitude	Longitude
Union Island Group				
UN-1	[39]	Upper Dolostone	62°01'40.6" N	111°45'00.0" W
UN-1A	[40]	Upper Dolostone	62°01'40.6" N	111°45'00.0" W
UN-2A	[41]	Upper Dolostone	62°01'40.6" N	111°45'00.0" W
UN-2B	[42]	Upper Dolostone	62°01'40.6" N	111°45'00.0" W
UN-3-1	[43]	Lower Dolostone	61°59'49.7" N	111°47'54.4" W
UN-3-1-2	[44]	Lower Dolostone	61°59'49.7" N	111°47'54.4" W
UN-3-2	[45]	Lower Dolostone	61°59'49.7" N	111°47'54.4" W
UN-3-3	[46]	Lower Dolostone	61°59'49.7" N	111°47'54.4" W
UN-3-4	[47]	Lower Dolostone	61°59'49.7" N	111°47'54.4" W
UN-4-1	[48]	Upper Dolostone	61°58'56.5" N	111°48'31.1" W
UN-4-2	[49]	Upper Dolostone	61°58'56.5" N	111°48'31.1" W
UN2-1	[50]	Black Shale	62°00'41.3" N	111°47'19.5" W
UN2-2	[51]	Black Shale	62°00'41.3" N	111°47'19.5" W
UN2-3	[52]	Black Shale	62°00'40.8" N	111°47'19.4" W
UN2-4	[53]	Black Shale	62°00'40.8" N	111°47'19.4" W
UN2-5	[54]	Black Shale	62°00'40.8" N	111°47'19.4" W
UN2-6	[55]	Black Shale	62°00'40.8" N	111°47'20.0" W
UN2-7	[56]	Black Shale	62°00'40.0" N	111°47'21.0" W
UN2-8	[57]	Black Shale	62°00'39.9" N	111°47'22.1" W
UN2-9	[58]	Black Shale	62°00'37.9" N	111°47'26.1" W
UN2-10	[59]	Black Shale	62°00'37.5" N	111°47'27.3" W
UN2-11	[60]	Black Shale	62°00'36.9" N	111°47'29.3" W
UN2-13	[61]	Black Shale	62°00'36.1" N	111°47'30.0" W
UN2-14	[62]	Black Shale	62°00'36.1" N	111°47'30.0" W
UN2-15	[63]	Black Shale	62°00'36.1" N	111°47'30.0" W
UN5-1	[64]	Black Shale	62° 0'23.5"N	111°46'49.3" W
UUGD-1A	[65]	Upper Dolostone	62°00'52.4" N	111°33'46.2" W
UUGD-1B	[66]	Upper Dolostone	62°00'52.4" N	111°33'46.2" W
UUGD-2	[67]	Upper Dolostone	62°00'52.4" N	111°33'46.2" W
UUGD-3A	[68]	Upper Dolostone	62°00'52.4" N	111°33'46.2" W
UUGD-3B	[69]	Upper Dolostone	62°00'52.4" N	111°33'46.2" W
UUGD-4A	[70]	Upper Dolostone	62°00'56.3" N	111°33'48.6" W
UUGD-4B	[71]	Upper Dolostone	62°00'56.3" N	111°33'48.6" W
UUGD-5-1-2	[72]	Upper Dolostone	61°58'00.9" N	111°36'03.8" W
UUGD-5-2-2	[73]	Upper Dolostone	61°58'00.9" N	111°36'03.8" W
CAMP DOLOSTONE	[74]	Upper Dolostone	62° 0'46.1"N	111°46'51.5"W
LH15-EA05	[75]	Upper Dolostone	62°01'023" N	111°33'66.5" W

Table 1 (continued): Map coordinates for Wilson Island Group samples.

Sample	ID #	Rock Unit	Latitude	Longitude
Wilson Island Group				
WI-16-1	[76]	Safety Cove Formation	62°02'32.5" N	111°42'27.5" W
WI-2-1	[77]	Safety Cove Formation	62°02'38.7" N	111°42'03.1" W
WI-2-2	[78]	Safety Cove Formation	62°02'38.7" N	111°42'03.1" W
WI-2-3	[79]	Safety Cove Formation	62°02'38.7" N	111°42'03.1" W
WI-2-4	[80]	Safety Cove Formation	62°02'38.7" N	111°42'03.1" W
WI-2-5	[81]	Safety Cove Formation	62°02'38.7" N	111°42'03.1" W
WI-2-7-1	[82]	Safety Cove Formation	62°02'38.7" N	111°42'03.1" W
WI-2-7-2	[83]	Safety Cove Formation	62°02'38.7" N	111°42'03.1" W
WI-2-8	[84]	Safety Cove Formation	62°04'35.5" N	111°37'39.6" W
WI-3	[85]	Safety Cove Formation	62°02'35.4" N	111°45'41.1" W
WI-4	[86]	Safety Cove Formation	62°02'36.7" N	111°45'38.0" W
WI-5	[87]	Safety Cove Formation	62°02'36.4" N	111°45'38.9" W
WI-L0-01	[88]	Safety Cove Formation	62°02'36.4" N	111°45'38.9" W
WI-05-1/1	[89]	Safety Cove Formation	62°02'36.4" N	111°45'38.9" W
WI-05-1/2	[90]	Safety Cove Formation	62°02'36.4" N	111°45'38.9" W
WI-6-1	[91]	Safety Cove Formation	62°02'31.3" N	111°45'51.1" W
WI-6-2	[92]	Safety Cove Formation	62°02'31.3" N	111°45'51.1" W

Table 2: Compiled data for Union Island Group and Wilson Island Group dolostones.

Sample ID	Mineralogy	$\delta^{13}C_{carb}$ (‰, VPDB)	$\delta^{18}O$ (‰, VPDB)	TOC (wt %)	$\delta^{13}C_{org}$ (‰, VPDB)	$\Delta^{13}C$ (‰, VPDB)	$^{87}Sr/^{86}Sr$ (‰)	Mg mg/g	Ca mg/g	Mn µg/g	Fe µg/g	Sr µg/g	Mg/Ca	Mn/Sr
Union Island Group														
UN-16-1	ferroan dolomite	0.9	-8.4	0.02	-23.9	24.8		113.9	204.8	2145.96	11476.47	47.59	0.556	45
UN-16-1A	ferroan dolomite	0.7	-10.1	0.02	-23.9	24.6								
UN-16-2	ferroan dolomite	1.2	-9.6	0.02	-24.0	25.2		91.05	171.2	1116.86	14685.32	32.13	0.532	35
UN-16-4	ferroan dolomite	6.4	-9.9	0.01				113.79	203.61	1457.85	8156.62	62.49	0.559	23
UN-16-6-0m	ferroan dolomite	0.8	-10.1	0.07	-26.2	27.0								
UN-16-6-4.5m	ferroan dolomite	0.7	-9.1	0.07	-26.2	26.8								
UN-16-6-7m	ferroan dolomite	0.4	-9.4	0.07	-35.0	35.4								
UN-16-6-10m	ferroan dolomite	1.4	-10.0	0.04	-30.8	32.2	0.72448	92.86	165.42	1025.15	8579.31	46.28	0.561	22
UN-16-6-11.5m	ferroan dolomite	0.8	-9.3	0.03	-32.0	32.8								
UN-16-6-12.1m	ferroan dolomite	0.8	-9.8	0.02	-22.1	23.0								
UN-16-6-14.1m	ferroan dolomite	0.9	-10.0	0.02	-29.6	30.4								
UN-16-6-15.6m	ferroan dolomite	0.4	-11.3	0.02	-23.9	24.2								
UN-16-6-18.6m	ferroan dolomite	0.1	-9.5	0.02	-24.4	24.5		105.25	191.79	1627.46	9130.32	46.95	0.549	35
UN-16-6-21.6m	ferroan dolomite	0.1	-9.7	0.03	-35.6	35.7								
UN-16-6-22.6m	ferroan dolomite	1.0	-9.6	0.02	-32.1	33.1								
UN-16-6-25m	dolomite	0.5	-9.4	0.03	-36.5	37.1	0.746003	96.68	182.16	943.01	11454.8	45.11	0.531	21
UN-16-6-26.6m	dolomite	1.4	-13.1	0.04	-33.1	34.5								
UN-16-6-29.1m	ferroan dolomite	0.7	-12.3	0.02	-31.5	32.2								
UN-16-6-35.1m	dolomite	0.0	-12.7	0.05	-29.9	29.9								
UN-16-16-39.1m	dolomite	-0.1	-12.6	0.04	-33.8	33.7								
UN-16-6-40.1m	ferroan dolomite	1.2	-10.2	0.08	-30.1	31.3	0.7353	82.42	162.25	1649.36	25011.59	34.64	0.508	48
UN-16-9	ferroan dolomite	0.5	-8.9	0.01	-23.5	24.0								
UN-16-11	ferroan dolomite	4.6	-11.0	0.10	-26.7	31.3		119.76	207.72	1330.23	13625.5	46.73	0.577	28
UN-16-12	ferroan dolomite	2.8	-7.9	0.01	-28.6	31.4								
UN-16-14	dolomite	2.2	-15.8	0.01	-32.4	34.6	0.73783	109.01	203.89	1833.39	23660.15	150.48	0.535	12
UN-16-17	ferroan dolomite	-0.1	-8.2	0.03	-27.7	27.6								
UN-16-18	ferroan dolomite	-0.3	-15.1	0.03	-25.8	25.6								
UN-16-19	dolomite	-4.4	-9.2	0.02	-25.6	21.1								
UN-16-20	dolomite	8.6	-7.8	0.68	-41.2	49.8	0.7084	121.81	220.58	549.59	3897.75	47.01	0.552	12
UN-16-23	ferroan dolomite	0.6	-10.6	0.01	-24.1	24.7		102.18	199.44	1954.18	22644.45	57.04	0.512	34
UN-16-27-0m	ferroan dolomite	1.3	-8.6	0.01	-24.0	25.4								
UN-16-27-4m	ferroan dolomite	2.3	-8.0	0.03	-28.2	30.5								
UN-16-27-14m	dolomite	1.6	-8.8	0.02	-24.4	25.9		94.64	165.72	494.47	12705.75	25.3	0.571	20
UN-16-27-19m	dolomite	1.2	-8.7	0.01	-35.0	36.2	0.7303	97.10	167.79	411.39	5845.34	24.75	0.579	17
UN-16-27-24m	dolomite	1.5	-5.6	0.01	-24.3	25.8	0.7305	109.22	189.63	328.19	5723.55	19.10	0.576	17
UN-16-27-29m	ferroan dolomite	0.8	-8.3	0.01	-28.2	29.1	0.7095	77.57	146.58	447.23	15689.60	19.99	0.529	22
UN-16-27-34m	ferroan dolomite	1.3	-7.1	0.01	-27.0	28.3	0.7434	98.92	186.69	619.55	20075.31	22.58	0.530	27

Table 2 (continued): Compiled data for Union Island Group and Wilson Island Group dolostones.

Sample ID	Mineralogy	$\delta^{13}C_{carb}$ (‰, VPDB)	$\delta^{18}O$ (‰, VPDB)	TOC (wt %)	$\delta^{13}C_{org}$ (‰, VPDB)	$\Delta^{v}C$ (‰, VPDB)	$^{87}Sr/^{86}Sr$ (‰)	Mg mg/g	Ca mg/g	Mn µg/g	Fe µg/g	Sr µg/g	Mg/Ca	Mn/Sr
Union Island Group														
UN-16-27-38m	ferroan dolomite	1.1	-8.2	0.03	-27.0	28.1		99.35	190.59	547.34	18196.57	22.53	0.521	24
UN-16-27-43m	ferroan dolomite	1.3	-6.5	0.01	-30.3	31.6	0.7642	94.56	174.39	606.31	20725.34	22.28	0.542	27
UN-16-27-48m	ferroan dolomite	1.1	-9.2	0.03	-33.6	34.7	0.7411	88.17	168.70	757.07	19185.36	26.73	0.523	28
UN-16-27-58m	ferroan dolomite	0.6	-7.0	0.01	-28.8	29.3	0.7366	105.48	197.92	787.41	15051.43	24.01	0.533	33
UN-16-27-72m	dolomite	0.6	-7.6	0.01	-30.3	30.9		118.51	210.47	522.99	6272.73	29.89	0.563	17
UN-16-27-76m	dolomite	1.2	-6.1	0.01	-30.2	31.4		119.81	216.82	1111.92	8894.12	35.11	0.553	32
UN-16-27-78m	dolomite	0.6	-9.7	0.01	-29.5	30.2		104.22	192.67	3433.49	13191.56	23.54	0.541	146
UN-16-27-81m	dolomite	0.9	-7.8	0.06	-26.4	27.3	0.7165	115.15	209.86	1771.30	9988.95	27.47	0.549	64
UN-16-27-83m	dolomite	0.9	-8.3	0.01	-29.9	30.8		90.29	165.48	2069.17	12358.32	39.18	0.546	53
UN-16-27-88m	ferroan dolomite	0.7	-8.9	0.01	-28.2	28.9	0.73711	67.57	133.35	768.25	25051.79	39.21	0.507	20
UN-16-27-91m	ferroan dolomite	0.6	-10.0	0.05	-37.5	38.1		68.27	143.50	747.00	27429.04	26.85	0.476	28
UN-16-27-121m	dolomite	1.5	-10.6	0.03	-34.3	35.8		98.37	191.83	2385.96	22029.46	35.11	0.513	68
UN-16-27-126m	ferroan dolomite	0.9	-12.6	0.01	-26.2	27.1		59.64	124.02	1169.47	24456.61	57.64	0.481	20
UN-16-27-128.5m	dolomite	0.3	-12.7	0.02	-30.3	30.6	0.72302	57.10	221.97	1291.91	16270.34	68.34	0.257	19
UN-16-27-134.5m	dolomite	0.5	-12.3	0.02	-32.6	33.1		52.66	125.61	1615.67	18112.50	68.04	0.419	24
UN-16-31-0m	dolomite	6.5	-7.4	0.03	-28.9	35.4								
UN-16-31-5m	dolomite	5.4	-9.7	0.01	-33.9	39.3	0.73344	122.69	214.6	901.05	6099.36	126.62	0.572	7
UN-16-31-8m	dolomite	7.9	-8.2	0.03	-35.9	43.8	0.75554	122.27	216.60	442.46	4398.40	78.55	0.564	6
UN-16-31-11m	dolomite	7.1	-9.8	0.01	-31.7	38.8		118.06	203.35	427.74	4398.45	49.84	0.581	9
UN-16-31-15m	dolomite	7.6	-8.4	0.01	-29.0	36.6	0.71008	120.98	213.53	536.47	4727.36	105.87	0.567	5
UN-16-31-19m	dolomite	8.7	-7.1	0.01	-24.0	32.7	0.71183	124.13	211.53	435.89	3390.61	61.95	0.587	7
UN-16-31-21m	dolomite	7.5	-8.7	0.01	-32.2	39.7		124.40	217.13	590.49	6012.58	56.41	0.573	10
UN-16-32	dolomite	7.6	-6.8	0.01	-37.9	45.5	0.71598	121.42	214.18	848.78	6056.94	43.73	0.567	19
UN-16-33	ferroan dolomite	-8.3	-14.5	0.01	-32.3	24.0								
UN-16-34-0m	dolomite	7.9	-8.6	0.01	-34.1	42.0		116.84	211.51	529.71	5465.62	31.87	0.552	17
UN-16-34-6m	ferroan dolomite	5.1	-9.6	0.01	-32.9	38.0		103.80	203.35	1646.52	21151.34	26.71	0.510	62
UN-16-34-8m	dolomite	6.0	-9.0	0.07	-25.0	31.0								
UN-16-34-10m	dolomite	7.5	-7.7	0.03	-31.8	39.2								
UN-16-34-13m	dolomite	8.6	-7.6	0.05	-34.7	43.2	0.7324	88.7	155.21	725.38	7285.38	22.22	0.571	33
UN-16-34-17m	dolomite	8.3	-7.7	0.01	-36.1	44.4	0.7377	88.95	156.64	741.98	6681.96	24.00	0.568	31
UN-16-34-20m	dolomite	8.0	-8.3	0.03	-42.1	50.0		114.76	205.19	1682.79	9624.54	52.08	0.559	32
UN-16-35-0m	dolomite	8.3	-7.3	0.01	-25.2	33.6	0.709							
UN-16-35-3mA	dolomite	8.1	-8.2	0.02	-22.7	30.9	0.7085	112.99	205.72	696.22	7828.29	55.52	0.549	13
UN-16-35-3mB	dolomite	8.9	-7.5	0.08	-25.1	34.0	0.7095	117.63	208.11	545.46	4368.99	58.94	0.565	9
UN-16-35-6m	dolomite	9.1	-8.0	0.04	-40.6	49.8		108.73	188.53	874.87	6137.48	39.98	0.577	22
UN-16-35-10m	dolomite	5.9	-9.5	0.02	-28.1	34.0		83.11	150.28	1420.88	11567.30	40.90	0.553	35
UN-16-35-14m	dolomite	9.2	-7.5	0.01	-27.7	36.9		122.02	213.34	977.42	3781.51	28.84	0.572	34
UN-16-35-24m	dolomite	8.0	-6.7	0.01	-30.8	38.8		115.11	199.23	841.26	4041.07	42.77	0.578	20
UN-16-35-32m	dolomite	7.9	-7.1	0.01	-27.6	35.5	0.71126	121.36	209.91	826.97	4171.87	74.70	0.578	11
CAMPDOLO	dolomite	-4.0	-18.5	0.01	-31.3	27.2								

Table 2 (continued): Compiled data for Union Island Group and Wilson Island Group dolostones.

Sample ID	Mineralogy	$\delta^{13}C_{carb}$ (‰, VPDB)	$\delta^{18}O$ (‰, VPDB)
Union Island Group			
UN-1A	dolomite	0.1	-14.2
UN-1B	dolomite	0.2	-14.2
UN-2A	dolomite	-0.7	-16.7
UN-2B	dolomite	-0.7	-17.1
UN-3-1	dolomite	9.5	-9.3
UN-3-1-2	dolomite	7.5	-9.5
UN-3-2	dolomite	8.1	-10.0
UN-3-2A	dolomite	6.6	-9.2
UN-3-2-B	dolomite	7.3	-8.8
UN-3-3	dolomite	7.7	-9.2
UN-3-3A	dolomite	7.7	-9.3
UN-3-3B	dolomite	7.7	-9.2
UN-3-4A	dolomite	7.5	-8.9
UN-3-4B	dolomite	7.4	-9.2
UN3-5A	dolomite	7.8	-9.5
UN-4-1	dolomite	1.3	-9.3
UN-4-2/1A	dolomite	0.5	-11.3
UN-4-2/2B	dolomite	0.6	-11.3
UUGD-1A	dolomite	1.0	-7.2
UUGD-1B	dolomite	0.9	-8.3
UUGD-2	dolomite	0.9	-6.5
UUGD-3A	ferroan dolomite	0.2	-14
UUGD-3B	ferroan dolomite	0.8	-10.7
UUGD-4A	ferroan dolomite	0.0	-8.3
UUGD-4B	ferroan dolomite	-1.5	-8.8
UUGD-5-1-2	dolomite	0.1	-10.2
UUGD-5-2-2	dolomite	-1.0	-13.8
Wilson Island Group			
WI-16-1	ferroan dolomite	1.5	-10.3
WI-3	ferroan dolomite	-2.1	-17.7
WI-4	dolomite	-1.8	-17.3
WI-5	ferroan dolomite	-1.3	-17.0
WI-2-1	dolomite	1.3	-10.1
WI-2-2	dolomite	0.5	-10.6
WI-2-3	dolomite	0.8	-12.1
WI-2-4	dolomite	1.7	-10.8
WI-2-5	dolomite	1.6	-10.5
WI-2-7-1	dolomite	1.4	-10.6
WI-2-7-2	dolomite	1.3	-11.5
WI-2-8	dolomite	1.5	-10.1
WI-L0-01	dolomite	1.3	-13.9
WI-05-1/1	dolomite	0.2	-16.9
WI-05-1/2	dolomite	0.3	-16.3
WI-6-1	ferroan dolomite (cement around quartz grains)	-3.3	-14.9
WI-6-2	ferroan dolomite (cement around quartz grains)	-3.2	-17.5

Table 3: Compiled data for the Union Island Group black shales, red and green mudstones, and gray shale samples.

Sample ID	Rock Type	$\delta^{13}C$ (‰, VPDB)	LOA (%)	TIC (wt %)	TOC (wt %)	TN (wt %)	δ15N (‰)	C/N	ε_{Nd}	TDM Age (Ga)
UN2-1	Black Shale	-38.0	70.8	8.5	0.6	0.01	3.5	49.5	-0.5	2.9
UN2-2	Black Shale	-38.5	8.7	1.0	4.2	0.12	4.9	35.0		
UN2-3	Black Shale	-37.1	87.2	10.5	0.5	0.01	4.4	33.3		
UN2-4	Black Shale	-38.7	46.0	5.5	2.1	0.04	5.0	52.8		
UN2-5	Black Shale	-37.7	76.9	9.2	0.4	0.01	4.0	27.7	0	3.1
UN2-6	Black Shale	-37.7	81.8	9.8	0.3	0.01	4.0	21.1		
UN2-7	Black Shale	-38.7	32.4	3.9	2.9	0.06	5.1	48.9		
UN2-8	Black Shale	-39.7	41.9	5.0	4.0	0.06	5.0	66.5		
UN2-9	Black Shale	-40.1	38.4	4.6	5.0	0.06	4.8	82.6		
UN2-10	Black Shale	-39.2	25.3	3.0	4.1	0.11	5.5	37.0		
UN2-11	Black Shale	-38.0	92.5	11.1	0.3	0.01	4.0	40.9		
UN2-13	Black Shale	-38.7	64.7	7.8	1.3	0.03	5.2	44.4		
UN2-14	Black Shale	-38.0	81.3	9.8	0.3	0.01	4.4	36.9		
UN2-15	Black Shale	-39.4	34.9	4.2	3.2	0.08	5.3	38.1		
UN5-1	Black Shale	-39.1	14.0	1.7	6.3	0.13	5.1	48.5	-5.1	2.8
UN-16-3	Black Shale	-37.6	31.2	3.7	2.4	0.07	6.3	35.3		
UN-16-5	Black Shale	-40.9	29.0	3.5	2.5	0.08	6.1	31.8		
UN-16-7	Black Shale	-37.8	64.6	7.8	0.8	0.02	6.2	38.3		
UN-16-13	Black Shale	-38.3	70.0	8.4	1.5	0.02	4.5	61.9		
UN-16-15	Black Shale	-40.4	61.8	7.4	1.3	0.03	6.9	42.7		
UN-16-22	Black Shale	-40.0	40.0	4.8	3.2	0.07	5.4	45.7		
UN-16-24	Gray Shale	-31.8	27.5	3.3	0.1	0.01	4.0	9.8		
UN-16-25	Black Shale	-40.8	22.2	2.7	3.4	0.08	6.0	42.0	-7.6	3.1
UN-16-26	Black Shale	-43.1	87.3	10.5	0.7	0.02	5.4	34.3		
UN-16-28	Black Shale	-41.7	50.5	6.1	2.9	0.03	6.4	95.4		
UN-16-29	Black Shale	-33.2	28.5	3.4	0.3	0.01	4.0	28.9		
UN-16-30	Black Shale	-41.6	17.8	2.1	0.6	0.06	2.9	9.9		
UN-16-36-2	Red and Green Mudstone	-26.6	17.5	2.1	0.04	0.02	1.7	2.1		
UN-16-37	Red and Green Mudstone	-27.8	17.0	2.0	0.04	0.02	1.7	1.8	-1.2	2.5
UN-16-38	Red and Green Mudstone	-26.9	22.9	2.7	0.04	0.01	1.6	3.6	3.2	2.2

Table 4: Provenance proxies for the Union Island Group black shale, red and green mudstone, and gray shale.

Sample ID	Rock Type	La/Sc	Th/Sc	La/Cr	Th/Cr	Zr/Sc
UN-16-3	black shale	2.44	0.82	0.39	0.09	10.7
UN-16-5	black shale	1.41	0.43	0.33	0.07	6.7
UN-16-7	black shale	1.73	0.53	0.95	0.10	7.0
UN-16-13	black shale	2.80	0.40	1.82	0.08	7.2
UN-16-15	black shale	1.54	0.31	0.76	0.06	7.6
UN-16-22	black shale	2.35	0.70	0.51	0.09	10.4
UN-16-25	black shale	2.55	0.72	0.34	0.08	11.3
UN-16-26	black shale	0.85	0.13	3.90	0.07	2.0
UN-16-28	black shale	1.97	0.47	0.75	0.09	7.7
UN-16-29	black shale	3.11	1.27	0.73	0.21	8.6
UN-16-30	black shale	1.83	0.50	0.28	0.06	9.3
UN-2-2	black shale	2.85	0.56	0.36	0.06	9.2
UN-2-4	black shale	2.90	0.72	0.49	0.07	12.8
UN-2-7	black shale	2.14	0.73	0.29	0.07	10.2
UN-2-8	black shale	2.23	0.62	0.42	0.07	8.6
UN-2-9	black shale	2.72	0.84	0.40	0.08	11.0
UN-2-10	black shale	1.87	0.58	0.26	0.06	8.1
UN-2-13	black shale	1.73	0.33			5.6
UN-2-15	black shale	5.71	0.93	0.93	0.10	33.1
UN-5-1	black shale	2.68	0.74	0.30	0.07	9.3
UN-16-24	gray shale	6.21	0.56	1.25	0.08	8.1
UN-16-37	red and green mudstone	2.55	0.95	0.48	0.15	10.2
UN-16-38	red and green mudstone	3.00	1.00	0.61	0.16	9.9
UN-16-36-2	red and green mudstone	2.63	0.88	0.52	0.14	9.2

Table 5: Rare-earth element concentrations for Union Island Group black shales, red and green mudstones, and gray shale samples. All values are normalized to Post-Archean Average Shale (PAAS) from Taylor and McLennan, (1985).

Sample ID	Rock Type	La (ppm)	Ce (ppm)	Pr (ppm)	Nd (ppm)	Sm (ppm)	Eu (ppm)	Gd (ppm)	Tb (ppm)	Dy(ppm)	Y (ppm)	Ho (ppm)	Er (ppm)	Tm (ppm)	Yb (ppm)	Lu (ppm)
UN-2-2	Black Shale	0.82	0.66	0.82	0.79	0.75	0.55	0.63	0.45	0.41	0.44	0.42	0.45	0.47	0.46	0.51
UN-2-4	Black Shale	0.38	0.30	0.39	0.38	0.38	0.46	0.43	0.40	0.41	0.50	0.44	0.44	0.44	0.41	0.39
UN-2-7	Black Shale	0.39	0.31	0.42	0.41	0.46	0.52	0.56	0.53	0.51	0.57	0.51	0.52	0.54	0.51	0.51
UN-2-8	Black Shale	0.35	0.28	0.36	0.35	0.39	0.47	0.45	0.43	0.40	0.46	0.42	0.41	0.42	0.39	0.39
UN-2-9	Black Shale	0.36	0.28	0.36	0.35	0.38	0.42	0.42	0.39	0.40	0.44	0.41	0.40	0.49	0.41	0.44
UN-2-10	Black Shale	0.49	0.38	0.52	0.50	0.58	0.56	0.64	0.58	0.57	0.59	0.55	0.54	0.52	0.54	0.51
UN-2-13	Black Shale	0.14	0.11	0.15	0.16	0.22	0.34	0.31	0.30	0.31	0.36	0.31	0.29	0.27	0.27	0.25
UN-2-15	Black Shale	1.20	0.99	1.24	1.20	1.26	1.18	1.32	1.15	1.18	1.51	1.24	1.26	1.31	1.14	1.11
UN-5-1	Black Shale	0.56	0.41	0.56	0.52	0.54	0.52	0.52	0.44	0.42	0.48	0.43	0.46	0.44	0.43	0.44
UN-16-3	Black Shale	0.58	0.48	0.58	0.55	0.57	0.53	0.64	0.58	0.54	0.61	0.54	0.58	0.62	0.55	0.58
UN-16-5	Black Shale	0.59	0.51	0.61	0.62	0.68	0.72	0.77	0.74	0.71	0.77	0.73	0.74	0.79	0.76	0.76
UN-16-7	Black Shale	0.18	0.16	0.19	0.19	0.23	0.34	0.30	0.27	0.26	0.28	0.26	0.24	0.25	0.21	0.21
UN-16-13	Black Shale	0.29	0.23	0.31	0.32	0.37	0.55	0.51	0.47	0.49	0.63	0.51	0.53	0.49	0.51	0.53
UN-16-15	Black Shale	0.36	0.32	0.41	0.45	0.52	0.78	0.69	0.59	0.56	0.62	0.57	0.54	0.52	0.46	0.48
UN-16-16	Black Shale	0.13	0.12	0.18	0.20	0.26	0.40	0.31	0.28	0.27	0.33	0.24	0.26	0.22	0.21	0.21
UN-16-22	Black Shale	0.49	0.40	0.50	0.50	0.56	0.70	0.70	0.62	0.61	0.67	0.59	0.61	0.64	0.57	0.60
UN-16-24	Gray Shale	2.76	2.27	2.41	2.19	2.00	2.04	1.52	1.11	0.94	0.78	0.82	0.73	0.79	0.72	0.72
UN-16-25	Black Shale	0.67	0.51	0.66	0.63	0.67	0.74	0.78	0.68	0.62	0.70	0.64	0.64	0.74	0.59	0.65
UN-16-26	Black Shale	0.18	0.14	0.18	0.21	0.33	0.49	0.50	0.49	0.49	0.55	0.50	0.49	0.49	0.45	0.46
UN-16-28	Black Shale	0.46	0.39	0.50	0.50	0.58	0.69	0.73	0.67	0.68	0.77	0.70	0.71	0.69	0.63	0.65
UN-16-29	Black Shale	1.22	1.09	1.17	1.07	1.07	0.92	1.03	0.90	0.82	0.78	0.78	0.79	0.81	0.77	0.79
UN-16-30	Black Shale	0.86	0.80	0.90	0.85	0.88	1.06	0.92	0.80	0.71	0.69	0.67	0.62	0.64	0.59	0.60
UN-16-36-2	Red and Green Mudstone	1.24	1.10	1.16	1.11	1.15	1.07	1.13	1.03	0.99	0.97	0.97	0.98	1.04	0.96	0.97
UN-16-37	Red and Green Mudstone	1.14	1.08	1.17	1.09	1.10	1.05	1.13	0.98	0.95	0.89	0.93	0.97	1.04	0.96	0.97
UN-16-38	Red and Green Mudstone	1.10	1.12	1.11	1.06	1.12	1.06	1.14	1.01	0.94	0.91	0.94	0.93	0.99	0.88	0.90

Table 6: REE anomalies for Union Island Group black shales, red and green mudstones, and gray shale samples. Calculation of Eu/Eu^*_{SN}, Ce/Ce^*_{SN}, and Pr/Pr^*_{SN} are referenced from Bau and Dulski, (1996). Calculating Y/Y* is referenced from Li et al., (2018).

Sample ID	Rock Type	Eu/Eu^*_{SN}	Ce/Ce^*_{SN}	Pr/Pr^*_{SN}	Y/Y^*_{SN}	Y/Ho	Pr/Yb_{SN}	Sm/Yb_{SN}
UN-2-2	Black Shale	0.84	0.80	1.13	1.04	28.3	1.76	1.62
UN-2-4	Black Shale	1.20	0.78	1.14	1.16	30.9	0.93	0.92
UN-2-7	Black Shale	1.08	0.77	1.16	1.11	30.6	0.81	0.88
UN-2-8	Black Shale	1.18	0.78	1.16	1.13	30.0	0.92	0.98
UN-2-9	Black Shale	1.09	0.79	1.14	1.09	29.5	0.87	0.92
UN-2-10	Black Shale	0.97	0.76	1.17	1.06	29.5	0.96	1.07
UN-2-13	Black Shale	1.38	0.79	1.09	1.17	31.9	0.55	0.81
UN-2-15	Black Shale	0.96	0.82	1.13	1.25	33.5	1.08	1.10
UN-5-1	Black Shale	1.02	0.73	1.20	1.12	30.5	1.28	1.25
UN-16-3	Black Shale	0.92	0.82	1.13	1.13	30.9	1.05	1.03
UN-16-5	Black Shale	1.03	0.84	1.08	1.07	29.2	0.80	0.89
UN-16-7	Black Shale	1.40	0.84	1.10	1.06	29.2	0.92	1.09
UN-16-13	Black Shale	1.35	0.78	1.12	1.25	33.5	0.60	0.73
UN-16-15	Black Shale	1.43	0.82	1.07	1.11	30.4	0.89	1.13
UN-16-22	Black Shale	1.21	0.80	1.12	1.13	31.7	0.87	0.97
UN-16-24	Gray Shale	1.19	0.88	1.08	0.88	26.2	3.33	2.76
UN-16-25	Black Shale	1.10	0.76	1.17	1.11	30.2	1.11	1.12
UN-16-26	Black Shale	1.27	0.77	1.02	1.11	30.2	0.39	0.73
UN-16-28	Black Shale	1.12	0.81	1.12	1.13	30.6	0.78	0.91
UN-16-29	Black Shale	0.90	0.91	1.09	0.97	27.5	1.52	1.38
UN-16-30	Black Shale	1.25	0.90	1.10	1.00	28.5	1.53	1.49
UN-16-36-2	Red and Green Mudstone	0.99	0.92	1.05	1.00	27.7	1.20	1.19
UN-16-37	Red and Green Mudstone	0.99	0.94	1.07	0.95	26.3	1.21	1.13
UN-16-38	Red and Green Mudstone	0.97	1.01	1.02	0.97	26.7	1.25	1.26

Table 7: Trace metal data for Union Island black shales, red and green mudstones, and gray shale samples

Sample ID	Rock Type	TOC (wt %)	Mo (ppm)	U (ppm)	Th (ppm)	U/Th	U/TOC	Mo/TOC
UN-2-2	Black Shale	4.2	9.9	7.1	6.8	1.0	1.7	2.3
UN-2-4	Black Shale	2.1	6.3	8.2	6.7	1.2	3.9	3.0
UN-2-7	Black Shale	2.9	6.4	5.5	7.5	0.7	1.9	2.2
UN-2-8	Black Shale	4.0	19.5	7.1	6.4	1.1	1.8	4.9
UN-2-9	Black Shale	5.0	13.2	8.3	6.8	1.2	1.7	2.7
UN-2-10	Black Shale	4.1	6.2	5.6	7.8	0.7	1.4	1.5
UN-2-13	Black Shale	1.3	1.1	3.1	2.8	1.1	2.5	0.9
UN-2-15	Black Shale	3.2	7.2	14.1	11.4	1.2	4.4	2.2
UN-5-1	Black Shale	6.3	11.4	7.3	6.9	1.1	1.2	1.8
UN-16-3	Black Shale	2.4	6.0	5.2	10.8	0.5	2.2	2.5
UN-16-5	Black Shale	2.5	8.0	6.6	9.6	0.7	2.7	3.2
UN-16-7	Black Shale	0.8	0.8	2.0	5.9	0.3	2.4	1.0
UN-16-13	Black Shale	1.5	3.0	7.7	5.3	1.4	5.2	2.0
UN-16-15	Black Shale	1.3	6.8	4.7	7.3	0.6	3.7	5.3
UN-16-22	Black Shale	3.2	11.7	6.8	9.3	0.7	2.1	3.7
UN-16-24	Gray Shale	0.1	0.14	2.5	13.2	0.19	25.2	1.4
UN-16-25	Black Shale	3.4	5.1	4.8	9.3	0.5	1.4	1.5
UN-16-26	Black Shale	0.7	7.9	12.6	7.9	1.6	18.3	11.5
UN-16-28	Black Shale	2.9	9.7	7.7	8.5	0.9	2.7	3.4
UN-16-29	Black Shale	0.3	0.14	5.3	26.6	0.2	18.4	0.5
UN-16-30	Black Shale	0.6	0.6	2.7	11.0	0.2	4.7	1.1
UN-16-36-2	Red and Green Mudstone	0.04	-	4.4	19.1	0.23	122.0	-
UN-16-37	Red and Green Mudstone	0.04	-	4.5	19.4	0.23	105.2	-
UN-16-38	Red and Green Mudstone	0.04	0.39	4.2	18.2	0.23	115.9	10.9